2019

# An Improved 3D Complex-Envelope Four-Stage ADI-FDTD Using The Fundamental Scheme

Qi Liu
*University of Mississippi*

# An Improved 3D Complex-Envelope Four-Stage ADI-FDTD Using The Fundamental Scheme

A Dissertation
presented in partial fulfillment of requirements
for the degree of Doctor of Philosophy
in the Department of Electrical Engineering
The University of Mississippi

by

Qi Liu

May 2019

ABSTRACT

The exponential operator splitting approach can be used to transform the two sub-steps based complex-envelope (CE) alternating-direction-implicit (ADI) FDTD algorithm into a four sub-steps based CE four-stages (4S) ADI-FDTD. In two dimensions the CE-4S-ADI-FDTD is more accurate than the CE-ADI-FDTD, but requires double the computation time due to the fixed time consumption in each sub-step.

Here, the existing 2D CE-4S-ADI-FDTD scheme is extended to three spatial dimensions. By incorporating the fundamental scheme into the 3D CE-4S-ADI-FDTD, the proposed 3D-4S-FADI-FDTD method is the result. In the fundamental scheme six auxiliary variables are defined, by which the number of terms and operations in the implicit equations is reduced. The computation time in each sub-step is reduced, and consequently the total computational time. The near perfectly matched layers (NPML) and the total field/scattered field schemes are incorporated into the 3D CE-4S-FADI-FDTD for modeling the problem with a boundless domain, and with a plane wave source respectively.

Three corresponding reference methods are developed. The CE explicit FDTD method is used to solve the problem with a point source and perfect electric conductor (PEC) boundaries. The problem with a point source and absorbing boundary conditions (ABC) is solved by the 3D free-space Green's function in the frequency domain, and then transformed to the time domain using the inverse fast Fourier transform (IFFT). For the problem with a plane wave and ABC, the frequency-domain solution is obtained using the volume integral equations and method of moments (VIE-MOM), and is then transformed into the time-domain solution using the IFFT. Comparison of the numerical results demonstrates the accuracy and computational effectiveness of the 3D CE-4S-FADI-FDTD algorithm.

ACKNOWLEDGEMENTS

I gladly express my sincere gratitude to my advisor, Dr. Paul M. Goggans – a respectable, resourceful and responsible scholar. By following his research notes I entered the world of computational electromagnetics. His idea of incorporating the CE representation into the FDTD formulation was the origin of this dissertation. By benefitting from his experience and suggestions, I found superior ways of modeling and solving problems with differing types of sources and boundary conditions. Dr. Goggans' patient guidance and long-term support continually encouraged me to keep working during my years in the University of Mississippi, and this is deeply appreciated.

I thank also the faculty of the Department of Electrical Engineering, who helped me by providing academic and financial support. In addition, I greatly appreciate the instructors of the classes I attended, from whom I learned a tremendous amount of knowledge which has benefited me very much.

TABLE OF CONTENTS

LIST OF FIGURES

LIST OF TABLES

# CHAPTER 1

# INTRODUCTION

The finite-difference time-domain (FDTD) method of Yee (1966) has been used widely in computational electromagnetics because it is simple to implement and capable of treating complex models over a wide range of frequency. The method is based on Maxwell's time-domain equations integrated with appropriate boundary conditions, well defined material media and specified source excitations. By discretizing the electric and magnetic fields in space and time, Maxwell's differential equations become difference equations, which can be solved by applying the leap-frog technique. The computation period is divided into a number of time steps; at each time step, the field components at the next time instant can be obtained from the field components at the current time instant. Accuracy and stability of this conventional explicit method of this sort depends on the time step being sufficiently short.

According to the Courant-Friedrichs-Lewy (CFL) condition, the maximum size of the time step depends on the spatial step. In the time-marching procedure the time step must be small enough for the amplification factor not to exceed one, so that the magnitude of the field components do not grow exponentially. This is a necessary condition for stability of the algorithm.

The choice of a small time step to achieve stability implies high computational time and cost, because more steps are needed to simulate a given time interval. A number of implicit FDTD algorithms have been developed to mitigate the problem. With a time step of arbitrary size these implicit methods condense the amplification factor and force it to be equal to or less than one. As a result, the necessary condition for stability is satisfied for any

size of time step. In the implicit methods, matrix solutions are needed at each time step, and these cost more time than the updating involved in the explicit method with the same size of time step. A small number of time steps is therefore required for the implicit methods to be more computationally effective. In other words, the time step needs to be several times larger than the Courant condition. Unfortunately, a large time step leads to large errors, especially in problems with a bandpass-limited (BPL) source, because of inadequate sampling. With a larger time step, the implicit methods run faster but less accurately. Consequently the implicit method has greater computational effectiveness than the explicit methods but at the cost of accuracy.

The complex-envelope (CE) FDTD algorithm was proposed by Pursel and Goggans (1999) and, for a BPL problem, greatly increased the maximum possible size of the time step $\Delta t$. According to the sampling theorem, the sampling frequency $f_s$ must be at least $2f_{max}$, where $f_{max}$ is the maximum frequency of the signal and is a function of the center-frequency $f_0$ and the bandwidth $B$. In the time domain, the time step $\Delta t$ is dependent on $f_{max}$, so that $\Delta t$ is reduced as $f_{max}$ increases. For the problem with a narrowband source, the time step must therefore be small for accuracy. Upon applying the CE, however, $f_0$ is shifted to zero, which results in a significant decrease in $f_{max}$. Specifically, $f_{max}$ is proportional to $B$, which is small for a narrow-band signal. As a result the allowable size of $\Delta t$ is greatly increased without much loss of accuracy. Incorporation of the implicit method into the CE algorithm gives the so-called CE implicit method, in which a large time step can be used. Not all implicit methods are compatible with the CE, however. The CE alternating-direction-implicit FDTD (CE-ADI-FDTD) Ma and Chen (2005) is a popular CE implicit method.

Absorbing boundary conditions (ABC) are also required for any FDTD method. Specifically, absorbing walls are considered in order to truncate the computational domain, such that outwardly traveling waves are absorbed after impinging on the boundaries. Consequently the computational domain is considered boundless. There are two categories of

ABC: analytical ABC and the perfectly matched layers (PML). With analytical ABC, the boundary points are manipulated based on the wave equation. The field at the boundary points at previous time instants are needed to cancel out the incident wave at the current time instant, by which means the boundaries are considered reflectionless. With PML, in contrast, several layers of absorbing materials are defined at the boundaries in which fictitious conductivities are introduced. As incident waves travel into the PML region, the magnitude of the waves decays such that waves reflected into the computational domain are almost zero in amplitude.

The research presented in this dissertation aims to formulate a new three-dimensional (3-D) CE implicit method with appropriate absorbing boundary conditions. In this developed method, the four-stages (4S) technique Ramadan (2009) is used to decompose the computational procedure of the 3D CE-ADI-FDTD in Ma and Chen (2005) into four substeps at each time step. Although the computational time needed at each time step is increased, the computational accuracy is significantly increased. By choosing a large time step, the total computation time is greatly reduced at the expense of some accuracy; but the accuracy still remains high because of the improvement from the 4S technique. After incorporating the fundamental scheme of Tan (2008) into the 3D CE-ADI-FDTD, the number of multiplications/divisions (M/D) and additions/subtractions (A/S) in the implicit equations is greatly reduced, and the computation time required for each time step decreases accordingly. The result is that, with a large time step, the proposed 3D CE four-stage ADI-FDTD using the fundamental scheme CE-4S-FADI-FDTD outperforms the 3D CE-ADI-FDTD in accuracy and computational cost. In addition, the 3D CE-4S-FADI-FDTD is incorporated into the nearly perfectly matched layers formalism of Cummer (2003). The numerical results demonstrate that no observable reflected waves exist in the computational domain with a Courant number beyond the stability restriction.

The dissertation is organized as follows. In Chapter 2 the classical FDTD algorithm is discussed using a 3D cavity example with a point source. Three popular unconditionally

stable implicit methods are reviewed. The ADI-FDTD solution and the FDTD solution are compared. In Chapter 3, the CE versions of the three implicit methods are presented, two of which are my own unsuccessful attempts. The 3D CE-ADI-FDTD formulation is then presented. Chapter 4 considers two types of analytical ABC and three types of PML. Chapter 5 sets out the total field/scattered field (TF/SF) scheme for modeling the plane-wave excitation source using the FDTD algorithm. In Chapter 6, the proposed CE-4S-FADI-FDTD method is formulated based on different types of boundary condition and excitation sources. Chapter 7 introduces three reference methods which correspond to the examples in chapter 6. Chapter 8 compares the numerical results based on the proposed methods and reference methods. Conclusions are set out and proposed further development is summarized in Chapter 9.

# CHAPTER 2

# FDTD

Maxwell's equations are a set of partial differential equations that describe the propagation of electromagnetic waves. The time-domain Maxwell's equations with electric and magnetic current sources are:

$$\nabla \times \vec{H} = \epsilon \frac{\partial \vec{E}}{\partial t} + \vec{J}, \tag{2.1}$$

$$\nabla \times \vec{E} = -\mu \frac{\partial \vec{H}}{\partial t} - \vec{M}, \tag{2.2}$$

where $\vec{E}$ is the electric field intensity vector in volts per meter, $\vec{H}$ is the magnetic field intensity vector in amperes per meter, $\epsilon$ is the permittivity of the medium, $\mu$ is the permeability of the medium, $\vec{J}$ is the electric current intensity in amperes per square meter, and $\vec{M}$ is the magnetic current in volts per square meter. The two equations can be decomposed into six component equations in Cartesian coordinates, as follows:

$$\frac{\partial}{\partial t} H_x = -\frac{1}{\mu}\frac{\partial}{\partial y} E_z + \frac{1}{\mu}\frac{\partial}{\partial z} E_y - \frac{1}{\mu} M_x \tag{2.3}$$

$$\frac{\partial}{\partial t} H_y = \frac{1}{\mu}\frac{\partial}{\partial x} E_z - \frac{1}{\mu}\frac{\partial}{\partial z} E_x - \frac{1}{\mu} M_y \tag{2.4}$$

$$\frac{\partial}{\partial t} H_z = -\frac{1}{\mu}\frac{\partial}{\partial x} E_y + \frac{1}{\mu}\frac{\partial}{\partial y} E_x - \frac{1}{\mu} M_z \tag{2.5}$$

$$\frac{\partial}{\partial t} E_x = \frac{1}{\epsilon}\frac{\partial}{\partial y} H_z - \frac{1}{\epsilon}\frac{\partial}{\partial z} H_y - \frac{1}{\epsilon} J_x \tag{2.6}$$

$$\frac{\partial}{\partial t}E_y = -\frac{1}{\epsilon}\frac{\partial}{\partial x}H_z + \frac{1}{\epsilon}\frac{\partial}{\partial z}H_x - \frac{1}{\epsilon}J_y \tag{2.7}$$

$$\frac{\partial}{\partial t}E_z = \frac{1}{\epsilon}\frac{\partial}{\partial x}H_y - \frac{1}{\epsilon}\frac{\partial}{\partial y}H_x - \frac{1}{\epsilon}J_z \tag{2.8}$$

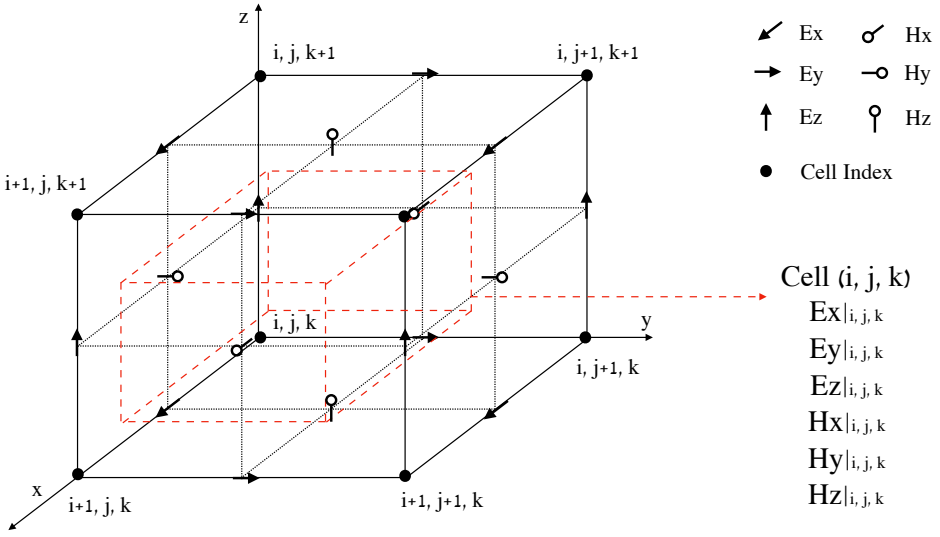


Figure 2.1. Yee Grid

## 2.1 Explicit FDTD

In the classical FDTD algorithm due to Yee (1966), the 3D space is modeled by discrete cells, and the fields in each cell are labeled by spatial indices. The magnetic fields and electric fields are discretized in the time domain by labeling at different time instants. By employing the second-order central difference approximation, the time-domain Maxwell's

equations are discretized as

$$\frac{H_x|_{i,j,k}^{n+\frac{1}{2}} - H_x|_{i,j,k}^{n-\frac{1}{2}}}{\Delta t} = -\frac{1}{\mu\Delta y}(E_z|_{i,j+1,k}^{n} - E_z|_{i,j,k}^{n}) + \frac{1}{\mu\Delta z}(E_y|_{i,j,k+1}^{n} - E_y|_{i,j,k}^{n}) - \frac{1}{\mu}M_x|_{i,j,k}^{n}, \quad (2.9)$$

$$\frac{H_y|_{i,j,k}^{n+\frac{1}{2}} - H_y|_{i,j,k}^{n-\frac{1}{2}}}{\Delta t} = \frac{1}{\mu\Delta x}(E_z|_{i+1,j,k}^{n} - E_z|_{i,j,k}^{n}) - \frac{1}{\mu\Delta z}(E_x|_{i,j,k+1}^{n} - E_x|_{i,j,k}^{n}) - \frac{1}{\mu}M_y|_{i,j,k}^{n}, \quad (2.10)$$

$$\frac{H_z|_{i,j,k}^{n+\frac{1}{2}} - H_z|_{i,j,k}^{n-\frac{1}{2}}}{\Delta t} = -\frac{1}{\mu\Delta x}(E_y|_{i+1,j,k}^{n} - E_y|_{i,j,k}^{n}) + \frac{1}{\mu\Delta y}(E_x|_{i,j+1,k}^{n} - E_x|_{i,j,k}^{n}) - \frac{1}{\mu}M_z|_{i,j,k}^{n}, \quad (2.11)$$

$$\frac{E_x|_{i,j,k}^{n+1} - E_x|_{i,j,k}^{n}}{\Delta t} = \frac{1}{\epsilon\Delta y}(H_z|_{i,j,k}^{n+\frac{1}{2}} - H_z|_{i,j-1,k}^{n+\frac{1}{2}}) - \frac{1}{\epsilon\Delta z}(H_y|_{i,j,k}^{n+\frac{1}{2}} - H_y|_{i,j,k-1}^{n+\frac{1}{2}}) - \frac{1}{\epsilon}J_x|_{i,j,k}^{n+\frac{1}{2}}, \quad (2.12)$$

$$\frac{E_y|_{i,j,k}^{n+1} - E_y|_{i,j,k}^{n}}{\Delta t} = -\frac{1}{\epsilon\Delta x}(H_z|_{i,j,k}^{n+\frac{1}{2}} - H_z|_{i-1,j,k}^{n+\frac{1}{2}}) + \frac{1}{\epsilon\Delta z}(H_x|_{i,j,k}^{n+\frac{1}{2}} - H_x|_{i,j,k-1}^{n+\frac{1}{2}}) - \frac{1}{\epsilon}J_y|_{i,j,k}^{n+\frac{1}{2}}, \quad (2.13)$$

$$\frac{E_z|_{i,j,k}^{n+1} - E_z|_{i,j,k}^{n}}{\Delta t} = \frac{1}{\epsilon\Delta x}(H_y|_{i,j,k}^{n+\frac{1}{2}} - H_y|_{i-1,j,k}^{n+\frac{1}{2}}) - \frac{1}{\epsilon\Delta y}(H_x|_{i,j,k}^{n+\frac{1}{2}} - H_x|_{i,j-1,k}^{n+\frac{1}{2}}) - \frac{1}{\epsilon}J_z|_{i,j,k}^{n+\frac{1}{2}}, \quad (2.14)$$

where the superscript $n$ represents the time instant and the subscripts $(i, j, k)$ represent the spatial position. In these equations, the unknown field in each cell at the next time instant can be represented by the known fields at the current and previous time instant. All fields can therefore be updated explicitly. For example, in (2.9), the fields are centered at time

instant $n$, and $H_x|_{i,j,k}^{n+\frac{1}{2}}$ at the future time instant $(n+\frac{1}{2})$ is the only unknown, and can therefore be calculated explicitly. Similarly, (2.11) is solved explicitly. Next, $E_y|_{i,j,k}^{n+1}$ can be determined by substituting $H_x|_{i,j,k}^{n+\frac{1}{2}}$ and $H_z|_{i,j,k}^{n+\frac{1}{2}}$ into (2.13). At each time step, all other fields can be calculated by the same procedure: the magnetic fields are calculated first, by which the electric fields are updated thereafter. A 3D cavity example is given in Figure 2.2. The cavity size is $45 \times 45 \times 45$ cells, and the z-directed point source $J_z$ is located at (23,23,23), which is the center of the cube. The observation point $(13, 23, 23)$ is 10 cells distant from the source on the negative $x$ axis. The source plane is at $z = 23$.

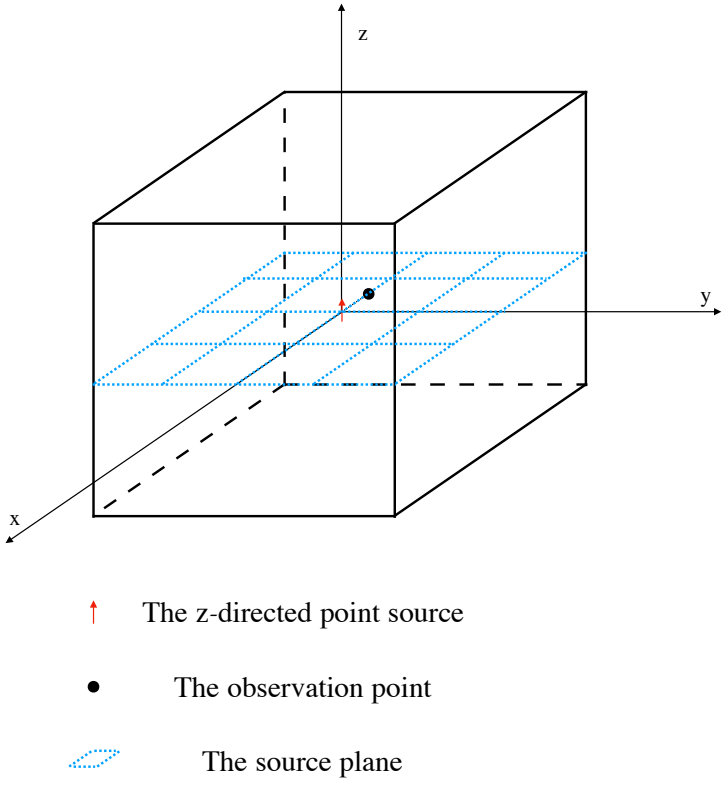


Figure 2.2. 3D cavity example truncated with PEC walls.

The source function is

$$J_z(t) = \exp\left[-\left(\frac{t-t_0}{\sigma}\right)^2\right] \times \left(\frac{t-t_0}{\sigma}\right), \tag{2.15}$$

where the time step $\Delta t = 4.8113 \times 10^{-10}$ second, the spatial step $\Delta x = \Delta y = \Delta z = 0.2498$ meter, $t_0 = 2.7009 \times 10^{-7}$ second and $\sigma = 3.1831 \times 10^{-8}$ second. The distribution of $E_z$ with CFLN= 1 on the source plane at four different time instants is shown in Figure 2.3. In $(a)$, the source is just starting to excite, and the fields in cells far from the source are therefore almost zero. In $(b)$, the field in the source cell is dominant due to the exponential term in the source function. In $(c)$, the field in the source cell decays, since the simulation time exceeds the delay of the Gaussian peak. The fields in other cells become visible. In $(d)$, the simulation time is double the Gaussian delay, so that the impact of the source is negligible and the distribution of $E_z$ on the source plane can be observed.

In FDTD, the distribution of fields in the entire domain is computed at each time instant, and the overall computation time is therefore reduced as the number of time steps decreases. The upper limit of the time step size is also bounded for stability according to the CFL condition. This stability requirement is

$$\text{CFLN} = c_0 \Delta t \sqrt{\frac{1}{\Delta x^2} + \frac{1}{\Delta y^2} + \frac{1}{\Delta z^2}} \leq 1, \tag{2.16}$$

where $c_0$ is the speed of light. If CFLN $> 1$, the amplification factor of the algorithm exceeds 1 in magnitude, causing exponential growth of the solution. The algorithm then becomes unstable immediately after activating the source. In Figure 2.4, $E_z$ at the observation point is shown based on different values of CFLN. For CFLN= 1, the result is stable, but for CFLN= 3 we see that $E_z$ grows exponentially and the FDTD algorithm fails due to instability. Therefore, after setting up the spatial grid, the size of the time step must be bounded for stability; there is a least number of time steps for the FDTD solution. The computation time needed at each time step is also fixed, and there is therefore a minimum value of the overall computation time for the classical FDTD solution.

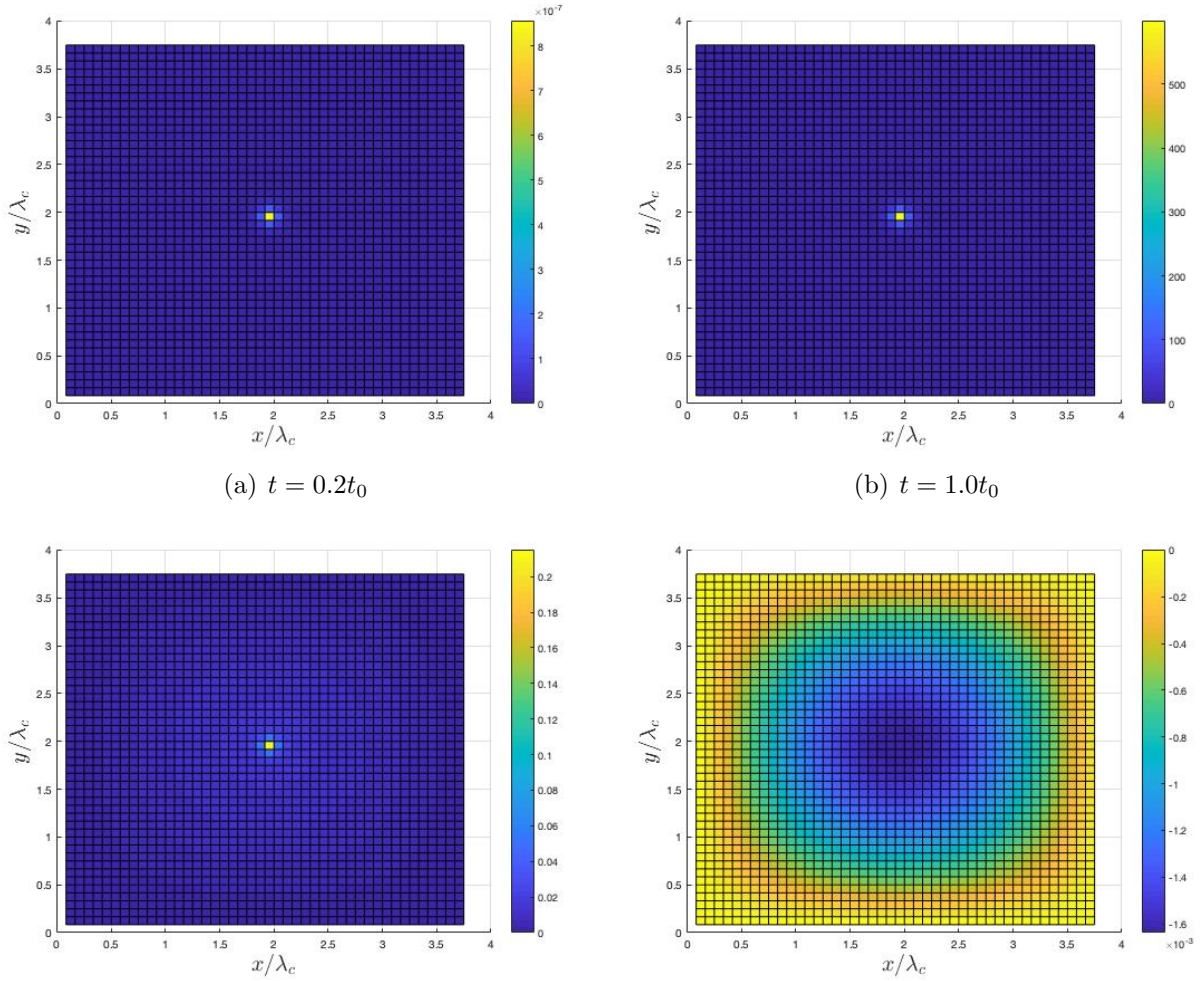


(a) $t = 0.2t_0$

(b) $t = 1.0t_0$

(c) $t = 1.2t_0$

(d) $t = 2.0t_0$

Figure 2.3. The distribution of $E_z$ on the source plane for the 3D cavity example.

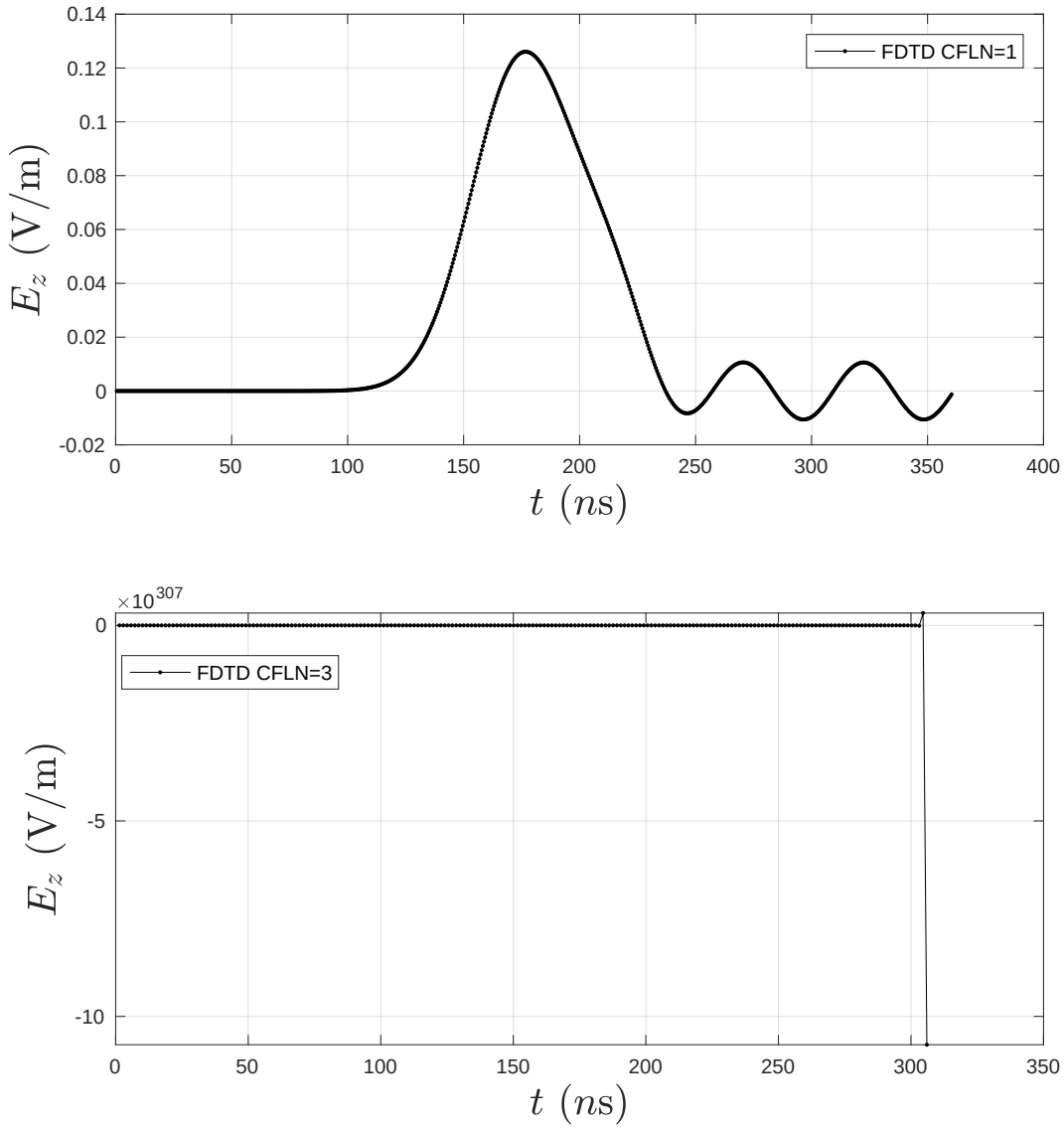


Figure 2.4. The electric field $E_z$ at the observation point based on the FDTD solution.

## 2.2 Implicit FDTD

In the classical FDTD algorithm the electric fields and magnetic fields are known at differing adjacent time instants, and all the unknown fields in each cell can be represented by the known fields in adjacent cells. Then, at each time step, using the leap-frog technique, the magnetic fields in each cell are calculated first and are then used to update the electric fields. Hence all the fields are calculated explicitly at each time step, and the solution can be obtained after the requisite number of time steps. Of course the size of the time step is restricted after setting the spatial step according to the CFL condition to ensure stability; the FDTD solution requires a minimum number of time steps. If the CFLN exceeds one, the amplification factor of the FDTD algorithm also exceeds one, leading to an unstable solution.

In recent decades a number of implicit FDTD methods have been developed to eliminate the CFL condition. At each time step of the implicit algorithm, the electric and magnetic fields are known at the same time instant. By substitution, one of these fields can be obtained by matrix solution, and the other can be updated algebraically and explicitly. In most of the implicit FDTD methods, the amplification factors are forced to be equal to or less than one. Consequently, these implicit methods are stable for any CFLN. In the following sections, five popular implicit FDTD methods are discussed.

## 2.3 FDTD using Crank-Nicolson scheme

### 2.3.1 2D CNDG

In Sun and Trueman (2003), a 2D Crank-Nicolson FDTD algorithm was developed. During the discretization procedure the electric fields and magnetic fields are first specified at the same time instant, and the fields at the intermediate time instant are thereafter approximated by the average of the fields at the next future time instant and the immediately preceding time instant.

In the $TE_z$ case, the electric fields $E_x$ and $E_y$ are expressed in terms of $H_z$. After

discretization by substituting $E_x$ and $E_y$ back into $H_z$, a new equation for $H_z$ is obtained in which the terms of $H_z$ at the next future time instant can be grouped. Through the Douglas-Gunn (DG) algorithm the coefficients of $H_z$ form two tridiagonal matrices, and $H_z$ at the future time instant can then be obtained by matrix solution. A similar procedure yields the result in the two dimensional $TM_z$ case. The Crank-Nicolson-Douglas-Gunn (CNDG) algorithm is among the most accurate for the two-dimensional case, but there is no clear way to extend it to the three-dimensional case.

### 2.3.2 3D CNDS and CNCSU

Application of the 3D Crank-Nicolson scheme yields six equations for the electric fields and magnetic fields. For example, $E_x$ is represented by $H_x$ and $H_y$; $E_y$ is represented by $H_x$ and $H_z$; $H_z$ is represented by $E_x$ and $E_y$. Substitution of $E_x$ and $E_y$ into $H_z$ yields an equation which includes three unknowns: $H_x$, $H_y$ and $H_z$. The coefficients of all the unknowns therefore form a dense matrix, causing the Douglas-Gunn algorithm to fail. Matrix solution becomes impractical in this case, because it is extremely time-consuming.

In Sun and Trueman (2006), two 3D Crank-Nicolson-type algorithms have been proposed. The Crank-Nicolson direct-splitting (CNDS) method deals with the difference operators in matrix form. The matrix is divided into two matrices, each consisting of half of the original operators. After application of the Crank-Nicolson scheme and some manipulation, each electric field can be obtained by a two-step procedure at each time instant. At the first step, an intermediate field is calculated from the fields at the past time instant, and this can be used to determine the field at the future time instant at the second step. In both steps the coefficient matrices are products of two tridiagonal matrices, rather than dense matrices, and matrix solution is once again realistic. After that, the magnetic fields are computed explicitly. The amplification factor is unity, and the CNDS algorithm is therefore unconditionally stable, although the numerical dispersion tends to be larger than in the conventional Crank-Nicolson scheme. To reduce the anisotropy, another algorithm was

proposed, as follows.

The Crank-Nicolson-cycle sweep-uniform (CNCSU) method was developed by Sun and Trueman (2006). The algorithm is similar to the CNDS method, but the matrix of difference operators is split in a different way. Specifically, the electric fields are updated implicitly and the magnetic fields are then calculated explicitly. By choosing the Courant number appropriately, the CNCSU method turns out to be as accurate in terms of isotropy as the conventional Crank-Nicolson scheme. It is not necessarily stable, however. When the CFLN exceeds a certain value, the method tends to be unstable. The allowable maximum CFLN for accuracy is smaller than that for stability, so that, as the CFLN increases, the result becomes inaccurate before it becomes unstable. Therefore the CNCSU method is considered unconditionally stable.

## 2.4 Split-Step FDTD

In Lee and Fornberg (2003) a split-step technique has been proposed to solve the three-dimensional Maxwell's equations. The matrix of difference operators is split into two sub-matrices, a positive operator matrix $A$ and a negative operator matrix $B$. The split-step technique involves two distinct calculations, written as $\partial u/\partial t = Au$ and $\partial u/\partial t = Bu$, where $u = [E_x, E_y, E_z, H_x, H_y, H_z]^T$. The entire procedure can be divided into several steps; at each step, one of these two calculations is implemented. In the first, involving $A$, each electric field is coupled with a magnetic field to set up a pair of equations, so that three pairs of equations are involved in total. For each pair, application of the Crank-Nicolson algorithm and substitution of the equation for the magnetic field into the other equation yields an equation in which the coefficients of the electric field at the future time instant are governed by a tridiagonal matrix. The electric field can be obtained by matrix solution, and the magnetic field is then computed explicitly.

Based on the requirements of accuracy and simulation time, the number of steps is chosen within a certain range. A larger number of steps leads to more accurate results but

suffers from longer simulation times. As a balance between the two requirements, most of the following research focuses on the four-step and six-step methods. In Kong and Chu (2010a), both methods are discussed. The four-step and six-step methods both outperform the conventional alternating-direction-implicit FDTD, with shorter simulation time and greater accuracy.

## 2.5 Alternating-Direction-Implicit FDTD

The Alternating-Direction-Implicit FDTD algorithm is one of the most popular implicit FDTD methods, and was first proposed by Takefumi Namiki. In Namiki (1999), the 2D ADI-FDTD formulation was derived. At each time step the calculation consists of two sub-steps. An intermediate field is defined for each electric and magnetic field component. In the 2D $TE_Z$ example, the intermediate magnetic field is solved implicitly using the intermediate electric fields. The coefficient matrix of the unknowns is tridiagonal, and the implicit equations can therefore be solved without much expenditure of computer time. After that, the intermediate magnetic fields are updated explicitly. Similarly, in the second sub-step, the fields at the future time instant can be obtained from the intermediate fields and the fields at the previous time instant. The amplification factor of the ADI-FDTD is equal to one, confirming its unconditional stability. The numerical experiment demonstrates that the ADI-FDTD with large CFLN is much more computationally effective than the explicit FDTD.

In Namiki (2000) the 3D ADI-FDTD formulation is presented. As in the 2D-ADI, two sub-steps are required at each time step. In the first sub-step, an intermediate field is defined for each of the electric and magnetic fields. By substituting the magnetic fields into the electric field equation, the intermediate electric field can be determined implicitly. The intermediate magnetic field is then updated. In the second sub-step, the fields at the future time instant is calculated by substituting in the intermediate fields. The 3D ADI-FDTD preserves unconditional stability and also outperforms the conventional explicit FDTD in

terms of computational time. In fact, if the spatial step size is much smaller than the wavelength, a much larger time step is possible without unacceptable numerical errors.

With $U = [E_x\ E_y\ E_z\ H_x\ H_y\ H_z]^T$ and $S = [-\frac{1}{\mu}M_x\ -\frac{1}{\mu}M_y\ -\frac{1}{\mu}M_z\ -\frac{1}{\epsilon}J_x\ -\frac{1}{\epsilon}J_y\ -\frac{1}{\epsilon}J_z]^T$, Maxwell's equations can be represented as

$$\frac{\partial}{\partial t}U = MU + S. \tag{2.17}$$

The two matrices representing operators $A$ and $B$ are defined as

$$A = \begin{bmatrix} 0 & 0 & 0 & 0 & 0 & \frac{1}{\mu}\frac{\partial}{\partial y} \\ 0 & 0 & 0 & \frac{1}{\mu}\frac{\partial}{\partial z} & 0 & 0 \\ 0 & 0 & 0 & 0 & \frac{1}{\mu}\frac{\partial}{\partial x} & 0 \\ 0 & \frac{1}{\epsilon}\frac{\partial}{\partial z} & 0 & 0 & 0 & 0 \\ 0 & 0 & \frac{1}{\epsilon}\frac{\partial}{\partial x} & 0 & 0 & 0 \\ \frac{1}{\epsilon}\frac{\partial}{\partial y} & 0 & 0 & 0 & 0 & 0 \end{bmatrix},$$

$$B = \begin{bmatrix} 0 & 0 & 0 & 0 & -\frac{1}{\mu}\frac{\partial}{\partial z} & 0 \\ 0 & 0 & 0 & 0 & 0 & -\frac{1}{\mu}\frac{\partial}{\partial x} \\ 0 & 0 & 0 & -\frac{1}{\mu}\frac{\partial}{\partial y} & 0 & 0 \\ 0 & 0 & -\frac{1}{\epsilon}\frac{\partial}{\partial y} & 0 & 0 & 0 \\ -\frac{1}{\epsilon}\frac{\partial}{\partial z} & 0 & 0 & 0 & 0 & 0 \\ 0 & -\frac{1}{\epsilon}\frac{\partial}{\partial x} & 0 & 0 & 0 & 0 \end{bmatrix}.$$

Then the ADI-FDTD algorithm is represented by

$$\left(I - \frac{\Delta t}{2}A\right)U|^{n+\frac{1}{2}} = \left(I + \frac{\Delta t}{2}B\right)U|^{n}, \tag{2.18}$$

$$\left(I - \frac{\Delta t}{2}B\right)U|^{n+1} = \left(I + \frac{\Delta t}{2}A\right)U|^{n+\frac{1}{2}}. \tag{2.19}$$

Here the ADI-FDTD algorithm is used to solve the 3D cavity problem. The cavity is discretized with the same spatial steps and the excitation source is specified with the same parameters. Figure 2.5 shows $E_z$ at the same observation point for different values of CFLN. With CFLN= 1, the ADI-FDTD clearly yields an accurate result that is in good agreement with the FDTD solution. With CFLN= 3, the result based on the ADI-FDTD method is still stable, although at the cost of accuracy.

As the amplification factor of the overall procedure is equal to one with any time step, the ADI-FDTD is unconditionally stable. According to the sampling theorem, the time step is related to the maximum frequency of the source. A large time step can lead to inaccurate results because of undersampling, especially in situations where the source is a high-frequency one. Figure 2.6 shows $E_z$ calculated at the same observation point for the same cavity example as in Section 2.1. The source function is a modulated Gaussian, of the form

$$J_z(t) = \exp\left[-\left(\frac{t-t_0}{\sigma}\right)^2\right] \times \cos\left(2\pi f_0 t\right), \tag{2.20}$$

where the center frequency $f_0 = 100\ M\text{Hz}$. For CFLN= 3, large errors are visible due to undersampling, especially after the reflected wave from the PEC boundaries is involved. Because of the high carrier frequency, the field changes rapidly and the phase error quickly accumulates until, after 240 $n$s, the ADI-FDTD solution becomes inaccurate.

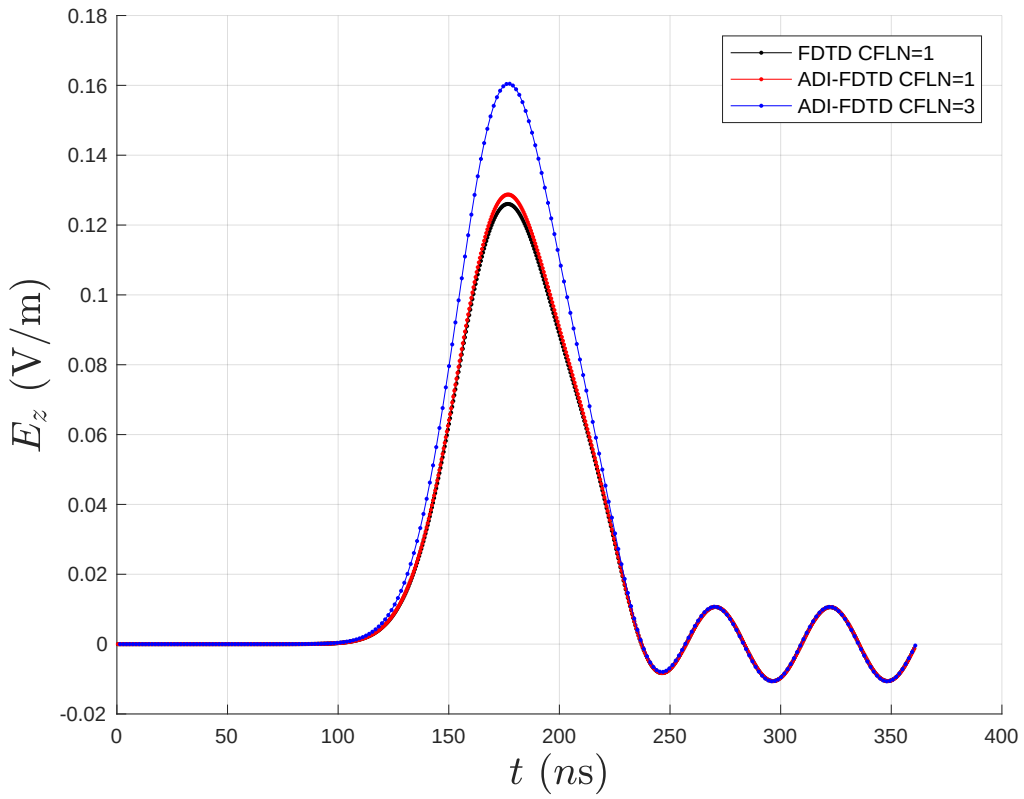


Figure 2.5. $E_z$ at the observation point calculated by the 3D classical FDTD and ADI-FDTD methods for different values of CFLN.

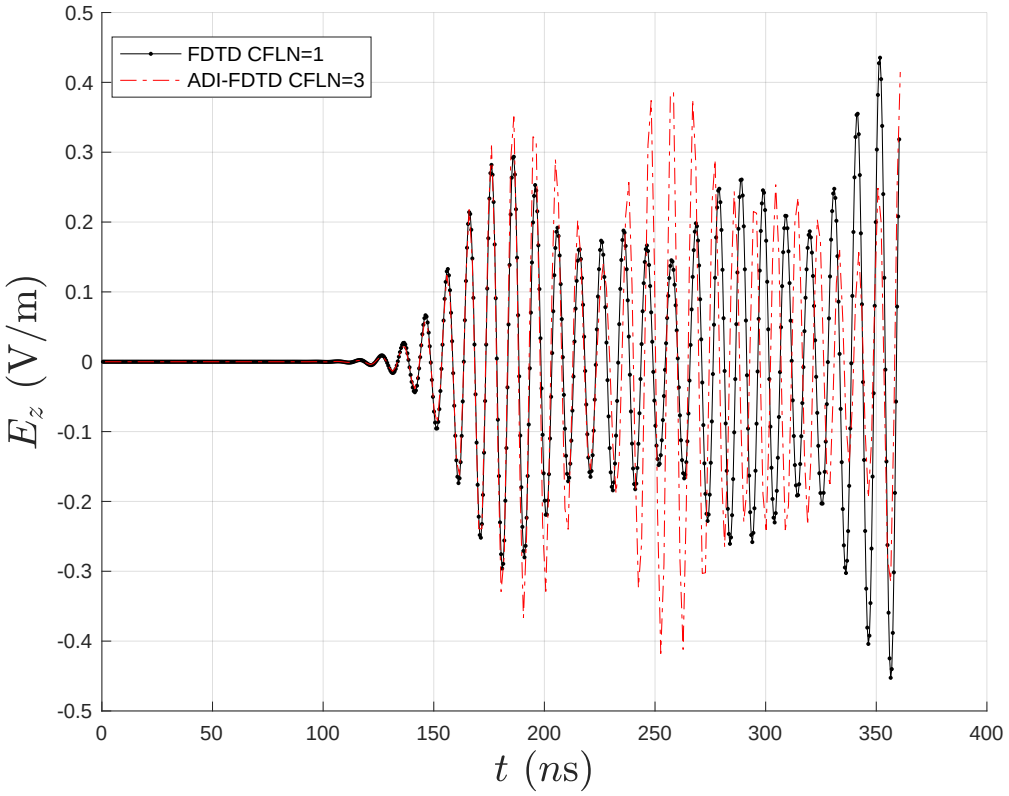


Figure 2.6. $E_z$ at the observation point calculated by the ADI-FDTD and FDTD methods with a band-pass limited point source

# CHAPTER 3

## COMPLEX-ENVELOPE IMPLICIT FDTD

According to the Nyquist-Shannon sampling theorem, the maximum time step is constrained by the maximum frequency of the signal. Hence for an implicit FDTD algorithm excited by a bandpass-limited (BPL) source, the time step must still be sufficiently small to provide accuracy. In this case the benefit of choosing an implicit FDTD algorithm diminishes as the carrier frequency of the source increases. With a BPL source, as the time step exceeds a threshold value the implicit algorithm is stable but not accurate.

To overcome this disadvantage in the case of a bandpass-limited source, the complex-envelope (CE) FDTD technique was proposed in Pursel and Goggans (1999). After applying the CE, the carrier frequency of the signal is shifted to zero, so that the BPL source is transformed to a complex lowpass-limited (LPL) signal such that the maximum frequency is half the bandwidth. With a narrow-band signal, the maximum frequency is reduced more with the complex envelope. A set of modified Maxwell's equations is developed paying due regard to the differential operator with respect to time; the field components are all multiplied by an exponential function $e^{j\omega_0 t}$ due to the CE, which adds a further term in each equation, stemming from the differential operator. With this additional term, the modified Maxwell's equation can be solved in two ways, either by using complex field components or real field components.

To solve the modified Maxwell's equations using complex field components it is necessary to discretize all of the complex field components in time directly. This necessitates representation of the additional term at the intermediate time instant, and this is unknown and difficult to calculate. The knowns in the equation are all at the preceding time instant,

whereas all of the unknowns are at the future time instant. The additional term can therefore be represented by the average of the corresponding term at the past time instant and that at the future time instant. Then the unknown terms at the future time are grouped together while the terms at the past time instant are placed on the right hand side of the equation.

The alternative is to solve the modified Maxwell's equation using real field components. The complex field components are written explicitly in terms of their real and imaginary parts. Then the original equations are decomposed into two sets of equations by taking their real and imaginary parts. The two sets of equations are discretized at different time instants so that the leap-frog technique can be used. Further details are discussed with some implicit methods, as follows.

## 3.1 Complex-Envelope Representation

A real band-pass limited signal with bandwidth $B$ can be represented as

$$x(t) = A(t)\cos\left[2\pi f_0 t + \phi(t)\right], \tag{3.1}$$

where $f_0$ is the center frequency, $A(t)$ is the amplitude and $\phi(t)$ is the phase. Equation (3.1) can be rewritten as

$$x(t) = \Re\Big\{A(t)\exp\left[j\phi(t)\right]\exp\left[j2\pi f_0 t\right]\Big\}. \tag{3.2}$$

The complex-envelope representation of $x(t)$ is

$$\tilde{x}(t) = A(t)\exp\left[j\phi(t)\right] = x^p(t) + jx^q(t), \tag{3.3}$$

where $x_p(t)$ and $x_q(t)$ are the in-phase and quadrature portions of $x(t)$. Both of $x_p(t)$ and $x_q(t)$ are low-pass limited with bandwidth $B/2$. Substitution of (3.3) into (3.2) yields

$$x(t) = \Re\Big\{\tilde{x}(t)\exp\left[j2\pi f_0 t\right]\Big\}, \tag{3.4}$$

or

$$x(t) = \Re\Big\{ [x^p(t) + jx^q(t)][\cos(2\pi f_0 t) + j\sin(2\pi f_0 t)] \Big\}. \tag{3.5}$$

In Haykin (1983) and Pursel and Goggans (1999) the bandpass-limited signal $x(t)$ can be expressed as

$$x(t) = x^p(t)\cos(2\pi f_0 t) - x^q(t)\sin(2\pi f_0 t). \tag{3.6}$$

The bandwidth of center frequency of $x(t)$ can be expressed as

$$B = f_{max} - f_{min} \tag{3.7}$$

and

$$f_0 = \frac{f_{max} + f_{min}}{2}, \tag{3.8}$$

where $f_{max}$ and $f_{min}$ are the maximum and minimum frequencies in $x(t)$.

To understand the relation between the Fourier transform of $x(t)$ and the Fourier transform of $\tilde{x}(t)$, it is useful to introduce the pre-envelope, $x_+(t)$, and the Hilbert transform, $\hat{x}(t)$, of $x(t)$. They are related by the expression

$$x_+(t) = x(t) + j\hat{x}(t). \tag{3.9}$$

Consider now the Hilbert Transform pairs

$$H\{a(t)\cos(2\pi f_0 t)\} = a(t)\sin(2\pi f_0 t) \tag{3.10}$$

and

$$H\{a(t)\sin(2\pi f_0 t)\} = -a(t)\cos(2\pi f_0 t), \tag{3.11}$$

where $H\{\}$ is the Hilbert Transform operation. Substitution of (3.6) into (3.9) yields

$$\begin{aligned} x_+(t) &= \Big\{x^p(t)\cos(2\pi f_0 t) - x^q(t)\sin(2\pi f_0 t)\Big\} + jH\Big\{x^p(t)\cos(2\pi f_0 t) - x^q(t)\sin(2\pi f_0 t)\Big\} \\ &= \Big\{x^p(t)\cos(2\pi f_o t) - x^q(t)\sin(2\pi f_0 t)\Big\} + j\Big\{x^p(t)\sin(2\pi f_o t) + x^q(t)\cos(2\pi f_0 t)\Big\} \\ &= \Big\{x^p(t) + jx^q(t)\Big\}\Big\{\cos(2\pi f_0 t) + j\sin(2\pi f_0 t)\Big\} \\ &= \tilde{x}(t)\mathrm{e}^{j2\pi f_0 t}. \end{aligned} \tag{3.12}$$

The standard engineering definition of Fourier Transform is used, such that

$$X(f) = \int_{-\infty}^{\infty} x(t)\mathrm{e}^{-j2\pi ft}dt \tag{3.13}$$

and

$$x(t) = \int_{-\infty}^{\infty} X(f)\mathrm{e}^{j2\pi ft}dt. \tag{3.14}$$

The Fourier transform of the complex envelope signal is then obtained as

$$\begin{aligned} \tilde{X}(f) &= F\{\tilde{x}(t)\} \\ &= F\{x_+(t)\mathrm{e}^{-j2\pi f_0 t}\} \\ &= F\left\{x(t)\mathrm{e}^{-j2\pi f_0 t} + j\hat{x}(t)\mathrm{e}^{-j2\pi f_0 t}\right\} \\ &= X(f+f_0) + jF\left\{\left[x(t)\otimes\frac{1}{\pi t}\right]\mathrm{e}^{-j2\pi f_0 t}\right\} \\ &= X(f+f_0) + j\{X(f+f_0)\cdot[-j\mathrm{sgn}(f+f_0)]\} \\ &= X(f+f_0) + \{X(f+f_0)\cdot\mathrm{sgn}(f+f_0)\}, \end{aligned} \tag{3.15}$$

where

$$\mathrm{sgn}(f) = \begin{cases} 1, & \text{if } f > 0; \\ 0, & \text{if } f = 0; \\ -1, & \text{if } f < 0. \end{cases} \tag{3.16}$$

From (3.15) and (3.16), the relation between $X(f)$ and $\tilde{X}(f)$ can be written as

$$\tilde{X}(f) = \begin{cases} 2X(f + f_0) & \text{if } f + f_0 > 0 \\ 0 & \text{if } f + f_0 \leq 0. \end{cases} \tag{3.17}$$

Thus, in the frequency domain, $\tilde{X}(f)$ is the positive part of $X(f)$ with double magnitude after shifting down to the baseband with a center frequency of zero. This process is illustrated in Figure 3.1 and Figure 3.2.

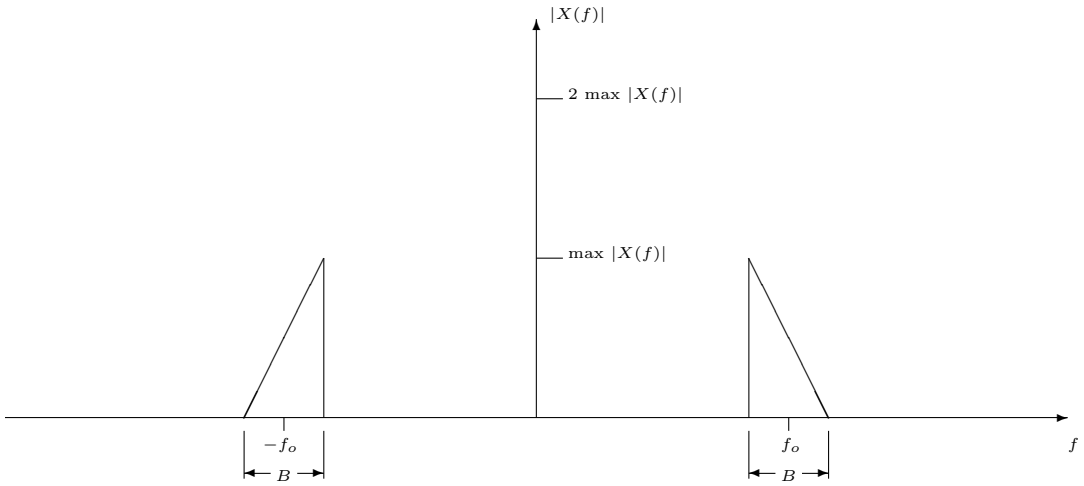


Figure 3.1. The frequency spectrum of a real bandpass-limited signal $X(f)$.

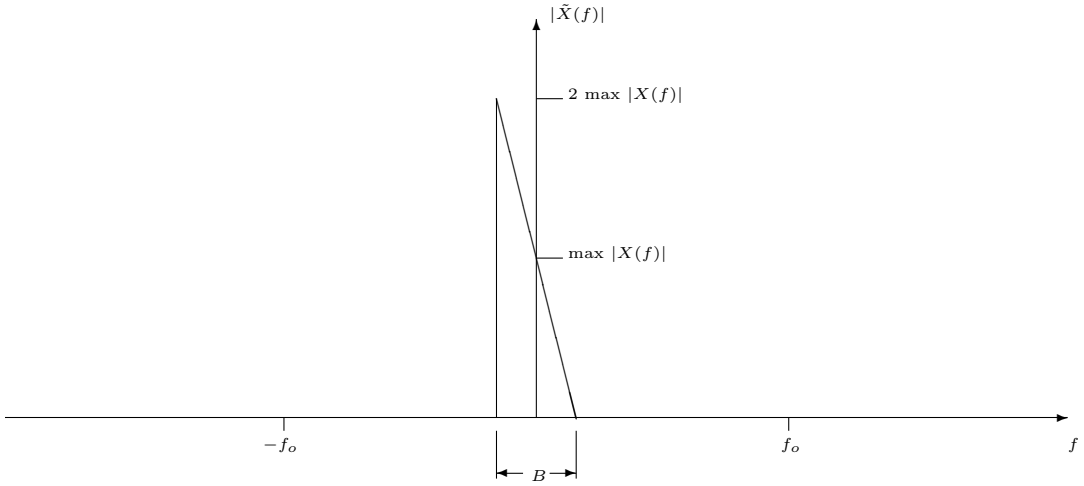


Figure 3.2. The frequency spectrum of the complex envelope of the real bandpass-limited signal $\tilde{X}(f)$.

## 3.2 Complex-Envelope Crank-Nicolson FDTD

The coefficients of the unknowns in the CN-FDTD formulation follows the pattern $1 + D_A + D_B$, where $D_A$ and $D_B$ respectively denote the second derivatives with respect

to space along orthogonal directions. The implicit computation is difficult to performed, because the coefficient matrix is a dense matrix rather than tridiagonal. In high dimensional FDTD, therefore, a CN scheme is always used with the Douglas-Gunn (DG) algorithm, in Sun and Trueman (2003). Specifically, the DG algorithm has the differential operator term $D_A D_B$ on the left hand side of the equation such that the coefficient of the unknown field component at the future time instant is changed to $1 + D_A + D_B + D_A D_B$, which is equal to $(1 + D_A)(1 + D_B)$. An identical $D_A D_B$ term acting on the same field component at the past time instant must correspondingly be added to the right hand side of the equation. In computation, $1 + D_A$ and $1 + D_B$ are represented by tridiagonal matrices, so that the unknown field component can readily be obtained by matrix solution.

After applying CE and discretizing the complex field component, however, the coefficients of the unknown fields no longer follow the pattern $1 + D_A + D_B$, and the DG algorithm cannot therefore be readily applied. It follows that CE CN FDTD computation must be performed using real field components.

### 3.2.1 2D CE-CN-FDTD

A two-dimensional complex-envelope FDTD formulation using alternating in-phase and quadrature field variables was proposed by Goggans and Liu (2015). The complex field components are decomposed into an in-phase part (the real part) and a quadrature part (the imaginary part). Collection of the real terms yields one set of equations, and correspondingly with the imaginary terms. At each time step during computation, in the first set of equations the unknowns are at the future time instant, whereas the unknowns in the second set of equations are at the 1/2 time instant before. The unknowns in the second set of equations are therefore calculated first, and can then be used to obtain the unknowns in the first set of equations. At the next time step, the unknowns in the first set of equations from the previous time step can be used to calculate the unknowns in the second set of equations. The in-phase part and quadrature part of the complex field components

can thereby be obtained at each successive time increment as time marches forward. The algorithm maintains high computational effectiveness and accuracy.

### 3.2.2 3D CE-CN-FDTD

The alternating in-phase and quadrature method has been used in 3D CNDS and CNCSU according to Sun and Trueman (2006). The additional term from the CE in each equation is known and serves as part of the source, and the rest of the equation preserves the same equation structure as in conventional CNDS and CNCSU. At each time step, the quadrature parts of the fields are calculated first, and then substituted into the other set of equations. The in-phase part of the fields are then calculated. The final numerical results show instability with a Courant number larger than one. If the Courant number is less than or equal to one, the result is stable but not particularly accurate, suggesting incompatibility between CNDS/CNCSU and CE.

## 3.3 Complex-Envelope Four-Stage Split-Step FDTD

An unconditionally-stable three-dimensional four-stage split-step FDTD method was presented in Kong and Chu (2009). Numerical results show that the simulation time is reduced by 30% relative to the conventional ADI-FDTD method, while the accuracy is maintained at the same level. This is therefore a candidate for application of the CE algorithm.

The complex-envelope four-stage split-step (CE-4S-SS) FDTD is expressed via six modified Maxwell's equations, which can be solved in matrix form $\partial U/\partial t + j\omega_0 U = MU$, where $U = [E_x E_y E_z H_x H_y H_z]^T$ and $M$ is the matrix of differential operators. $M$ is divided into two sub-matrices $A$ and $B$ such that $M = A + B$, where $A$ consists of all positive differential operators and $B$ contains all negative differential operators. At each time step the calculation is decomposed into four procedures, which are performed in the following order. In the first procedure, the intermediate field components at time instant $n + 1/4$ are calculated according to $\partial U/\partial t + j\omega_0 U = AU$. In the second procedure, the intermediate field

components at time instant $n+2/4$ are calculated according to $\partial U/\partial t + j\omega_0 U = BU$. In the third procedure, the intermediate field components at time instant $n+3/4$ are calculated according to $\partial U/\partial t + j\omega_0 U = AU$, and in the final procedure the field components at time instant $n+1$ are calculated according to $\partial U/\partial t + j\omega_0 U = BU$. The equations can be solved by using real field components or by using imaginary field components as introduced above.

Numerical results reveal that the solution using real field components is unstable. With CFLN$\leq$ 1 the result is stable; but, as the CFLN increases and exceeds one, the results become unstable and exhibit exponential growth of numerical instabilities.

The solution using complex field components, in contrast, yields stable results with arbitrary Courant number, although as CFLN increases, the accuracy of the results degrades rapidly, so that little simulation time is saved.

In summary, no matter how the modified equations are solved, the solution in 3D involving the CE-4S-SS FDTD turns out to be either inaccurate or unstable, and the method is therefore of limited practical use.

## 3.4 Complex-Envelope Alternating-Direction-Implicit FDTD

The complex-envelope Alternating-Direction-Implicit FDTD (CE-ADI-FDTD) scheme was developed by Ma and Chen (2005). By adapting the CE to the conventional ADI FDTD a set of modified Maxwell's equations arises, which can be solve using complex field components. These CE Maxwell's equations are written as

$$\nabla \times \tilde{\mathbf{H}} = \epsilon \frac{\partial \tilde{\mathbf{E}}}{\partial t} + j\omega_0 \epsilon \tilde{\mathbf{E}} + \tilde{\mathbf{J}}, \tag{3.18}$$

$$\nabla \times \tilde{\mathbf{E}} = -\mu \frac{\partial \tilde{\mathbf{H}}}{\partial t} - j\omega_0 \mu \tilde{\mathbf{H}} - \tilde{\mathbf{M}}. \tag{3.19}$$

The calculation is divided into two steps. In the first step the fields at the intermediate time instant $U^{n+1/2}$are calculated by:

$$\frac{4+j\omega_0\Delta t}{4}\tilde{E}_x|^{n+\frac{1}{2}} - \frac{\Delta t}{2\epsilon}\frac{\partial}{\partial y}\tilde{H}_z|^{n+\frac{1}{2}} = \frac{4-j\omega_0\Delta t}{4}\tilde{E}_x|^{n} - \frac{\Delta t}{2\epsilon}\frac{\partial}{\partial z}\tilde{H}_y|^{n} - \frac{\Delta t}{2\epsilon}\tilde{J}_x|^{n+\frac{1}{4}}, \quad (3.20)$$

$$\frac{4+j\omega_0\Delta t}{4}\tilde{E}_y|^{n+\frac{1}{2}} - \frac{\Delta t}{2\epsilon}\frac{\partial}{\partial z}\tilde{H}_x|^{n+\frac{1}{2}} = \frac{4-j\omega_0\Delta t}{4}\tilde{E}_y|^{n} - \frac{\Delta t}{2\epsilon}\frac{\partial}{\partial x}\tilde{H}_z|^{n} - \frac{\Delta t}{2\epsilon}\tilde{J}_y|^{n+\frac{1}{4}}, \quad (3.21)$$

$$\frac{4+j\omega_0\Delta t}{4}\tilde{E}_z|^{n+\frac{1}{2}} - \frac{\Delta t}{2\epsilon}\frac{\partial}{\partial x}\tilde{H}_y|^{n+\frac{1}{2}} = \frac{4-j\omega_0\Delta t}{4}\tilde{E}_z|^{n} - \frac{\Delta t}{2\epsilon}\frac{\partial}{\partial y}\tilde{H}_x|^{n} - \frac{\Delta t}{2\epsilon}\tilde{J}_z|^{n+\frac{1}{4}}, \quad (3.22)$$

$$\frac{4+j\omega_0\Delta t}{4}\tilde{H}_x|^{n+\frac{1}{2}} - \frac{\Delta t}{2\mu}\frac{\partial}{\partial z}\tilde{E}_y|^{n+\frac{1}{2}} = \frac{4-j\omega_0\Delta t}{4}\tilde{H}_x|^{n} - \frac{\Delta t}{2\mu}\frac{\partial}{\partial y}\tilde{E}_z|^{n} - \frac{\Delta t}{2\mu}\tilde{M}_x|^{n+\frac{1}{4}}, \quad (3.23)$$

$$\frac{4+j\omega_0\Delta t}{4}\tilde{H}_y|^{n+\frac{1}{2}} - \frac{\Delta t}{2\mu}\frac{\partial}{\partial x}\tilde{E}_z|^{n+\frac{1}{2}} = \frac{4-j\omega_0\Delta t}{4}\tilde{H}_y|^{n} - \frac{\Delta t}{2\mu}\frac{\partial}{\partial z}\tilde{E}_x|^{n} - \frac{\Delta t}{2\mu}\tilde{M}_y|^{n+\frac{1}{4}}, \quad (3.24)$$

$$\frac{4+j\omega_0\Delta t}{4}\tilde{H}_z|^{n+\frac{1}{2}} - \frac{\Delta t}{2\mu}\frac{\partial}{\partial y}\tilde{E}_x|^{n+\frac{1}{2}} = \frac{4-j\omega_0\Delta t}{4}\tilde{H}_z|^{n} - \frac{\Delta t}{2\mu}\frac{\partial}{\partial z}\tilde{E}_y|^{n} - \frac{\Delta t}{2\mu}\tilde{M}_z|^{n+\frac{1}{4}}. \quad (3.25)$$

In the second step the fields at the future time instant are calculated by:

$$\frac{4+j\omega_0\Delta t}{4}\tilde{E}_x|^{n+1} + \frac{\Delta t}{2\epsilon}\frac{\partial}{\partial z}\tilde{H}_y|^{n+1} = \frac{4-j\omega_0\Delta t}{4}\tilde{E}_x|^{n+\frac{1}{2}} + \frac{\Delta t}{2\epsilon}\frac{\partial}{\partial y}\tilde{H}_z|^{n+\frac{1}{2}} - \frac{\Delta t}{2\epsilon}\tilde{J}_x|^{n+\frac{3}{4}}, \quad (3.26)$$

$$\frac{4+j\omega_0\Delta t}{4}\tilde{E}_y|^{n+1}+\frac{\Delta t}{2\epsilon}\frac{\partial}{\partial x}\tilde{H}_z|^{n+1}=\frac{4-j\omega_0\Delta t}{4}\tilde{E}_y|^{n+\frac{1}{2}}+\frac{\Delta t}{2\epsilon}\frac{\partial}{\partial z}\tilde{H}_x|^{n+\frac{1}{2}}-\frac{\Delta t}{2\epsilon}\tilde{J}_y|^{n+\frac{3}{4}}, \quad (3.27)$$

$$\frac{4+j\omega_0\Delta t}{4}\tilde{E}_z|^{n+1}+\frac{\Delta t}{2\epsilon}\frac{\partial}{\partial y}\tilde{H}_x|^{n+1}=\frac{4-j\omega_0\Delta t}{4}\tilde{E}_z|^{n+\frac{1}{2}}+\frac{\Delta t}{2\epsilon}\frac{\partial}{\partial x}\tilde{H}_y|^{n+\frac{1}{2}}-\frac{\Delta t}{2\epsilon}\tilde{J}_z|^{n+\frac{3}{4}}, \quad (3.28)$$

$$\frac{4+j\omega_0\Delta t}{4}\tilde{H}_x|^{n+1}+\frac{\Delta t}{2\mu}\frac{\partial}{\partial y}\tilde{E}_z|^{n+1}=\frac{4-j\omega_0\Delta t}{4}\tilde{H}_x|^{n+\frac{1}{2}}+\frac{\Delta t}{2\mu}\frac{\partial}{\partial z}\tilde{E}_y|^{n+\frac{1}{2}}-\frac{\Delta t}{2\mu}\tilde{M}_x|^{n+\frac{3}{4}}, \quad (3.29)$$

$$\frac{4+j\omega_0\Delta t}{4}\tilde{H}_y|^{n+1}+\frac{\Delta t}{2\mu}\frac{\partial}{\partial z}\tilde{E}_x|^{n+1}=\frac{4-j\omega_0\Delta t}{4}\tilde{H}_y|^{n+\frac{1}{2}}+\frac{\Delta t}{2\mu}\frac{\partial}{\partial x}\tilde{E}_z|^{n+\frac{1}{2}}-\frac{\Delta t}{2\mu}\tilde{M}_y|^{n+\frac{3}{4}}, \quad (3.30)$$

$$\frac{4+j\omega_0\Delta t}{4}\tilde{H}_z|^{n+1}+\frac{\Delta t}{2\mu}\frac{\partial}{\partial x}\tilde{E}_y|^{n+1}=\frac{4-j\omega_0\Delta t}{4}\tilde{H}_z|^{n+\frac{1}{2}}+\frac{\Delta t}{2\mu}\frac{\partial}{\partial y}\tilde{E}_x|^{n+\frac{1}{2}}-\frac{\Delta t}{2\mu}\tilde{M}_z|^{n+\frac{3}{4}}. \quad (3.31)$$

In each step the equations are decomposed into three pairs of equations. Both of equations in each pair contain the same two unknowns, namely the electric field in one direction and the magnetic field components in another direction. Hence, in each pair, there are two unknowns and two equations. In the first step, for instance, the discretized equations for $E_x$ and $H_z$ with $J_x = M_z = 0$ are:

$$\frac{4+j\omega_0\Delta t}{4}\tilde{E}_x|_{i,j,k}^{n+\frac{1}{2}}-\frac{\Delta t}{2\epsilon}\frac{\partial}{\partial y}\tilde{H}_z|_{i,j,k}^{n+\frac{1}{2}}=\frac{4-j\omega_0\Delta t}{4}\tilde{E}_x|_{i,j,k}^{n}-\frac{\Delta t}{2\epsilon}\frac{\partial}{\partial z}\tilde{H}_y|_{i,j,k}^{n}, \quad (3.32)$$

$$\frac{4+j\omega_0\Delta t}{4}\tilde{H}_z|_{i,j,k}^{n+\frac{1}{2}} - \frac{\Delta t}{2\mu}\frac{\partial}{\partial y}\tilde{E}_x|_{i,j,k}^{n+\frac{1}{2}} = \frac{4-j\omega_0\Delta t}{4}\tilde{H}_z|_{i,j,k}^{n} - \frac{\Delta t}{2\mu}\frac{\partial}{\partial z}\tilde{E}_y|_{i,j,k}^{n}. \tag{3.33}$$

The spatial derivatives are approximated by the second-order accurate central difference formula in Elsherbeni and Demir (2009). As a result, (3.32) and (3.33) are written as

$$\begin{aligned}\tilde{E}_x|_{i,j,k}^{n+\frac{1}{2}} = \frac{4-j\omega_0\Delta t}{4+j\omega_0\Delta t}\tilde{E}_x|_{i,j,k}^{n} &+ \frac{4}{4+j\omega_0\Delta t}\frac{\Delta t}{2\epsilon\Delta}(\tilde{H}_z|_{i,j,k}^{n+\frac{1}{2}} - \tilde{H}_z|_{i,j-1,k}^{n+\frac{1}{2}}) \\ &- \frac{4}{4+j\omega_0\Delta t}\frac{\Delta t}{2\epsilon\Delta}(\tilde{H}_y|_{i,j,k}^{n} - \tilde{H}_z|_{i,j,k-1}^{n}),\end{aligned} \tag{3.34}$$

$$\begin{aligned}\tilde{H}_z|_{i,j,k}^{n+\frac{1}{2}} = \frac{4-j\omega_0\Delta t}{4+j\omega_0\Delta t}\tilde{H}_z|_{i,j,k}^{n} &+ \frac{4}{4+j\omega_0\Delta t}\frac{\Delta t}{2\mu\Delta}(\tilde{E}_x|_{i,j+1,k}^{n+\frac{1}{2}} - \tilde{E}_x|_{i,j,k}^{n+\frac{1}{2}}) \\ &- \frac{4}{4+j\omega_0\Delta t}\frac{\Delta t}{2\mu\Delta}(\tilde{E}_y|_{i+1,j,k}^{n} - \tilde{E}_y|_{i,j,k}^{n}).\end{aligned} \tag{3.35}$$

By defining $C_A = \frac{4}{4+j\omega_0\Delta t}\frac{\Delta t}{2\epsilon\Delta}$, $C_B = \frac{4}{4+j\omega_0\Delta t}\frac{\Delta t}{2\mu\Delta}$ and $C = \frac{4-j\omega_0\Delta t}{4+j\omega_0\Delta t}$, equations (3.34) and (3.35) are simplified as

$$\tilde{E}_x|_{i,j,k}^{n+\frac{1}{2}} = C\cdot\tilde{E}_x|_{i,j,k}^{n} + C_A\cdot(\tilde{H}_z|_{i,j,k}^{n+\frac{1}{2}} - \tilde{H}_z|_{i,j-1,k}^{n+\frac{1}{2}}) - C_B\cdot(\tilde{H}_y|_{i,j,k}^{n} - \tilde{H}_z|_{i,j,k-1}^{n}), \tag{3.36}$$

$$\tilde{H}_z|_{i,j,k}^{n+\frac{1}{2}} = C\cdot\tilde{H}_z|_{i,j,k}^{n} + C_A\cdot(\tilde{E}_x|_{i,j+1,k}^{n+\frac{1}{2}} - \tilde{E}_x|_{i,j,k}^{n+\frac{1}{2}}) - C_B\cdot(\tilde{E}_y|_{i+1,j,k}^{n} - \tilde{E}_y|_{i,j,k}^{n}). \tag{3.37}$$

Substitution of the magnetic equation (3.37) into the electric equation (3.36) yields

a new equation in which the coefficient matrix of the unknown is tridiagonal:

$$\begin{aligned}
&\tilde{E}_x|_{i,j,k}^{n+\frac{1}{2}} - C_A C_B(\tilde{E}_x|_{i,j+1,k}^{n+\frac{1}{2}} - 2\tilde{E}_x|_{i,j,k}^{n+\frac{1}{2}} - \tilde{E}_x|_{i,j-1,k}^{n+\frac{1}{2}}) \\
&= C \cdot \tilde{E}_x|_{i,j,k}^{n} - C_A C_B(\tilde{E}_y|_{i+1,j,k}^{n} - \tilde{E}_y|_{i,j,k}^{n}) + C_A C_B(\tilde{E}_y|_{i+1,j-1,k}^{n} - \tilde{E}_y|_{i,j-1,k}^{n}) \\
&\quad + C_A C(\tilde{H}_z|_{i,j,k}^{n} - \tilde{H}_z|_{i,j-1,k}^{n}) - C_A(\tilde{H}_y|_{i,j,k}^{n} - \tilde{H}_y|_{i,j,k-1}^{n}). \qquad (3.38)
\end{aligned}$$

The unknown $\tilde{E}_x|_{i,j,k}^{n+\frac{1}{2}}$ in the new equation can consequently be solved for implicitly, and then substituted into the original pair. The other unknown $\tilde{H}_z|_{i,j,k}^{n+\frac{1}{2}}$ is then obtained explicitly. In the second step, by following a similar procedure, the solution of $U^{n+1}$, the unknown at future time instants, can be obtained. Then, by implementing the algorithm at successive time steps, the fields at all time instants can be calculated.

Figure 3.3 shows the envelope of $E_z$ at the same observation point for the same 3D cavity problem excited by the BPL source as in the previous chapter. With CFLN= 3, the CE-ADI-FDTD solution is in good agreement with the FDTD solution. In Ma and Chen (2005), the CE-ADI-FDTD was shown demonstrated to be a qualified algorithm, which preserves accuracy as the CFLN increases, especially for a narrow-band problem with high center frequency and dense spatial resolution. It has been shown that the benefits can be improved by incorporating the four-stage technique and the basic scheme into the CE-ADI-FDTD methodology, as will be proposed in detail in Chapter 6.

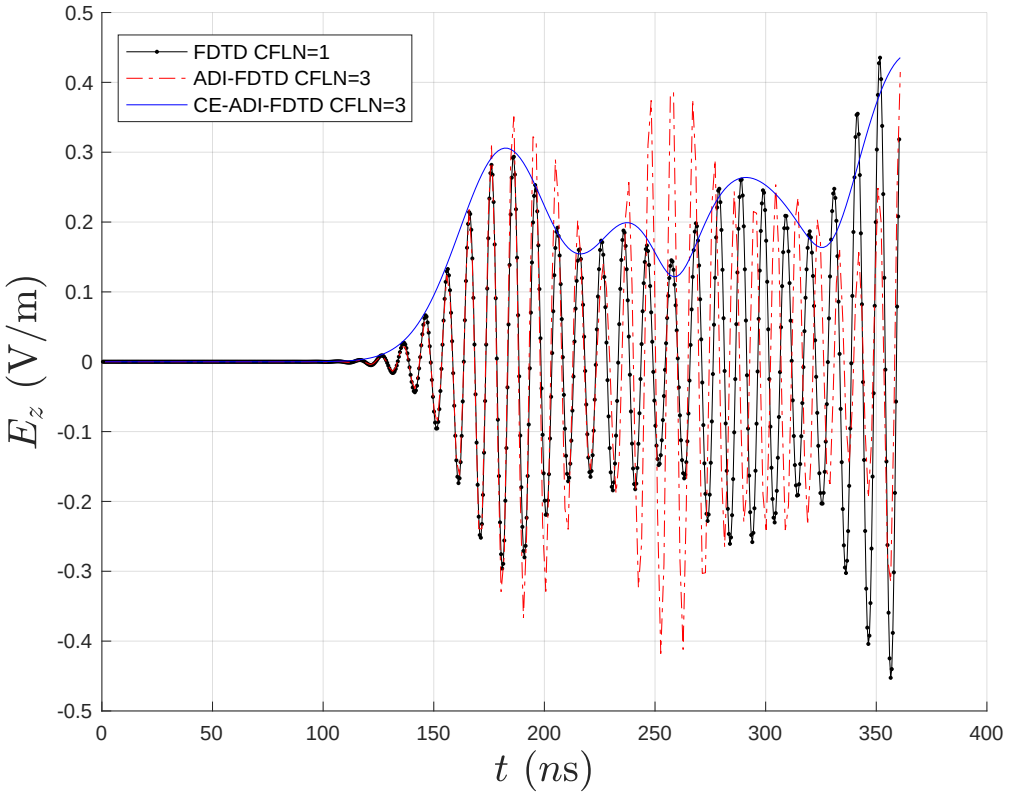


Figure 3.3. The envelope of $E_z$ recorded at the observation point based on the CE-ADI-FDTD.

# CHAPTER 4

# ABSORBING BOUNDARY CONDITIONS

Numerical analysis is necessary to tackle many problems of interest that involve cavities defined in open regions. The relevant domains are unbounded, and cannot therefore be modeled on a uniform grid. Several methods based on local absorbing boundary conditions (ABC) have been developed in recent decades to truncate the problem domain. The incident waves impinging on the boundaries are canceled out by pre-defined boundary values such that few reflection waves travel back to the simulation domain. That is, the outwardly traveling waves are expected to disappear after hitting the boundary, so that the domain of the problem can effectively be considered unbounded. Reflection errors still exist, however, and are most obvious in two-dimensional and three-dimensional problems. Furthermore, in problems that involve dispersive, inhomogeneous or anisotropic media, the performance of the local Absorbing Boundary Conditions (ABC) may be questioned. Two popular local ABC methods will be discussed later on.

A completely different approach is the perfectly matched layers (PML) technique originally proposed by Berenger (1994). Several additional layers of cells are defined on the boundaries of the computational domain, in all directions. In each additional cell, pairs of fictitious conductivities are introduced such that all waves decay as they travel in the PML region. Consequently, the incident waves begin to decay after entering the PML region from the domain modeled routinely in the computation. During propagation, the incident waves are weakened and are eventually absorbed by the PML region. Then no reflected waves enter the computational region, which can consequently be considered boundless. Three well known PML formulations will be presented below.

## 4.1 First-Order Mur Absorbing Boundary Condition

Mur ABC is based on the solution of the one-way wave equation and was introduced in Mur (1981). The three-dimensional wave equation is $\frac{\partial^2 U}{\partial x^2} + \frac{\partial^2 U}{\partial y^2} + \frac{\partial^2 U}{\partial z^2} - \frac{1}{c^2}\frac{\partial^2 U}{\partial t^2} = 0$, where $U$ is a scalar field component. The ABC's are defined based on the electric field that is tangential to the boundary.

In the first-order Mur ABC algorithm, the wave equation is approximated on the boundary by considering only the differential operator in the direction normal to the boundary. In the three-dimensional case, the ABC upon $E_z$ in the $x$ direction is given by $\frac{\partial^2 E_z}{\partial x^2} - \frac{1}{c^2}\frac{\partial^2 E_z}{\partial t^2} = 0$, which is equivalent to $(\frac{\partial E_z}{\partial x} - \frac{1}{c}\frac{\partial E_z}{\partial t})(\frac{\partial E_z}{\partial x} + \frac{1}{c}\frac{\partial E_z}{\partial t}) = 0$. For the outgoing waves, the field on the left boundary is calculated via $(\frac{\partial}{\partial x} - \frac{1}{c}\frac{\partial}{\partial t})E_z|_{x=0} = 0$. Similarly, the ABC equations for all other electric fields can be determined.

The first-order Mur ABC has been widely used in different FDTD algorithms, because of its ease of implementation. With explicit FDTD algorithms, the fields within the boundary cells are updated first, then the electric fields at the boundary itself are calculated. With implicit FDTD algorithms, the electric fields at the boundaries are represented by the field components in adjacent cells. Then a matrix solution can be determined, as in the conventional implicit FDTD algorithm. A three-dimensional conventional explicit FDTD algorithm with first-order Mur has been implemented numerically; the results demonstrate the validity of the ABC, with acceptable reflection errors.

## 4.2 Liao Extrapolation Non-reflecting Boundary Condition

In Liao (1996), the so-called Liao ABC has been developed, by which the electric field components on the boundary are calculated by extrapolation. For the same example as in the previous section, on the left boundary in the $x$ direction, $E_z|^{n+1}_{x_0,y,z} = \sum_{i=1}^{N}(-1)^{i+1}C_i^N E_z|^{n-(i-1)}_{x_0+i\Delta x,y,z}$, where $C_i^N$ is a binomial coefficient, $\Delta x$ is the spatial step in the $x$ direction, and $N$ is the order of the boundary condition.

The accuracy of Liao ABC can be improved by choosing a higher order algorithm –

a larger $N$. Unfortunately the high order Liao algorithm has poor stability. In Zhang and Yu (2012), the high order Liao ABC is weighted with a low order Liao ABC which gives an improved Liao ABC. The numerical results show that the improved Liao ABC has much smaller errors than the second order Mur ABC; however, increasing $N$ beyond 5 scarcely improves the accuracy.

### 4.3 Berenger Perfectly Matched Layers

In Berenger (1994), the two-dimensional perfectly matched layer algorithm was developed. In both the $TM_z$ and $TE_z$ cases, it was shown that the outward traveling electromagnetic waves were absorbed. The three-dimensional explicit FDTD PML formulation was given in Elsherbeni and Demir (2009). Each field component is decomposed into two parts, for example $E_z = E_{zx} + E_{zy}$. In addition, six fictitious conductivity variables are introduced in the PML region, by which the original six Maxwell's equations are converted into a new set of twelve modified equations. The PML layers are defined by adding several spatial cells in all directions. The fictitious conductivity in the PML region varies along the direction perpendicular to the interface between the PML and non-PML region; in the non-PML region, the fictitious conductivities are set to zero. Then, as in the conventional FDTD algorithm, the new equations can be solved explicitly. The calculation in the non-PML region is identical to that for the conventional explicit FDTD algorithm, because the conductivities are zero. The PML has been found to outperform the previous two local ABC, with small reflection errors. In Lin et al. (2007) the PML is also implemented in an approximate two-dimensional Crank-Nicolson scheme. The result is stable and accurate for CFLN= 4.

### 4.4 Stretched Coordinates Perfectly Matched Layers

The stretched coordinates (SC) PML formulation based on the modified Maxwell's equations in the frequency domain was introduced in Chew and Weedon (1994). It has been

shown that the SC-PML is also compatible with the 2D CNDG algorithm by Li et al. (2015). Starting with the frequency-domain modified Maxwell's equations, two auxiliary terms are defined for each component through the stretched coordinate variables and spatial differential operators. Then, after taking the inverse Fourier transform, each frequency-domain modified Maxwell's equation is decomposed into one time-domain modified Maxwell's equation and one auxiliary differential equation. After discretization the auxiliary equation is substituted into the time-domain Maxwell's equation, which can be solved using the CNDG scheme.

The results confirm that the ADE CNDG-PML algorithm preserves stability and small reflection error with a large Courant number. Furthermore, by incorporating the CE into the ADE CNDG-PML, a new CE-ADE CNDG-PML formulation is obtained, which provides accurate and stable results by using real field components.

## 4.5 Nearly Perfectly Matched Layers

Another well known and widely used PML is nearly perfectly matched layers (NPML), which was proposed in Cummer (2003). Like the SC-PML, the NPML is based on the frequency-domain modified Maxwell's equations and the inverse Fourier transform. The auxiliary variables are defined in a different way, however, such that the time-domain auxiliary equations are simpler than those in the SC PML.

It has been shown that the two-dimensional four-stages split-step (4S-SS) FDTD can be incorporated into the NPML algorithm stably and also accurately by Kong and Chu (2010b). Also, the NPML is compatible with the 2D ADI-FDTD in Ramadan (2005). Numerical results show that the ADI-FDTD with NPML is unconditionally stable, although an arbitrarily large Courant number cannot be chosen due to the greatly reduced accuracy.

Figure 4.1 shows the distribution of $E_z$ on the source plane for a 3D cavity problem similar to the example in the previous chapter. The size of the cavity is $117 \times 117 \times 117$ cells and the z-directed source is positioned at $(59, 59, 59)$, the center of the cube. The source function is

$$J_z(t) = -6 \times 10^5 \times \exp\left[-\left(\frac{t-t_0}{\sigma}\right)^2\right] \times \left(\frac{t-t_0}{\sigma}\right), \tag{4.1}$$

where $t_0 = 1.8006 \times 10^{-7}$ second and $\sigma = 3.1831 \times 10^{-8}$ second. The time step $\Delta t = 4.1667 \times 10^{-10}$ second, the spatial steps $\Delta x = \Delta y = \Delta z = 0.2498$ meter, and the observation point is 20 cells away from the source at $(39, 59, 59)$. Figure 4.1 shows the early distribution of $E_z$ on the source plane ($z = 59$). In the early stage, the distribution based on any absorbing boundary condition is the same, due to the dominant source. In $(a)$, the source just begins to excite; in $(b)$, the electric field at the source point increases due to the growth of the exponential factor in the source function; in $(c)$, the source function is near its peak, which can be seen from the magnitude of $E_z$ at the source point; in $(d)$, the simulation time is larger than $t_0$, the Gaussian delay for the peak, so that the magnitude of the electric field at the source point begins to decay.

Figure 4.2 compares the performances of the four different absorbing condition (ABC) methods. After a sufficiently long simulation time, differences appear. In $(a)$ and $(b)$, with the analytical ABC methods, there exist reflected waves from the boundaries and the corners of the cavity. In $(c)$, the incident waves and the reflected waves are absorbed in the PML region, and the interface between the computational region and the PML region is observable. In $(d)$, the reflected waves are restricted to the corners within the PML region, and scarcely enter the computational region.

Figure 4.3 shows $E_z$ recorded at the observation point based on the different methods. After the incident wave propagates through the observation point, no reflected wave is expected to be seen thereafter because of the boundary condition. The ABC methods clearly provide very good performance. After 0.3 $\mu$s, reflected waves are scarcely recorded at the observation point. The analytical solution is based on a 3D free-space Green's function and the inverse fast Fourier transform (IFFT). The analytical ABC methods are not so good at dealing with incident waves not normal to the boundaries, although it still neutralizes

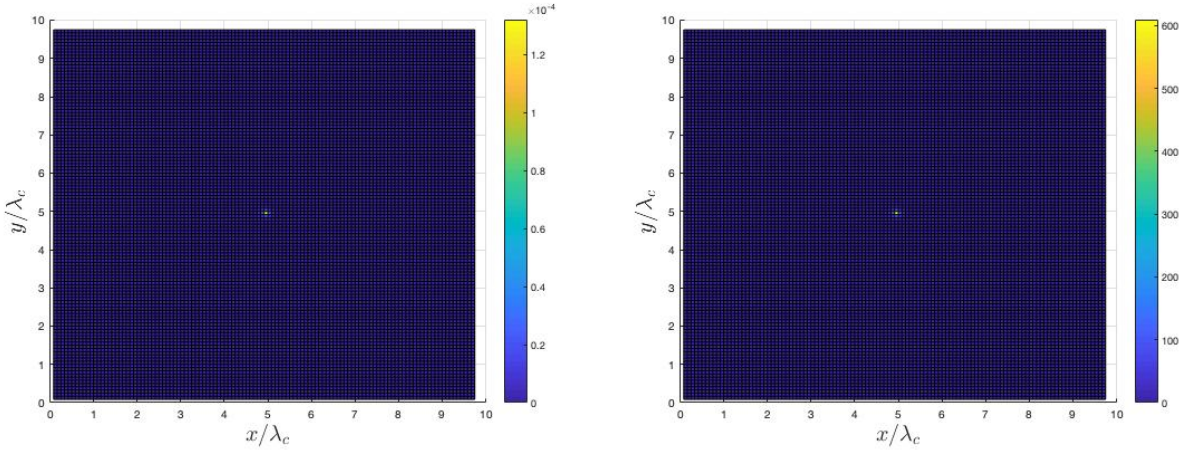


(a) $t = 0.2t_0$




(b) $t = 0.6t_0$

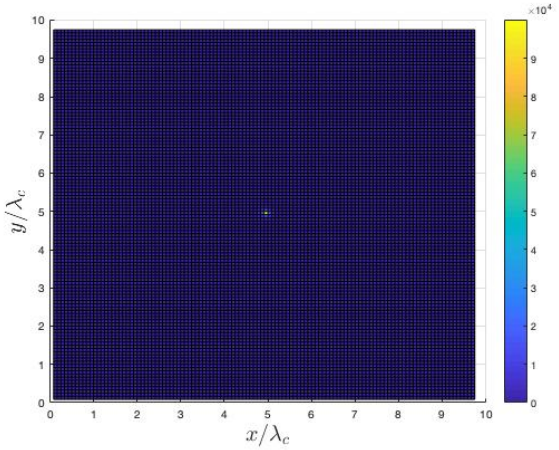


(c) $t = 1.0t_0$

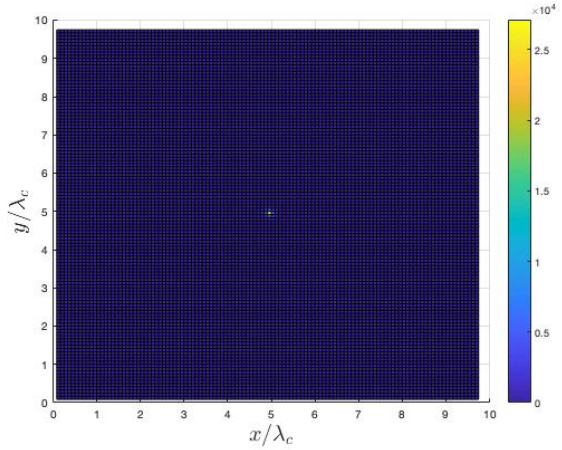


(d) $t = 1.2t_0$

Figure 4.1. The early distribution of $E_z$ on the source plane for the 3D cavity example.

the incident waves directly on the boundaries through the pre-defined boundary values. The PML and NPML algorithm create the PML region in which waves from any angle are absorbed. Nevertheless, the PML region also involves additional cells for computation, so that more computational time is required, especially in problems in more dimensions.

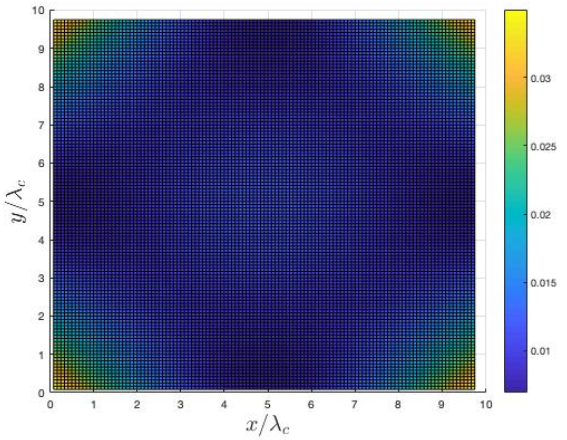


(a) 1st Mur at $t = 2.0t_0$.

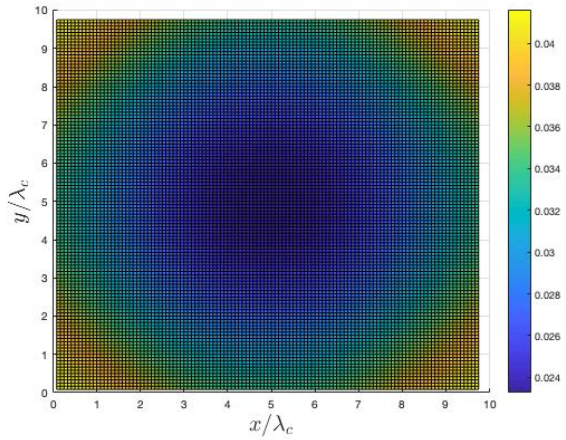


(b) Improved 5th Liao at $t = 2.0t_0$.

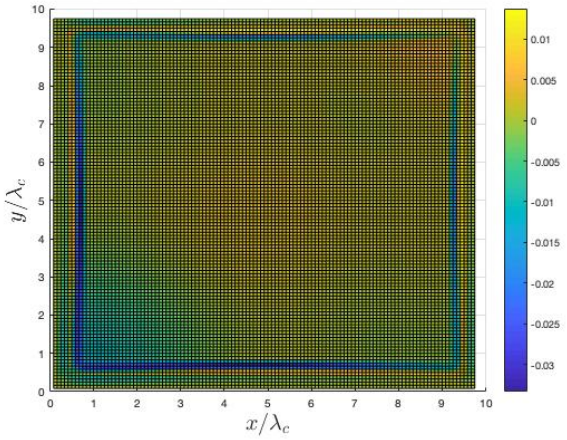


(c) PML at $t = 2.0t_0$.

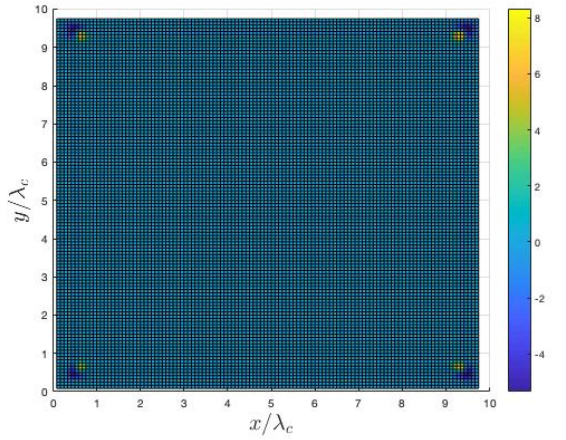


(d) NPML at $t = 2.0t_0$.

Figure 4.2. The final distribution of $E_z$ on the source plane based on different ABC's.

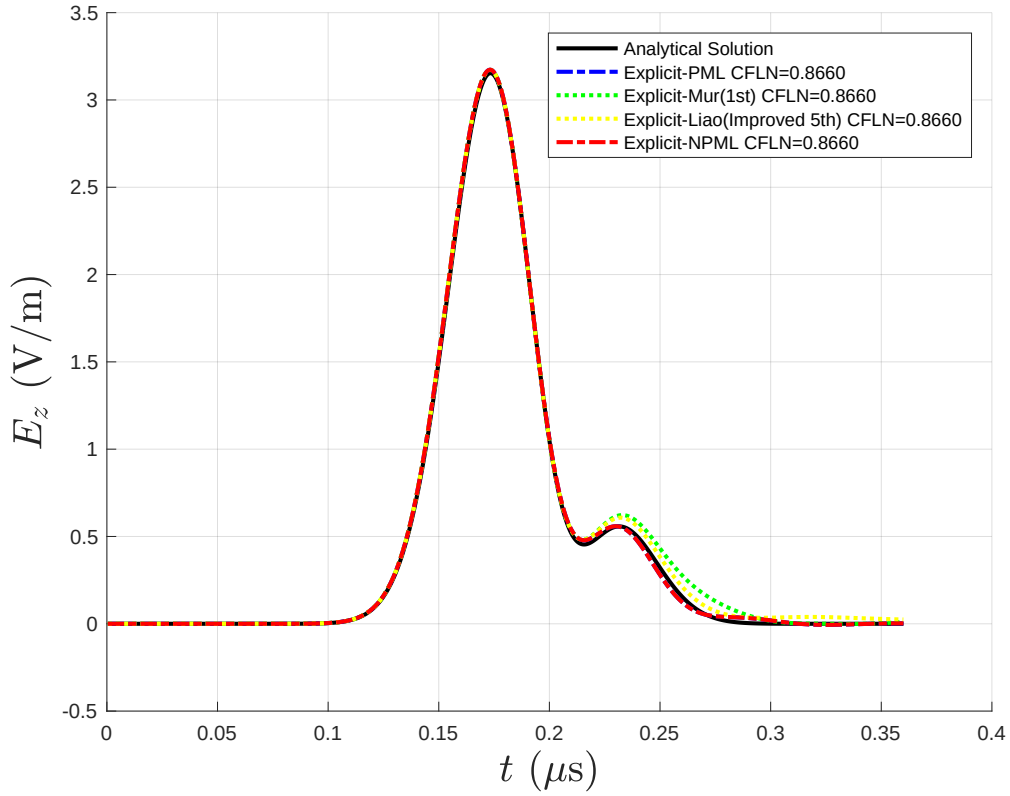


Figure 4.3. The recorded $E_z$ at the observation point based on different ABC's.

# CHAPTER 5

# THE TOTAL FIELD SCATTERED FIELD SCHEME

## 5.1 Total Field/Scattered Field Boundary

The total field/scattered field (TF/SF) technique Umashankar and Taflove (1982) was proposed in order to solve the electromagnetic problem involving excitation by a plane wave source. The domain of computation is divided into two regions, the total field region and the scattered field region. In addition, all scalar field components are represented by the sum of the incident field and the scattered field; for example, $E_{x,tot} = E_{x,inc} + E_{x,scat}$. The total field components are defined in the total field region; the scattered field components are defined in both regions; the incident field components are considered on the interface between the two regions.

### 5.1.1 The 1D Scheme

Figure 5.1 shows this model of the 1D example excited by a plane wave source. The source function is a $z$-directed Gaussian pulse that propagates along the $x$ axis. The 1D computational domain is free space on the left and right hand sides. A dielectric with $\epsilon = 3\epsilon_0$ and $\mu = \mu_0$ is placed in the middle, where $\epsilon_0$ and $\mu_0$ denote as usual the permittivity and permeability of free space. The incident wave is defined on the TF/SF boundary and propagates towards the $+x$ direction. The analytical ABC walls are placed at both ends of the domain. In the 1D cavity the incident waves are perpendicular to the boundaries, and the analytical ABC walls therefore perform perfectly and there are no reflected waves.

In Figure 5.2 the 1D model is discretized based on the Yee lattice. The TF/SF boundary is placed between Cell $I$ and Cell $I + 1$. To update the fields near the TF/SF

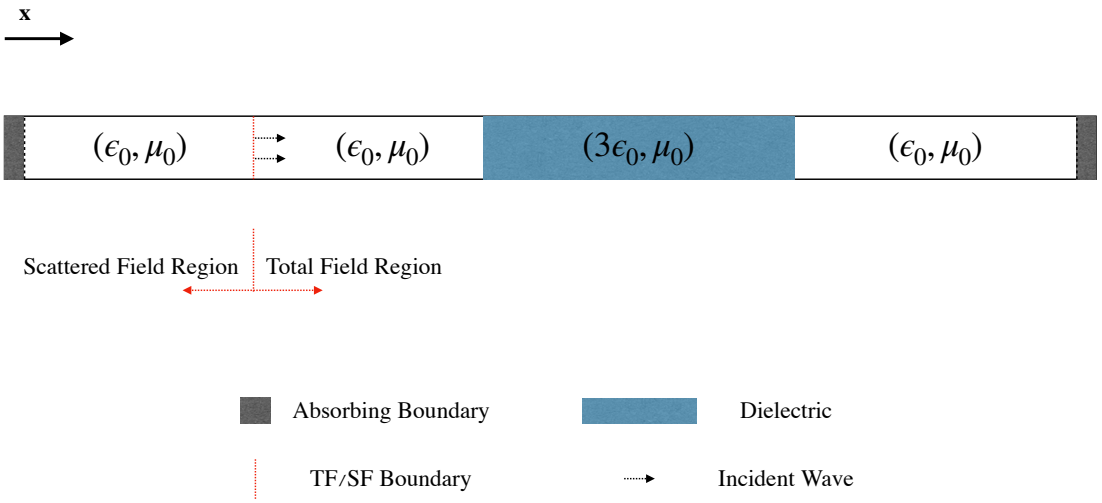


Figure 5.1. Model of the 1D TF/SF example.

boundary, the field correction method is to be applied in the FDTD algorithm, as follows. The explicit equation for updating $E_z|^{n+1}$ in Cell $I$ is

$$E_z|_{I+1}^{n+1} = E_z|_{I+1}^{n} + \frac{\Delta t}{\epsilon|_{I+1}\Delta x}(H_y|_{I+1}^{n+\frac{1}{2}} - H_y|_{I}^{n+\frac{1}{2}}). \tag{5.1}$$

In (5.2) with the TF/SF scheme, the fields are all labeled according to region, so as to indicate that the field is in the total field region or the scattered field region.

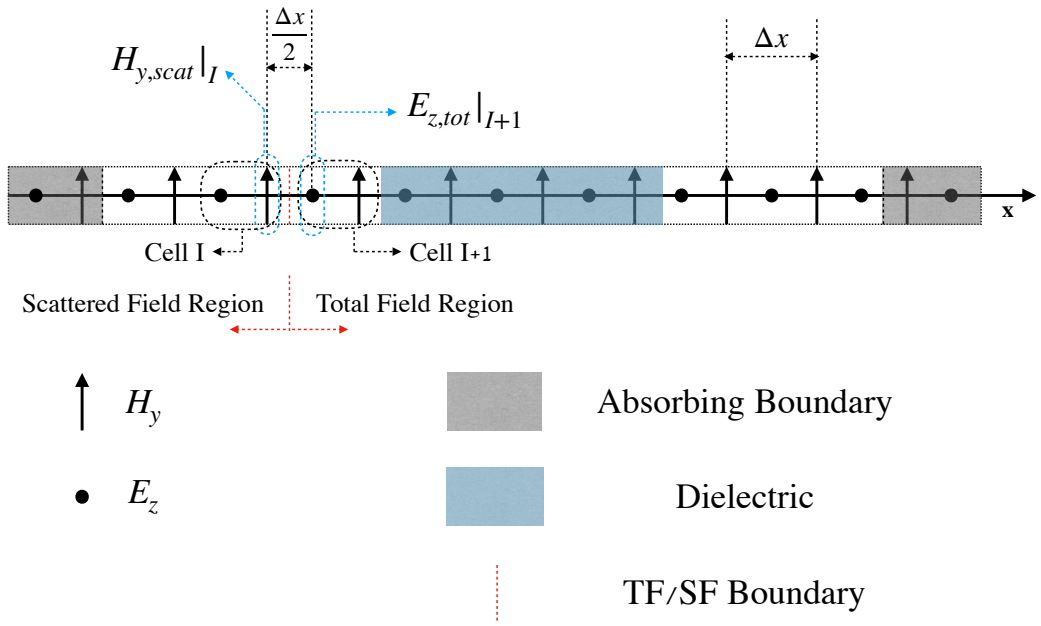


Figure 5.2. The grid of the 1D TF/SF example.

$$E_{z,tot}|_{I+1}^{n+1} = E_{z,tot}|_{I+1}^{n} + \frac{\Delta t}{\epsilon|_{I+1}\Delta x}(H_{y,tot}|_{I+1}^{n+\frac{1}{2}} - H_{y,scat}|_{I}^{n+\frac{1}{2}}), \tag{5.2}$$

The labels in (5.2) are not matched, because $H_{y,scat}|_I^{n+\frac{1}{2}}$ relates to the scattered field region whereas $E_{z,tot}|_{I+1}^{n+1}$, $E_{z,tot}|_{I+1}^{n}$ and $H_{y,tot}|_{I+1}^{n+\frac{1}{2}}$ relate to the total field region. To apply the field correction method, the field in the scattered field region is represented by

$$H_{y,scat}|_I^{n+\frac{1}{2}} = H_{y,tot}|_I^{n+\frac{1}{2}} - H_{y,inc}|_I^{n+\frac{1}{2}}. \tag{5.3}$$

Substitution of (5.3) into (5.2) yields

$$E_{z,tot}|_{I+1}^{n+1} = E_{z,tot}|_{I+1}^{n} + \frac{\Delta t}{\epsilon|_{I+1}\Delta x}[H_{y,tot}|_{I+1}^{n+\frac{1}{2}} - (H_{y,tot}|_{I}^{n+\frac{1}{2}} - H_{y,inc}|_{I}^{n+\frac{1}{2}})]. \tag{5.4}$$

In (5.4), the incident field $H_{y,inc}|_{I}^{n+\frac{1}{2}}$ represents the excitation source, and the labels of all other fields are matched. Finally, (5.4) can be rewritten in the classical FDTD way as

$$E_{z}|_{I+1}^{n+1} = E_{z}|_{I+1}^{n} + \frac{\Delta t}{\epsilon|_{I+1}\Delta x}[H_{y}|_{I+1}^{n+\frac{1}{2}} - (H_{y}|_{I}^{n+\frac{1}{2}} - H_{y,inc}|_{I}^{n+\frac{1}{2}})]. \tag{5.5}$$

Similarly, the equation for the magnetic field in Cell $I$ becomes

$$H_{y}|_{I}^{n+\frac{1}{2}} = H_{y}|_{I}^{n-\frac{1}{2}} + \frac{\Delta t}{\mu\Delta x}(E_{z}|_{I+1}^{n} - E_{z}|_{I}^{n}), \tag{5.6}$$

$$H_{y,scat}|_{I}^{n+\frac{1}{2}} = H_{y,scat}|_{I}^{n-\frac{1}{2}} + \frac{\Delta t}{\mu\Delta x}(E_{z,tot}|_{I+1}^{n} - E_{z,scat}|_{I}^{n}), \tag{5.7}$$

$$H_{y,scat}|_{I}^{n+\frac{1}{2}} = H_{y,scat}|_{I}^{n-\frac{1}{2}} + \frac{\Delta t}{\mu\Delta x}[(E_{z,scat}|_{I+1}^{n} + E_{z,inc}|_{I+1}^{n}) - E_{z,scat}|_{I}^{n}], \tag{5.8}$$

$$H_{y}|_{I}^{n+\frac{1}{2}} = H_{y}|_{I}^{n-\frac{1}{2}} + \frac{\Delta t}{\mu\Delta x}[(E_{z}|_{I+1}^{n} + E_{z,inc}|_{I+1}^{n}) - E_{z}|_{I}^{n}]. \tag{5.9}$$

For cells that are not near the TF/SF boundary, all fields in each equation are in the same region, so that no field correction is needed. The incident Gaussian fields in the following 1D example are given by

$$E_{z,inc}|_{I+1}^{n} = \exp\left[-\frac{\left(n\Delta t - t_0 - \frac{I\Delta x}{c_0}\right)^2}{\sigma^2}\right], \tag{5.10}$$

$$H_{y,inc}|_I^{n+\frac{1}{2}} = -\frac{1}{\eta_0}\exp\left\{-\frac{\left[\left(n+\frac{1}{2}\right)\Delta t - t_0 - \frac{\left(I-\frac{1}{2}\right)\Delta x}{c_0}\right]^2}{\sigma^2}\right\}. \tag{5.11}$$

where $t_0 = 180.06$ $n$s, $\sigma = 31.831$ $n$s, $\Delta x = 0.2498$ m, $\Delta t = 0.8333$ $n$s, $\eta_0$ is the characteristic impedance of free space and $c_0$ is the speed of light. In (5.10), the incident electric field in Cell $I+1$ at the interface is defined as a Gaussian wave with a spatial delay $\frac{I\Delta x}{c_0}$ and a time delay $t_0$. In Figure 5.2, the distance between $H_y$ in Cell $I$ and $E_z$ in Cell $I+1$ is $\frac{\Delta x}{2}$, and the spatial delay for $H_{y,inc}|_I^{n+\frac{1}{2}}$ in (5.11) is $\frac{(I-\frac{1}{2})\Delta x}{c_0}$. Snapshots of the electric field in the one-dimensional domain are plotted in Figure 5.3. The size of the cavity is $841 \times 1$ and $I = 221$. The dielectric is located from Cell 423 to Cell 633, and all other cells are free space. At $t = 0.5t_0$ the magnitude of the incident electric field remains negligible due to the delay of the Gaussian function. The electric field components along the whole one-dimensional axis are therefore almost zero. At $t = 2t_0$ the incident wave first becomes apparent at the interface and travels to the right hand side. At $t = 3.2t_0$ the incident wave impinges on the dielectric, and is thereafter decomposed into a transmitted wave traveling to the right and a reflected wave traveling to the left. At $t = 4t_0$ the transmitted wave and the reflected wave travel away from each other. Finally, at $t = 4.9t_0$, the incident wave hits the right edge of the dielectric, giving rise to a second transmitted wave and reflected wave.

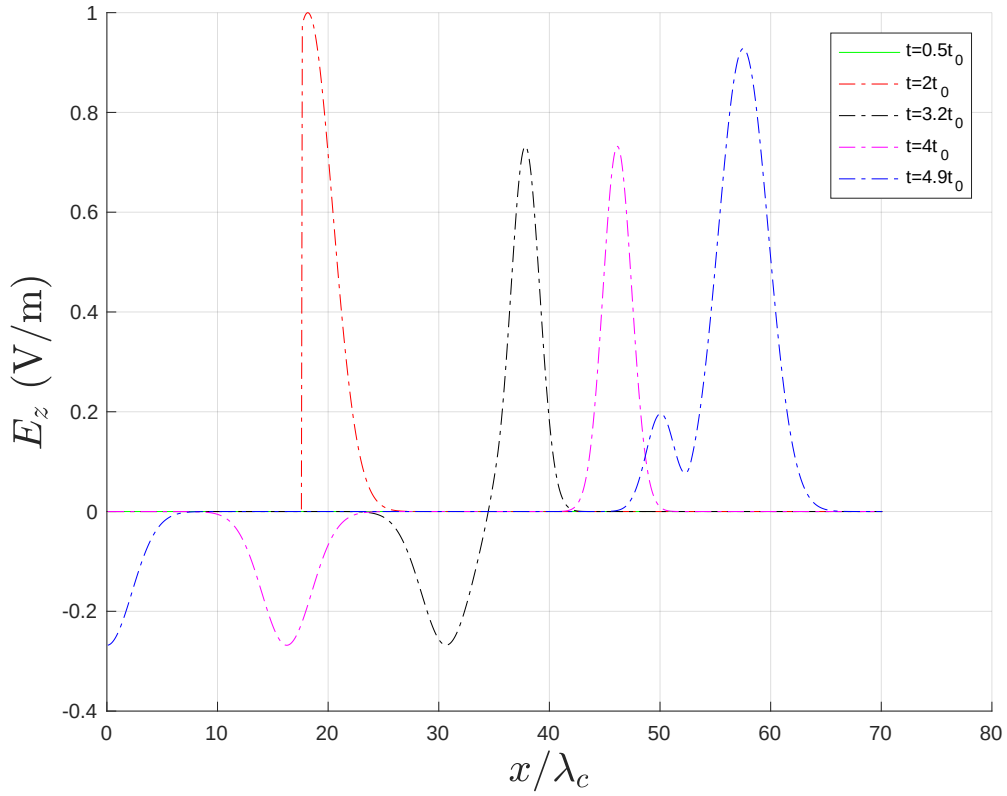


Figure 5.3. The distribution of $E_z$ in the 1D domain at different times.

### 5.1.2 The 2D Scheme

A 2D $TM_Z$ example of the TF/SF boundary is shown in Figure 5.4. The cavity is free space, and a PEC plate is placed across the center as a reflector. The NPML is applied around the entire computational domain in order to absorb the reflected waves. The total field region and the scattered field region are set up as in the one-dimensional case Schneider (2010). The incident wave is positioned along the left TF/SF boundary and the PEC plate is within the total field region.

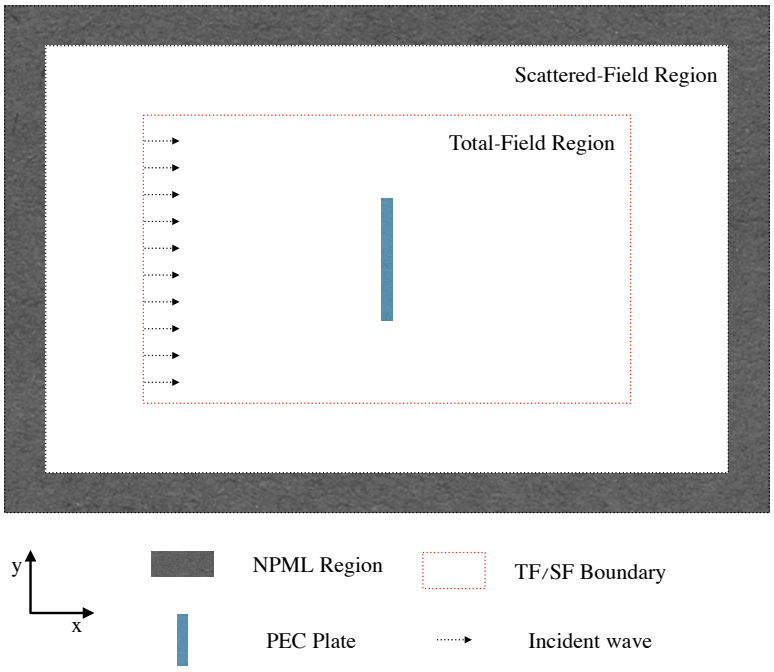


Figure 5.4. Two-dimensional TF/SF example.

Figure 5.5 shows the grid for the 2D cavity. The incident waves are obtained from the auxiliary 1D FDTD simulation. The equations for the 1D auxiliary grid are

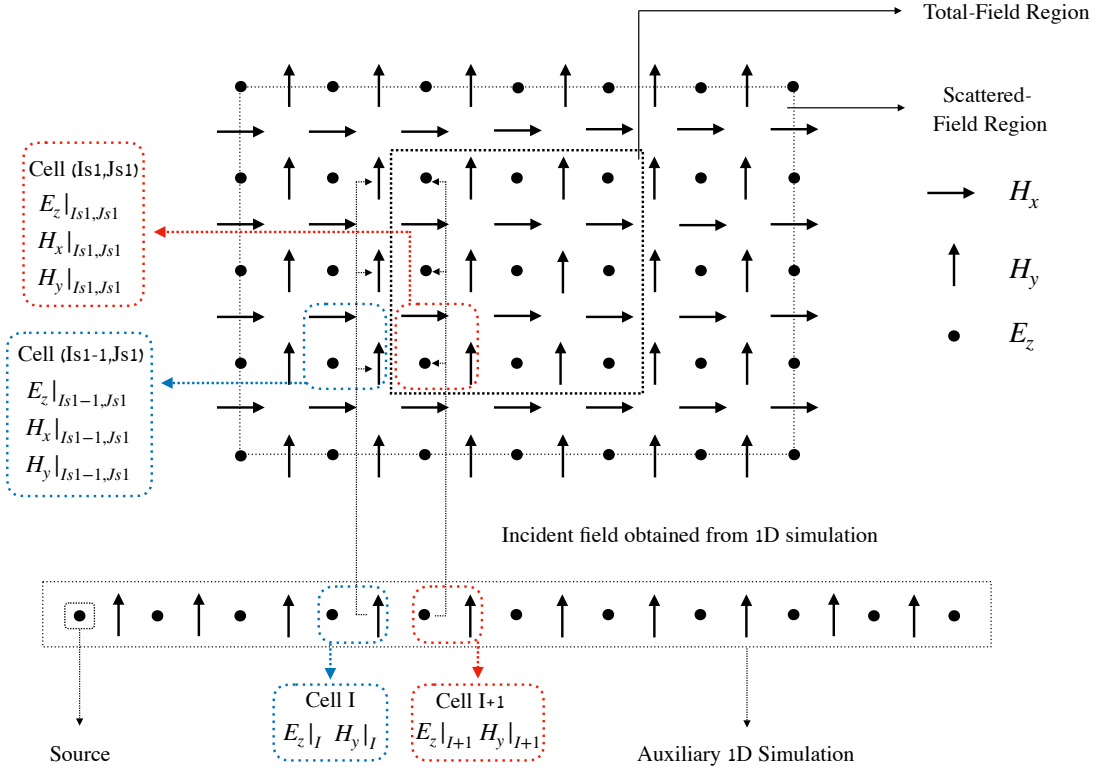


Figure 5.5. The grid of the 2D TF/SF scheme.

$$H_{y,1D}|_i^{n+\frac{1}{2}} = H_{y,1D}|_i^n + \frac{\Delta t}{\Delta x \mu}(E_{z,1D}|_{i+1}^n - E_{z,1D}|_i^n), \tag{5.12}$$

$$E_{z,1D}|_i^{n+1} = E_{z,1D}|_i^n + \frac{\Delta t}{\Delta x \epsilon}(H_{y,1D}|_i^{n+\frac{1}{2}} - H_{y,1D}|_{i-1}^{n+\frac{1}{2}}) - \frac{\Delta t}{\epsilon} J_{z,1D}|_i^{n+\frac{1}{2}}, \tag{5.13}$$

where the source of the 1D simulation is

$$J_{z,1D}|_I^{n+\frac{1}{2}} = -\frac{2}{\eta \Delta x} \exp\left\{-\frac{\left[\left(n+\frac{1}{2}\right)\Delta t - t_0\right]^2}{2\sigma_0^2}\right\}. \tag{5.14}$$

The equations of the classical 2D FDTD are

$$H_x|_{i,j}^{n+\frac{1}{2}} = H_x|_{i,j}^{n} - \frac{\Delta t}{\Delta y \mu}(E_z|_{i,j+1}^{n} - E_z|_{i,j}^{n}), \tag{5.15}$$

$$H_y|_{i,j}^{n+\frac{1}{2}} = H_y|_{i,j}^{n} + \frac{\Delta t}{\Delta x \mu}(E_z|_{i+1,j}^{n} - E_z|_{i,j}^{n}), \tag{5.16}$$

$$\begin{aligned} E_z|_{i,j}^{n+1} = E_z|_{i,j}^{n} &- \frac{\Delta t}{\Delta y \epsilon|_{i,j}}(H_x|_{i,j}^{n+\frac{1}{2}} - H_x|_{i,j-1}^{n+\frac{1}{2}}) \\ &- \frac{\Delta t}{\Delta x \epsilon|_{i,j}}(H_y|_{i,j}^{n+\frac{1}{2}} - H_y|_{i-1,j}^{n+\frac{1}{2}}). \end{aligned} \tag{5.17}$$

The fields at the TF/SF boundary must be corrected by the incident fields. For example, after labeling the fields, $H_x$ in Cell $(Is1, Js1-1)$, $H_y$ in Cell $(Is1-1, Js1)$, and $E_z$ in Cell $(Is1, Js1)$, are represented as

$$H_{x,scat}|_{Is1,Js1-1}^{n+\frac{1}{2}} = H_{x,scat}|_{Is1,Js1-1}^{n} - \frac{\Delta t}{\Delta y \mu}(E_{z,tot}|_{Is1,Js1}^{n} - E_{z,scat}|_{Is1,Js1-1}^{n}), \tag{5.18}$$

$$H_{y,scat}|_{Is1-1,Js1}^{n+\frac{1}{2}} = H_{y,scat}|_{Is1-1,Js1}^{n} + \frac{\Delta t}{\Delta x \mu}(E_{z,tot}|_{Is1,Js1}^{n} - E_{z,scat}|_{Is1-1,Js1}^{n}), \tag{5.19}$$

$$\begin{aligned} E_{z,tot}|_{Is1,Js1}^{n+1} = E_{z,tot}|_{Is1,Js1}^{n} &- \frac{\Delta t}{\Delta y \epsilon|_{Is1,Js1}}(H_{x,tot}|_{Is1,Js1}^{n+\frac{1}{2}} - H_{x,scat}|_{Is1,Js1-1}^{n+\frac{1}{2}}) \\ &- \frac{\Delta t}{\Delta x \epsilon|_{Is1,Js1}}(H_{y,tot}|_{Is1,Js1}^{n+\frac{1}{2}} - H_{y,scat}|_{Is1-1,Js1}^{n+\frac{1}{2}}). \end{aligned} \tag{5.20}$$

With the incident fields on the TF/SF boundary, (5.18), (5.19) and (5.20) are rewritten as

$$H_{x,scat}|^{n+\frac{1}{2}}_{Is1,Js1-1} = H_{x,scat}|^{n}_{Is1,Js1-1} - \frac{\Delta t}{\Delta y \mu}[(E_{z,scat}|^{n}_{Is1,Js1} + E_{z,inc}|^{n}_{Is1,Js1}) - E_{z,scat}|^{n}_{Is1,Js1-1}], \tag{5.21}$$

$$H_{y,scat}|^{n+\frac{1}{2}}_{Is1-1,Js1} = H_{y,scat}|^{n}_{Is1-1,Js1} + \frac{\Delta t}{\Delta x \mu}[(E_{z,scat}|^{n}_{Is1,Js1} + E_{z,inc}|^{n}_{Is1,Js1}) - E_{z,scat}|^{n}_{Is1-1,Js1}], \tag{5.22}$$

$$\begin{aligned} E_{z,tot}|^{n+1}_{Is1,Js1} = E_{z,tot}|^{n}_{Is1,Js1} &- \frac{\Delta t}{\Delta y \epsilon|_{Is1,Js1}}[H_{x,tot}|^{n+\frac{1}{2}}_{Is1,Js1} - (H_{x,tot}|^{n+\frac{1}{2}}_{Is1,Js1-1} - H_{x,inc}|^{n+\frac{1}{2}}_{Is1,Js1-1})] \\ &- \frac{\Delta t}{\Delta x \epsilon|_{Is1,Js1}}[H_{y,tot}|^{n+\frac{1}{2}}_{Is1,Js1} - (H_{y,tot}|^{n+\frac{1}{2}}_{Is1-1,Js1} + H_{y,inc}|^{n+\frac{1}{2}}_{Is1-1,Js1})]. \end{aligned} \tag{5.23}$$

In the 2D TF/SF scheme, the incident fields are obtained from Cell $I$ and Cell $I+1$ in the 1D FDTD simulation. Figure 5.5 shows that only $E_z$ and $H_y$ exist in the 1D grid, so that the incident fields can be written as

$$E_{z,inc}|^{n}_{Is1,Js1} = E_{z,1D}|^{n}_{I+1}, \tag{5.24}$$

$$H_{x,inc}|^{n+\frac{1}{2}}_{Is1-1,Js1} = 0, \tag{5.25}$$

$$H_{y,inc}|^{n+\frac{1}{2}}_{Is1-1,Js1} = H_{y,1D}|^{n+\frac{1}{2}}_{I}. \tag{5.26}$$

In the 2D example, $\Delta x = \Delta y = 0.2498$ m is the spatial step, $\Delta t = 0.58926$ $n$s is the time step, $f_0 = 100$ $M$Hz is the center frequency, $\lambda_0 = 0.29979$ m is the wavelength at the center frequency, and $\sigma_0 = 4.502$ $n$s controls the width of the Gaussian function while

$t_0 = 36.013$ $n$s is the delay of the Gaussian peak. In Figure 5.6, the upper sub-figure shows the Gaussian source $J_z$ in the 1D simulation; the lower sub-figure shows the electric field in Cell $I + 1$, which serves as the source of the incident wave in the 2D simulation.

Snapshots of the distribution of $E_z$ in the 2D cavity at four time instants are shown in Figure 5.7. At $t = 0.5t_0$ the incident wave fisrt becomes apparent on the left TF/SF boundary. At $t = 1.2t_0$ the incident wave is obvious and propagates along the $x$ axis. At $t = 1.5t_0$ it impinges on the PEC plate. At $t = 2.0t_0$ the PEC plate is illuminated by the incident wave, and the resulting induced surface current starts to radiate. Scattered waves are generated and begin to propagate omnidirectionally.

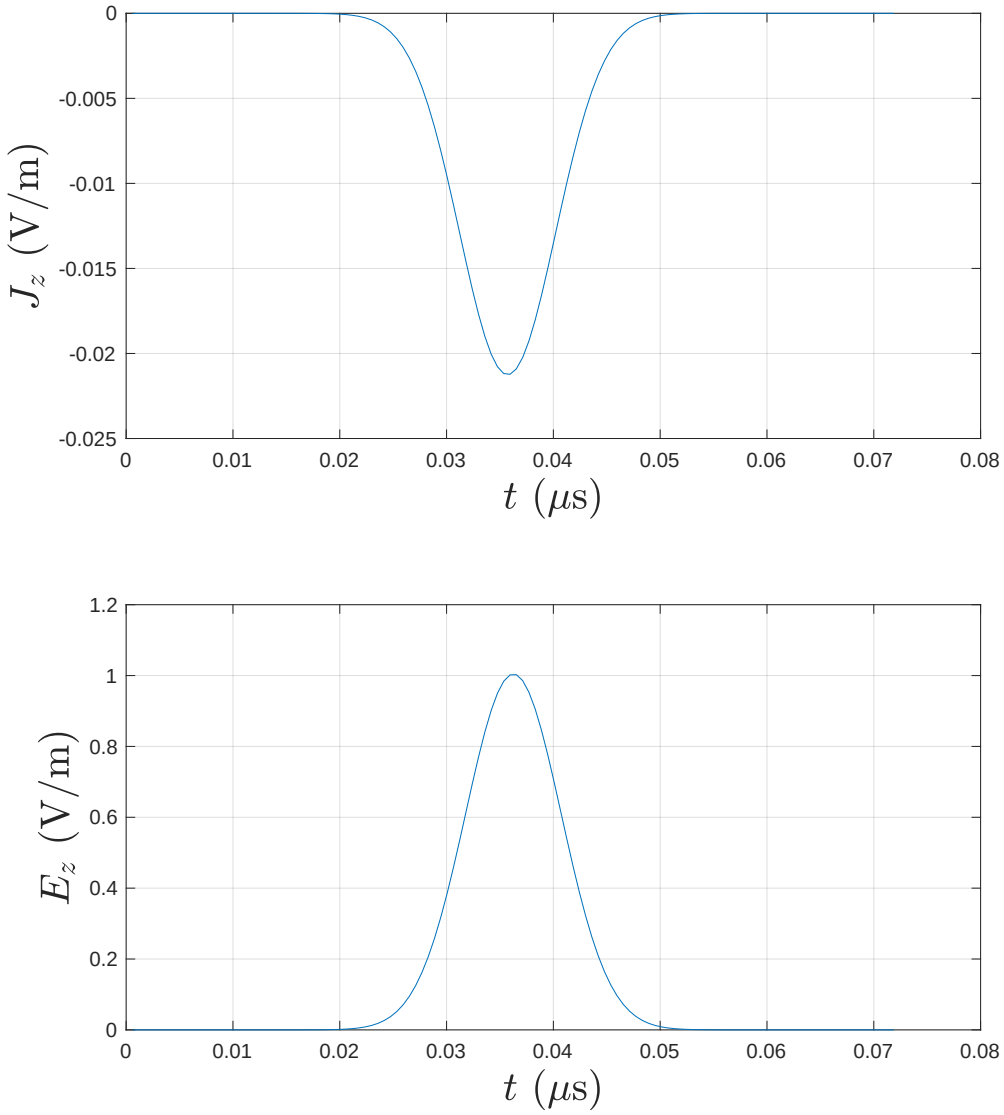


Figure 5.6. The source function for the 1D auxiliary FDTD grid and the resultant $E_{z,1D}$ in Cell $I + 1$.

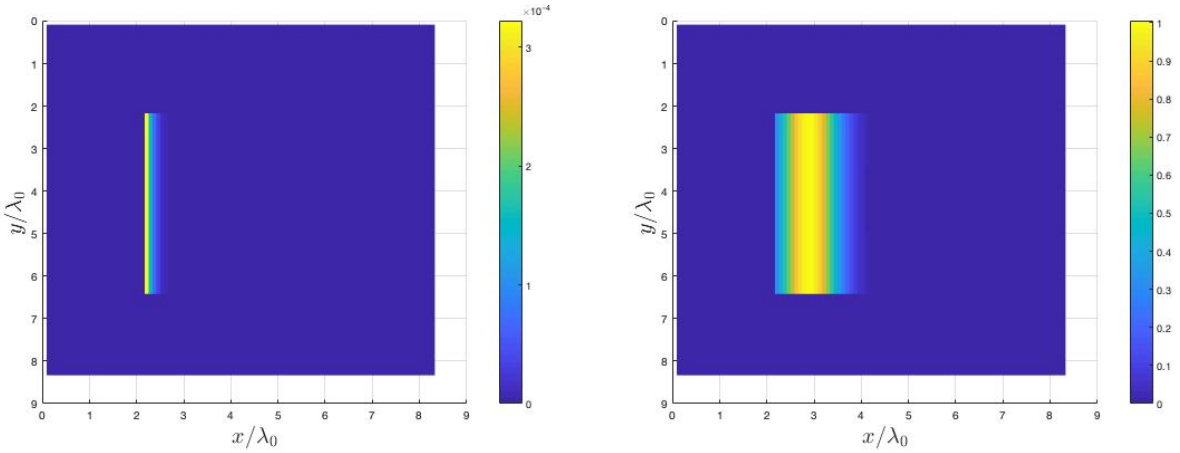


(a) $t = 0.5t_0$




(b) $t = 1.2t_0$

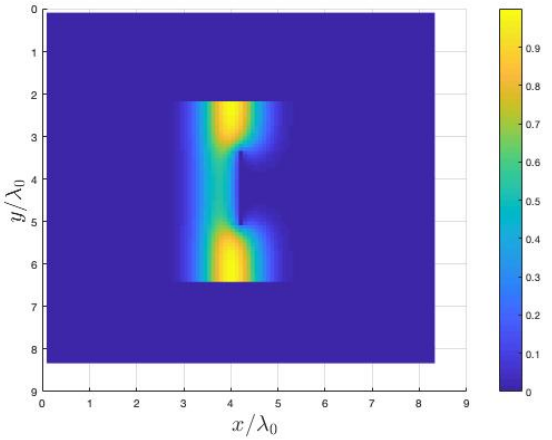


(c) $t = 1.5t_0$

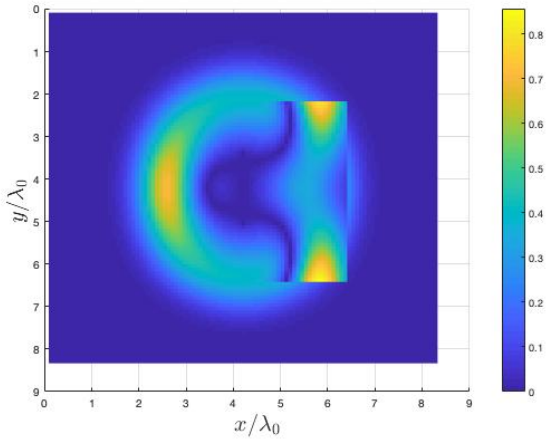


(d) $t = 2.0t_0$

Figure 5.7. The results of the two-dimensional TF/SF example

# CHAPTER 6

# THE DEVELOPED METHOD

A 2D $TM_z$ CE-4S-ADI-FDTD was introduced in Ramadan (2009). By splitting of the exponential operator, the CE-4S-ADI-FDTD is formulated as a four sub-step computational procedure. The CE-4S-ADI-FDTD solution is demonstrably much more accurate than the CE-ADI-FDTD with the same CFLN, but it requires twice the computation time because of the two additional sub-steps in each time step. In the implicit FDTD methods, the choice of a large CFLN reduces the total number of time steps and facilitates rapid solution at the cost of some accuracy. Thus, with an appropriately large CFLN, the CE-4S-ADI-FDTD solution is faster and more accurate than the corresponding CE-ADI-FDTD. In Tan (2008), fundamental schemes were developed for the implicit FDTD methods such that the number of operations in the implicit equations was greatly reduced, and the speed of computation can consequently be increased. In the present dissertation, by incorporating the fundamental scheme and the 4S scheme into the CE-ADI-FDTD algorithm in the 3D space, the 3D CE-4S-FADI-FDTD algorithm is set up. This proposed method is faster and more accurate than conventional CE-ADI-FDTD. The NPML scheme is used for modeling the absorbing boundary conditions, and the TF/SF scheme is used to model the plane wave excitation.

## 6.1 CE Implicit Class Problem

Implicit FDTD methods are developed for reducing the computation time by choosing a large CFLN value. In problems that require only a low spatial sampling rate, the allowable time step nevertheless remains small because of the accuracy limit according to the sampling theorem. That is, the maximum CFLN necessary to maintain the accuracy of these Implicit methods requires a large number of time steps. At each time step, the implicit equation

requires more computational time than the explicit equation. With a small CFLN, the implicit method is therefore slower than the explicit FDTD method.

The implicit FDTD method is more effective computationally than the explicit method in problems of small size. In large-size problems, a large number of cells is needed, implying a large number of implicit equations. Implicit equations require more computation time than explicit equations, and a large CFLN is therefore needed which degrades the accuracy of the implicit solution. Thus, in small-size problems, the implicit solution can be faster than the explicit solution while maintaining accuracy with a reasonable choice of CFLN.

Use of the CE representation shifts the center frequency of the BPL source and fields to zero. This procedure reduces the maximum frequency and accordingly increases the allowable time step, based on the sampling theorem. Ma and Chen (2005) demonstrates that the benefits of using the CE representation decrease as the ratio of the center frequency to the bandwidth decreases. With a small ratio then, after shifting the center frequency to zero, the maximum frequency is equal to half of the bandwidth, which is still high. The small allowable time step then leads to a small CFLN and a slow implicit solution.

In conclusion, CE implicit methods are developed for solving small-size problems, involving high spatial sampling rate and a narrowband excitation source.

## 6.2 3D CE-4S-FADI-FDTD with PEC Boundaries

Begin with the CE Maxwell's equations, $\frac{\partial}{\partial t}\tilde{u} + j\omega_0\tilde{u} = M\tilde{u}$, where the matrix $M$ consists of the spatial differential operators, and

$$\tilde{u} = [\tilde{E}_x\ \tilde{E}_y\ \tilde{E}_z\ \tilde{H}_x\ \tilde{H}_y\ \tilde{H}_z]^T. \tag{6.1}$$

Next, $M_1$ and $j\omega_0$ are combined and decomposed into two sub-matrices, $A_1$ and $B_1$ as follows:

$$M_1 = \begin{bmatrix} 0 & 0 & 0 & 0 & -\frac{1}{\mu}\frac{\partial}{\partial z} & \frac{1}{\mu}\frac{\partial}{\partial y} \\ 0 & 0 & 0 & \frac{1}{\mu}\frac{\partial}{\partial z} & 0 & -\frac{1}{\mu}\frac{\partial}{\partial x} \\ 0 & 0 & 0 & -\frac{1}{\mu}\frac{\partial}{\partial y} & \frac{1}{\mu}\frac{\partial}{\partial x} & 0 \\ 0 & \frac{1}{\epsilon}\frac{\partial}{\partial z} & -\frac{1}{\epsilon}\frac{\partial}{\partial y} & 0 & 0 & 0 \\ -\frac{1}{\epsilon}\frac{\partial}{\partial z} & 0 & \frac{1}{\epsilon}\frac{\partial}{\partial x} & 0 & 0 & 0 \\ \frac{1}{\epsilon}\frac{\partial}{\partial y} & -\frac{1}{\epsilon}\frac{\partial}{\partial x} & 0 & 0 & 0 & 0 \end{bmatrix}$$

$$A_1 = \begin{bmatrix} -\frac{j\omega_0}{2} & 0 & 0 & 0 & 0 & \frac{1}{\mu}\frac{\partial}{\partial y} \\ 0 & -\frac{j\omega_0}{2} & 0 & \frac{1}{\mu}\frac{\partial}{\partial z} & 0 & 0 \\ 0 & 0 & -\frac{j\omega_0}{2} & 0 & \frac{1}{\mu}\frac{\partial}{\partial x} & 0 \\ 0 & \frac{1}{\epsilon}\frac{\partial}{\partial z} & 0 & -\frac{j\omega_0}{2} & 0 & 0 \\ 0 & 0 & \frac{1}{\epsilon}\frac{\partial}{\partial x} & 0 & -\frac{j\omega_0}{2} & 0 \\ \frac{1}{\epsilon}\frac{\partial}{\partial y} & 0 & 0 & 0 & 0 & -\frac{j\omega_0}{2} \end{bmatrix}$$

$$B_1 = \begin{bmatrix} -\frac{j\omega_0}{2} & 0 & 0 & 0 & -\frac{1}{\mu}\frac{\partial}{\partial z} & 0 \\ 0 & -\frac{j\omega_0}{2} & 0 & 0 & 0 & -\frac{1}{\mu}\frac{\partial}{\partial x} \\ 0 & 0 & -\frac{j\omega_0}{2} & -\frac{1}{\mu}\frac{\partial}{\partial y} & 0 & 0 \\ 0 & 0 & -\frac{1}{\epsilon}\frac{\partial}{\partial y} & -\frac{j\omega_0}{2} & 0 & 0 \\ -\frac{1}{\epsilon}\frac{\partial}{\partial z} & 0 & 0 & 0 & -\frac{j\omega_0}{2} & 0 \\ 0 & -\frac{1}{\epsilon}\frac{\partial}{\partial x} & 0 & 0 & 0 & -\frac{j\omega_0}{2} \end{bmatrix}$$

Upon defining the auxiliary vector $\tilde{v}$, the computational procedure for the 3D CE-4S-FADI-FDTD algorithm is as follows:

sub-step 1

$$\tilde{v}|^n = 2\tilde{u}|^n - \tilde{v}|^{n-\frac{1}{4}} + \frac{\Delta t}{4}\tilde{s}|^{n+\frac{1}{8}}, \tag{6.2}$$

$$\left(I - \frac{\Delta t}{4}A_1\right)\tilde{u}|^{n+\frac{1}{4}} = \tilde{v}|^n, \tag{6.3}$$

sub-step 2

$$\tilde{v}|^{n+\frac{1}{4}} = 2\tilde{u}|^{n+\frac{1}{4}} - \tilde{v}|^{n} + \frac{\Delta t}{4}\tilde{s}|^{n+\frac{3}{8}}, \tag{6.4}$$

$$\left(I - \frac{\Delta t}{4}B_1\right)\tilde{u}|^{n+\frac{1}{2}} = \tilde{v}|^{n+\frac{1}{4}}, \tag{6.5}$$

sub-step 3

$$\tilde{v}|^{n+\frac{1}{2}} = 2\tilde{u}|^{n+\frac{1}{2}} - \tilde{v}|^{n+\frac{1}{4}} + \frac{\Delta t}{4}\tilde{s}|^{n+\frac{5}{8}}, \tag{6.6}$$

$$\left(I - \frac{\Delta t}{4}A_1\right)\tilde{u}|^{n+\frac{3}{4}} = \tilde{v}|^{n+\frac{1}{2}}, \tag{6.7}$$

sub-step 4

$$\tilde{v}|^{n+\frac{3}{4}} = 2\tilde{u}|^{n+\frac{3}{4}} - \tilde{v}|^{n+\frac{1}{2}} + \frac{\Delta t}{4}\tilde{s}|^{n+\frac{7}{8}}, \tag{6.8}$$

$$\left(I - \frac{\Delta t}{4}B_1\right)\tilde{u}|^{n+1} = \tilde{v}|^{n+\frac{3}{4}}, \tag{6.9}$$

where

$$\tilde{v} = [\tilde{e}_x\ \tilde{e}_y\ \tilde{e}_z\ \tilde{h}_x\ \tilde{h}_y\ \tilde{h}_z]^T, \tag{6.10}$$

$$\tilde{s} = \left[-\frac{1}{\epsilon}\tilde{J}_x\ -\frac{1}{\epsilon}\tilde{J}_y\ -\frac{1}{\epsilon}\tilde{J}_z\ -\frac{1}{\mu}\tilde{M}_x\ -\frac{1}{\mu}\tilde{M}_y\ -\frac{1}{\mu}\tilde{M}_z\right]^T \tag{6.11}$$

and $I$ is the identity matrix. At each time step, three intermediate field components are needed, at $t = n + 1/4$, $t = n + 2/4$ and $t = n + 3/4$, in the calculation involving four sub-steps. In each sub-step, after spatial discretization, then by substituting the equation of magnetic field components it follows that the equation for the electric field components can be solved implicitly. The magnetic field components are then updated explicitly. For example, expansion of the matrices in sub-step 1 yields the following equations:

$$\tilde{e}_x|^n_{i,j,k} = 2\tilde{E}_x|^n_{i,j,k} - \tilde{e}_x|^{n-\frac{1}{4}}_{i,j,k} - \frac{\Delta t}{4\epsilon}\tilde{J}_x|^{n+\frac{1}{8}}_{i,j,k}, \tag{6.12}$$

$$\tilde{e}_y|^n_{i,j,k} = 2\tilde{E}_y|^n_{i,j,k} - \tilde{e}_y|^{n-\frac{1}{4}}_{i,j,k} - \frac{\Delta t}{4\epsilon}\tilde{J}_y|^{n+\frac{1}{8}}_{i,j,k}, \tag{6.13}$$

$$\tilde{e}_z|^n_{i,j,k} = 2\tilde{E}_z|^n_{i,j,k} - \tilde{e}_z|^{n-\frac{1}{4}}_{i,j,k} - \frac{\Delta t}{4\epsilon}\tilde{J}_z|^{n+\frac{1}{8}}_{i,j,k}, \tag{6.14}$$

$$\tilde{h}_x|^n_{i,j,k} = 2\tilde{H}_x|^n_{i,j,k} - \tilde{h}_x|^{n-\frac{1}{4}}_{i,j,k} - \frac{\Delta t}{4\mu}\tilde{M}_x|^{n+\frac{1}{8}}_{i,j,k}, \tag{6.15}$$

$$\tilde{h}_y|^n_{i,j,k} = 2\tilde{H}_y|^n_{i,j,k} - \tilde{h}_y|^{n-\frac{1}{4}}_{i,j,k} - \frac{\Delta t}{4\mu}\tilde{M}_y|^{n+\frac{1}{8}}_{i,j,k}, \tag{6.16}$$

$$\tilde{h}_z|^n_{i,j,k} = 2\tilde{H}_z|^n_{i,j,k} - \tilde{h}_z|^{n-\frac{1}{4}}_{i,j,k} - \frac{\Delta t}{4\mu}\tilde{M}_z|^{n+\frac{1}{8}}_{i,j,k}, \tag{6.17}$$

$$\frac{8 + j\omega_0\Delta t}{8}\tilde{E}_x|^{n+\frac{1}{4}}_{i,j,k} - \frac{\Delta t}{4\epsilon\Delta y}(\tilde{H}_z|^{n+\frac{1}{4}}_{i,j,k} - \tilde{H}_z|^{n+\frac{1}{4}}_{i,j-1,k}) = \tilde{e}_x|^n_{i,j,k}, \tag{6.18}$$

$$\frac{8 + j\omega_0\Delta t}{8}\tilde{E}_y|^{n+\frac{1}{4}}_{i,j,k} - \frac{\Delta t}{4\epsilon\Delta z}(\tilde{H}_x|^{n+\frac{1}{4}}_{i,j,k} - \tilde{H}_x|^{n+\frac{1}{4}}_{i,j,k-1}) = \tilde{e}_y|^n_{i,j,k}, \tag{6.19}$$

$$\frac{8 + j\omega_0\Delta t}{8}\tilde{E}_z|^{n+\frac{1}{4}}_{i,j,k} - \frac{\Delta t}{4\epsilon\Delta x}(\tilde{H}_y|^{n+\frac{1}{4}}_{i,j,k} - \tilde{H}_y|^{n+\frac{1}{4}}_{i-1,j,k}) = \tilde{e}_z|^n_{i,j,k}, \tag{6.20}$$

$$\frac{8 + j\omega_0\Delta t}{8}\tilde{H}_x|^{n+\frac{1}{4}}_{i,j,k} - \frac{\Delta t}{4\mu\Delta z}(\tilde{E}_y|^{n+\frac{1}{4}}_{i,j,k+1} - \tilde{E}_y|^{n+\frac{1}{4}}_{i,j,k}) = \tilde{h}_x|^n_{i,j,k}, \tag{6.21}$$

$$\frac{8 + j\omega_0\Delta t}{8}\tilde{H}_y|^{n+\frac{1}{4}}_{i,j,k} - \frac{\Delta t}{4\mu\Delta x}(\tilde{E}_z|^{n+\frac{1}{4}}_{i+1,j,k} - \tilde{E}_z|^{n+\frac{1}{4}}_{i,j,k}) = \tilde{h}_y|^n_{i,j,k}, \tag{6.22}$$

$$\frac{8+j\omega_0\Delta t}{8}\tilde{H}_z|_{i,j,k}^{n+\frac{1}{4}} - \frac{\Delta t}{4\mu\Delta y}(\tilde{E}_x|_{i,j+1,k}^{n+\frac{1}{4}} - \tilde{E}_x|_{i,j,k}^{n+\frac{1}{4}}) = \tilde{h}_z|_{i,j,k}^{n}, \tag{6.23}$$

Equations (6.12) - (6.17) for the auxiliary variables can be solved explicitly. For simplicity, the sizes of the spatial steps are the same in all directions in the examples below: $\Delta x = \Delta y = \Delta z = \Delta$. The equations for the electric and magnetic fields are then written as:

$$\tilde{E}_x|_{i,j,k}^{n+\frac{1}{4}} = C \cdot \tilde{e}_x|_{i,j,k}^{n} + AC(\tilde{H}_z|_{i,j,k}^{n+\frac{1}{4}} - \tilde{H}_z|_{i,j-1,k}^{n+\frac{1}{4}}), \tag{6.24}$$

$$\tilde{E}_y|_{i,j,k}^{n+\frac{1}{4}} = C \cdot \tilde{e}_y|_{i,j,k}^{n} + AC(\tilde{H}_x|_{i,j,k}^{n+\frac{1}{4}} - \tilde{H}_x|_{i,j,k-1}^{n+\frac{1}{4}}), \tag{6.25}$$

$$\tilde{E}_z|_{i,j,k}^{n+\frac{1}{4}} = C \cdot \tilde{e}_z|_{i,j,k}^{n} + AC(\tilde{H}_y|_{i,j,k}^{n+\frac{1}{4}} - \tilde{H}_y|_{i-1,j,k}^{n+\frac{1}{4}}), \tag{6.26}$$

$$\tilde{H}_x|_{i,j,k}^{n+\frac{1}{4}} = C \cdot \tilde{h}_x|_{i,j,k}^{n} + BC(\tilde{E}_y|_{i,j,k+1}^{n+\frac{1}{4}} - \tilde{E}_y|_{i,j,k}^{n+\frac{1}{4}}), \tag{6.27}$$

$$\tilde{H}_y|_{i,j,k}^{n+\frac{1}{4}} = C \cdot \tilde{h}_y|_{i,j,k}^{n} + BC(\tilde{E}_z|_{i+1,j,k}^{n+\frac{1}{4}} - \tilde{E}_z|_{i,j,k}^{n+\frac{1}{4}}), \tag{6.28}$$

$$\tilde{H}_z|_{i,j,k}^{n+\frac{1}{4}} = C \cdot \tilde{h}_z|_{i,j,k}^{n} + BC(\tilde{E}_x|_{i,j+1,k}^{n+\frac{1}{4}} - \tilde{E}_x|_{i,j,k}^{n+\frac{1}{4}}), \tag{6.29}$$

where $C = \frac{8}{8+j\omega_0\Delta t}$, $A = \frac{\Delta t}{4\epsilon\Delta}$ and $B = \frac{\Delta t}{4\mu\Delta}$. Substitution of (6.29) into (6.24) yields

$$\begin{aligned}\tilde{E}_x|^{n+\frac{1}{4}} = C \cdot \tilde{e}_x|_{i,j,k}^{n} &+ AC \cdot [C \cdot \tilde{h}_z|_{i,j,k}^{n} + BC \cdot (\tilde{E}_x|_{i,j+1,k}^{n+\frac{1}{4}} - \tilde{E}_x|_{i,j,k}^{n+\frac{1}{4}})] \\ &- AC \cdot [C \cdot \tilde{h}_z|_{i,j-1,k}^{n} + BC \cdot (\tilde{E}_x|_{i,j,k}^{n+\frac{1}{4}} - \tilde{E}_x|_{i,j-1,k}^{n+\frac{1}{4}})].\end{aligned} \tag{6.30}$$

After rearranging (6.30), $\tilde{E}_x$ can be solved by

$$\tilde{E}_x|_{i,j,k}^{n+\frac{1}{4}} - ABC^2 \cdot (\tilde{E}_x|_{i,j+1,k}^{n+\frac{1}{4}} - 2\tilde{E}_x|_{i,j,k}^{n+\frac{1}{4}} + \tilde{E}_x|_{i,j-1,k}^{n+\frac{1}{4}})$$
$$= C \cdot \tilde{e}_x|_{i,j,k}^{n} + AC^2 \cdot (\tilde{h}_z|_{i,j,k}^{n} - \tilde{h}_z|_{i,j-1,k}^{n}). \tag{6.31}$$

With PEC boundary conditions, it follows that at any time instant $\tilde{E}_x|_{i,1,k} = 0$ and $\tilde{E}_x|_{i,j_{max},k} = 0$, where $j_{max}$ is the maximum index of $\tilde{E}_x$ in the $y$ direction. Consequently, (6.31) can be written in matrix form as

$$\begin{bmatrix} 1+2P & -P & 0 & 0 & \cdots & 0 \\ -P & 1+2P & -P & 0 & \cdots & 0 \\ & & & \ddots & & \\ 0 & \cdots & 0 & -P & 1+2P & -P \\ 0 & \cdots & 0 & 0 & 1+2P & -P \end{bmatrix} \begin{bmatrix} \tilde{E}_x|_{i,2,k}^{n+\frac{1}{4}} \\ \tilde{E}_x|_{i,3,k}^{n+\frac{1}{4}} \\ \vdots \\ \tilde{E}_x|_{i,j_{max}-2,k}^{n+\frac{1}{4}} \\ \tilde{E}_x|_{i,j_{max}-1,k}^{n+\frac{1}{4}} \end{bmatrix} = \begin{bmatrix} \tilde{f}_x|_{i,2,k}^{n} \\ \tilde{f}_x|_{i,3,k}^{n} \\ \vdots \\ \tilde{f}_x|_{i,j_{max}-2,k}^{n} \\ \tilde{f}_x|_{i,j_{max}-1,k}^{n} \end{bmatrix},$$

where $P = ABC^2$, $\tilde{f}_x|_{i,j,k}^{n} = C \cdot \tilde{e}_x|_{i,j,k}^{n} + AC^2 \cdot (\tilde{h}_z|_{i,j,k}^{n} - \tilde{h}_z|_{i,j-1,k}^{n})$, and the coefficient matrix of $\tilde{E}_x$ is tridiagonal. In sub-step 1, $\tilde{E}_x$ and $\tilde{H}_z$ are calculated according to the following procedure: first update the auxiliary fields $\tilde{e}_x$ and $\tilde{h}_z$ explicitly by (6.12) and (6.17); then update $\tilde{E}_x$ implicitly by (6.31); finally, update $\tilde{H}_z$ explicitly by (6.29). Next, $\tilde{E}_y$ and $\tilde{H}_x$ are updated in the same manner, and likewise $\tilde{E}_z$ and $\tilde{H}_y$. Similarly, within each time step, the electric fields, magnetic fields and auxiliary variables in other sub-steps can be updated.

There are three terms on the right hand side of the implicit equation (6.31), based on the proposed CE-4S-FADI-FDTD algorithm. In contrast, based on the CE-ADI-FDTD algorithm there are nine terms on the right hand side of the implicit equation (3.38) for calculating the same field $\tilde{E}_x$. Similar results are found in the comparison of other implicit equations based on the two methods. Consequently, in the CE-4S-FADI-FDTD algorithm, the number of terms and operations in the implicit equations is 66.67% fewer than in the

implicit equations of the CE-ADI-FDTD algorithm. As the implicit equations need to be solved multiple times at each time step, this results in a great reduction of the computational time needed in the overall simulation.

## 6.3 3D CE-4S-FADI-FDTD with NPML

To incorporate CE-4S-FADI-FDTD into the NPML algorithm, two auxiliary variables are defined for each field component, based on the the differential operators. For example, $E_{xy}$ and $E_{xz}$ are defined for $E_x$. In the frequency domain, $E_{xy} = \frac{E_x}{S_y}$, where $S_y = 1 + \frac{\sigma_y}{j\omega_0\epsilon}$, which by inverse Fourier transform can be converted to the time domain equation, $\frac{\partial}{\partial t}E_{xy} + \frac{\sigma_y}{\epsilon}E_{xy} = \frac{\partial}{\partial t}E_x$. The fictitious conductivities $\sigma_x$, $\sigma_y$ and $\sigma_z$ are defined as in the Berenger Perfectly Matched Layers method; see Elsherbeni and Demir (2009).

As an example, Figure 6.1 shows the PML conductivity $\sigma_y$ defined in the PML region. The cube in the top left corner represents the computational domain. After extending several cells along all directions, the new model is built at the bottom left corner, which includes the computational domain and the PML region. The distribution of the PML conductivities on the arbitrary 2D plane $i = i_0$ is shown at right; $\sigma_y$ is defined along the $y$ direction and $\sigma_z$ is defined along the $z$ direction. In the computational domain, $\sigma_y = 0$, and in the left PML region $\sigma_y$ is defined by the following equations:

$$\sigma_y|_{i,j,k} = \sigma_{max}\left(\frac{|j - j_-|\Delta y}{\delta}\right)^{n_{pml}}, \tag{6.32}$$

$$\sigma_{max} = -\frac{(n_{pml}+1)\,\epsilon c_0 \ln(R_0)}{2\Delta y N}, \tag{6.33}$$

where $j_0$ is the index of the left computational domain-PML interface, $|j - j_-|\Delta y$ is the distance between the conductivity cell and the interface, $n_{pml} = 2$ for the parabolic distribution, N is the number of PML cells in the left PML region, $\delta$ is the thickness of the PML region on the left, $\Delta y$ is the spatial step in the $y$ direction, and $R_0 = 10^{-5}$. Here, $\sigma_y$ in the

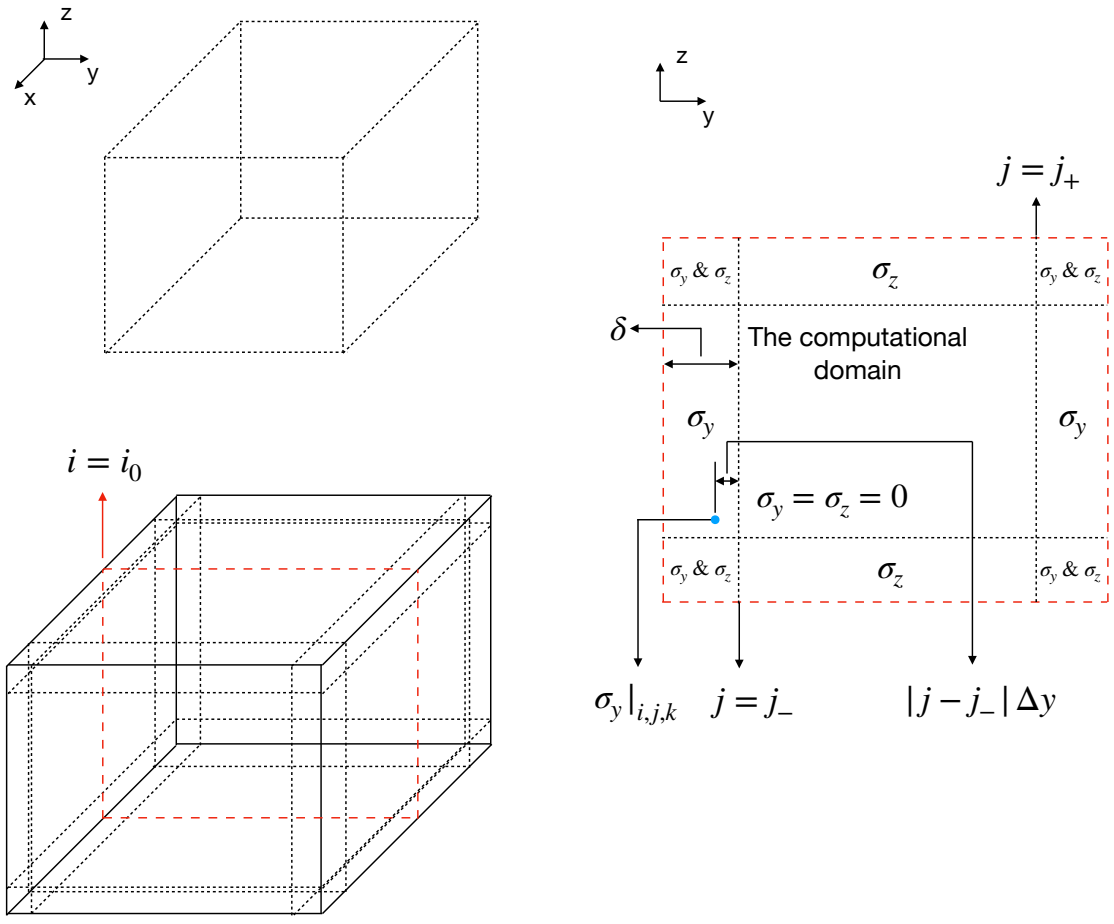


Figure 6.1. The distribution of $\sigma_y$ in the computational domain and in the PML region.

right PML region is defined according to the index of the right computational domain-PML interface $j_+$. The distribution of the PML conductivities in other regions of the new model can be found likewise. Then, using the PML conductivities $\sigma_x$, $\sigma_y$ and $\sigma_z$, the four sub-steps computation and the matrices of operators $M_2$, $A_2$ and $B_2$ for the 3D CE-4S-FADI-FDTD algorithm are as follows:

sub-step 1

$$\tilde{v}|^n = 2\tilde{u}|^n - \tilde{v}|^{n-\frac{1}{4}} + \frac{\Delta t}{4}\tilde{s}|^{n+\frac{1}{8}}, \tag{6.34}$$

$$\left(I - \frac{\Delta t}{4} A_2\right) \tilde{u}|^{n+\frac{1}{4}} = \tilde{v}|^{n}, \tag{6.35}$$

sub-step 2

$$\tilde{v}|^{n+\frac{1}{4}} = 2\tilde{u}|^{n+\frac{1}{4}} - \tilde{v}|^{n} + \frac{\Delta t}{4} \tilde{s}|^{n+\frac{3}{8}}, \tag{6.36}$$

$$\left(I - \frac{\Delta t}{4} B_2\right) \tilde{u}|^{n+\frac{1}{2}} = \tilde{v}|^{n+\frac{1}{4}}, \tag{6.37}$$

sub-step 3

$$\tilde{v}|^{n+\frac{1}{2}} = 2\tilde{u}|^{n+\frac{1}{2}} - \tilde{v}|^{n+\frac{1}{4}} + \frac{\Delta t}{4} \tilde{s}|^{n+\frac{5}{8}}, \tag{6.38}$$

$$\left(I - \frac{\Delta t}{4} A_2\right) \tilde{u}|^{n+\frac{3}{4}} = \tilde{v}|^{n+\frac{1}{2}}, \tag{6.39}$$

sub-step 4

$$\tilde{v}|^{n+\frac{3}{4}} = 2\tilde{u}|^{n+\frac{3}{4}} - \tilde{v}|^{n+\frac{1}{2}} + \frac{\Delta t}{4} \tilde{s}|^{n+\frac{7}{8}}, \tag{6.40}$$

$$\left(I - \frac{\Delta t}{4} B_2\right) \tilde{u}|^{n+1} = \tilde{v}|^{n+\frac{3}{4}}, \tag{6.41}$$

where

$$M_2 = \begin{bmatrix} 0 & 0 & 0 & 0 & -\frac{1}{\mu}\frac{\partial}{\partial z}\frac{1}{S_z} & \frac{1}{\mu}\frac{\partial}{\partial y}\frac{1}{S_y} \\ 0 & 0 & 0 & \frac{1}{\mu}\frac{\partial}{\partial z}\frac{1}{S_z} & 0 & -\frac{1}{\mu}\frac{\partial}{\partial x}\frac{1}{S_x} \\ 0 & 0 & 0 & -\frac{1}{\mu}\frac{\partial}{\partial y}\frac{1}{S_y} & \frac{1}{\mu}\frac{\partial}{\partial x}\frac{1}{S_x} & 0 \\ 0 & \frac{1}{\epsilon}\frac{\partial}{\partial z}\frac{1}{S_z} & -\frac{1}{\epsilon}\frac{\partial}{\partial y}\frac{1}{S_y} & 0 & 0 & 0 \\ -\frac{1}{\epsilon}\frac{\partial}{\partial z}\frac{1}{S_z} & 0 & \frac{1}{\epsilon}\frac{\partial}{\partial x}\frac{1}{S_x} & 0 & 0 & 0 \\ \frac{1}{\epsilon}\frac{\partial}{\partial y}\frac{1}{S_y} & -\frac{1}{\epsilon}\frac{\partial}{\partial x}\frac{1}{S_x} & 0 & 0 & 0 & 0 \end{bmatrix},$$

$$A_2 = \begin{bmatrix} -\frac{j\omega_0}{2} & 0 & 0 & 0 & 0 & \frac{1}{\mu}\frac{\partial}{\partial y}\frac{1}{S_y} \\ 0 & -\frac{j\omega_0}{2} & 0 & \frac{1}{\mu}\frac{\partial}{\partial z}\frac{1}{S_z} & 0 & 0 \\ 0 & 0 & -\frac{j\omega_0}{2} & 0 & \frac{1}{\mu}\frac{\partial}{\partial x}\frac{1}{S_x} & 0 \\ 0 & \frac{1}{\epsilon}\frac{\partial}{\partial z}\frac{1}{S_z} & 0 & -\frac{j\omega_0}{2} & 0 & 0 \\ 0 & 0 & \frac{1}{\epsilon}\frac{\partial}{\partial x}\frac{1}{S_x} & 0 & -\frac{j\omega_0}{2} & 0 \\ \frac{1}{\epsilon}\frac{\partial}{\partial y}\frac{1}{S_y} & 0 & 0 & 0 & 0 & -\frac{j\omega_0}{2} \end{bmatrix},$$

$$B_2 = \begin{bmatrix} -\frac{j\omega_0}{2} & 0 & 0 & 0 & -\frac{1}{\mu}\frac{\partial}{\partial z}\frac{1}{S_z} & 0 \\ 0 & -\frac{j\omega_0}{2} & 0 & 0 & 0 & -\frac{1}{\mu}\frac{\partial}{\partial x}\frac{1}{S_x} \\ 0 & 0 & -\frac{j\omega_0}{2} & -\frac{1}{\mu}\frac{\partial}{\partial y}\frac{1}{S_y} & 0 & 0 \\ 0 & 0 & -\frac{1}{\epsilon}\frac{\partial}{\partial y}\frac{1}{S_y} & -\frac{j\omega_0}{2} & 0 & 0 \\ -\frac{1}{\epsilon}\frac{\partial}{\partial z}\frac{1}{S_z} & 0 & 0 & 0 & -\frac{j\omega_0}{2} & 0 \\ 0 & -\frac{1}{\epsilon}\frac{\partial}{\partial x}\frac{1}{S_x} & 0 & 0 & 0 & -\frac{j\omega_0}{2} \end{bmatrix}.$$

In each sub-step the computation is performed as follows. First, calculate the auxiliary magnetic fields via the magnetic fields; second, substitute the auxiliary magnetic field into the difference equation for the electric fields; third, compute the electric fields implicitly and the magnetic fields explicitly; finally, update the auxiliary electric fields. As an example, $\tilde{E}_x$ and $\tilde{H}_z$ are calculated by expanding the matrices in the first sub-step as

$$\tilde{e}_x|^n_{i,j,k} = 2\tilde{E}_x|^n_{i,j,k} - \tilde{e}_x|^{n-\frac{1}{4}}_{i,j,k}, \tag{6.42}$$

$$\tilde{h}_z|^n_{i,j,k} = 2\tilde{H}_z|^n_{i,j,k} - \tilde{h}_z|^{n-\frac{1}{4}}_{i,j,k}, \tag{6.43}$$

$$\tilde{E}_x|^{n+\frac{1}{4}}_{i,j,k} = AC \cdot (\tilde{H}_{zy}|^{n+\frac{1}{4}}_{i,j,k} - \tilde{H}_{zy}|^{n+\frac{1}{4}}_{i,j-1,k}) + C \cdot \tilde{e}_x|^n_{i,j,k}, \tag{6.44}$$

$$\tilde{H}_z|_{i,j,k}^{n+\frac{1}{4}} = BC \cdot (\tilde{E}_{xy}|_{i,j+1,k}^{n+\frac{1}{4}} - \tilde{E}_{xy}|_{i,j,k}^{n+\frac{1}{4}}) + C \cdot \tilde{h}_z|_{i,j,k}^{n}, \tag{6.45}$$

where $A = \frac{\Delta t}{4\Delta\epsilon}$, $B = \frac{\Delta t}{4\Delta\mu}$ and $C = \frac{8}{8+j\omega_0\Delta t}$. The CE equations in the NPML region are:

$$\frac{\partial}{\partial t}\tilde{H}_{zy} + j\omega_0\tilde{H}_{zy} + \frac{\sigma_y}{\epsilon}\tilde{H}_{zy} = \frac{\partial}{\partial t}\tilde{H}_z + j\omega\tilde{H}_z, \tag{6.46}$$

$$\frac{\partial}{\partial t}\tilde{E}_{xy} + j\omega_0\tilde{E}_{xy} + \frac{\sigma_y}{\epsilon}\tilde{E}_{xy} = \frac{\partial}{\partial t}\tilde{E}_x + j\omega\tilde{E}_x. \tag{6.47}$$

By discretizing the fields in the time domain and space domain, (6.46) and (6.47) can be written as

$$\begin{aligned}\frac{\tilde{H}_{zy}|_{i,j,k}^{n+\frac{1}{4}} - \tilde{H}_{zy}|_{i,j,k}^{n}}{\Delta t/4} &+ \frac{j\omega_0\epsilon + \sigma_y|_{i,j,k}}{2\epsilon}(\tilde{H}_{zy}|_{i,j,k}^{n+\frac{1}{4}} + \tilde{H}_{zy}|_{i,j,k}^{n}) \\ &= \frac{\tilde{H}_z|_{i,j,k}^{n+\frac{1}{4}} - \tilde{H}_z|_{i,j,k}^{n}}{\Delta t/4} + \frac{j\omega_0}{2}(\tilde{H}_z|_{i,j,k}^{n+\frac{1}{4}} - \tilde{H}_z|_{i,j,k}^{n}),\end{aligned} \tag{6.48}$$

$$\begin{aligned}\frac{\tilde{E}_{xy}|_{i,j,k}^{n+\frac{1}{4}} - \tilde{E}_{xy}|_{i,j,k}^{n}}{\Delta t/4} &+ \frac{j\omega_0\epsilon + \sigma_y|_{i,j,k}}{2\epsilon}(\tilde{E}_{xy}|_{i,j,k}^{n+\frac{1}{4}} + \tilde{E}_{xy}|_{i,j,k}^{n}) \\ &= \frac{\tilde{E}_x|_{i,j,k}^{n+\frac{1}{4}} - \tilde{E}_x|_{i,j,k}^{n}}{\Delta t/4} + \frac{j\omega_0}{2}(\tilde{E}_x|_{i,j,k}^{n+\frac{1}{4}} - \tilde{E}_x|_{i,j,k}^{n}).\end{aligned} \tag{6.49}$$

Upon rearranging the terms, (6.48) and (6.49) become

$$\tilde{H}_{zy}|_{i,j,k}^{n+\frac{1}{4}} = A_{y1}|_{i,j,k} \cdot \tilde{H}_{zy}|_{i,j,k}^{n} + A_{y2}|_{i,j,k} \cdot \tilde{H}_z|_{i,j,k}^{n+\frac{1}{4}} - A_{y3}|_{i,j,k} \cdot \tilde{H}_z|_{i,j,k}^{n}, \tag{6.50}$$

$$\tilde{E}_{xy}|_{i,j,k}^{n+\frac{1}{4}} = A_{y1}|_{i,j,k} \cdot \tilde{E}_{xy}|_{i,j,k}^{n} + A_{y2}|_{i,j,k} \cdot \tilde{E}_x|_{i,j,k}^{n+\frac{1}{4}} - A_{y3}|_{i,j,k} \cdot \tilde{E}_x|_{i,j,k}^{n}, \tag{6.51}$$

where

$$A_{y1}|_{i,j,k} = \frac{8\epsilon - j\omega_0\Delta t \cdot \epsilon - \Delta t \cdot \sigma_y|_{i,j,k}}{8\epsilon + j\omega_0\Delta t \cdot \epsilon + \Delta t \cdot \sigma_y|_{i,j,k}}, \tag{6.52}$$

$$A_{y2}|_{i,j,k} = \frac{8\epsilon + j\omega_0\Delta t \cdot \epsilon}{8\epsilon + j\omega_0\Delta t \cdot \epsilon + \Delta t \cdot \sigma_y|_{i,j,k}}, \tag{6.53}$$

$$A_{y3}|_{i,j,k} = \frac{8\epsilon - j\omega_0\Delta t \cdot \epsilon}{8\epsilon + j\omega_0\Delta t \cdot \epsilon + \Delta t \cdot \sigma_y|_{i,j,k}}. \tag{6.54}$$

Substitution of (6.51) into (6.45) yields

$$\begin{aligned}\tilde{H}_z|_{i,j,k}^{n+\frac{1}{4}} &= BC \cdot (A_{y1}|_{i,j+1,k} \cdot \tilde{E}_{xy}|_{i,j+1,k}^{n} + A_{y2}|_{i,j+1,k} \cdot \tilde{E}_x|_{i,j+1,k}^{n+\frac{1}{4}} - A_{y3}|_{i,j+1,k} \cdot \tilde{E}_x|_{i,j+1,k}^{n}) \\ &\quad - BC \cdot (A_{y1}|_{i,j,k} \cdot \tilde{E}_{xy}|_{i,j,k}^{n} + A_{y2}|_{i,j,k} \cdot \tilde{E}_x|_{i,j,k}^{n+\frac{1}{4}} - A_{y3}|_{i,j,k} \cdot \tilde{E}_x|_{i,j,k}^{n}) + C \cdot \tilde{h}_z|_{i,j,k}^{n}.\end{aligned} \tag{6.55}$$

Then, by substituting (6.55) into (6.50), $\tilde{H}_{zy}|_{i,j,k}^{n+\frac{1}{4}}$ is represented as

$$\begin{aligned}\tilde{H}_{zy}|_{i,j,k}^{n+\frac{1}{4}} &= A_{y1}|_{i,j,k} \cdot \tilde{H}_{zy}|_{i,j,k}^{n} + C \cdot A_{y2}|_{i,j,k} \cdot \tilde{h}_z|_{i,j,k}^{n} - A_{y3}|_{i,j,k} \cdot \tilde{H}_z|_{i,j,k}^{n} \\ &+ BC \cdot A_{y2}|_{i,j,k} \cdot (A_{y1}|_{i,j+1,k} \cdot \tilde{E}_{xy}|_{i,j+1,k}^{n} + A_{y2}|_{i,j+1,k} \cdot \tilde{E}_x|_{i,j+1,k}^{n+\frac{1}{4}} - A_{y3}|_{i,j+1,k} \cdot \tilde{E}_x|_{i,j+1,k}^{n}) \\ &- BC \cdot A_{y2}|_{i,j,k} \cdot (A_{y1}|_{i,j,k} \cdot \tilde{E}_{xy}|_{i,j,k}^{n} + A_{y2}|_{i,j,k} \cdot \tilde{E}_x|_{i,j,k}^{n+\frac{1}{4}} - A_{y3}|_{i,j,k} \cdot \tilde{E}_x|_{i,j,k}^{n}).\end{aligned} \tag{6.56}$$

Finally substitution of (6.56) into (6.44) yields

$$
\begin{aligned}
\tilde{E}_x|_{i,j,k}^{n+\frac{1}{4}} &- ABC^2 \cdot A_{y2}|_{i,j,k} \cdot A_{y2}|_{i,j+1,k} \cdot \tilde{E}_x|_{i,j+1,k}^{n+\frac{1}{4}} \\
&- ABC^2 \cdot A_{y2}|_{i,j,k} \cdot A_{y2}|_{i,j,k} \cdot \tilde{E}_x|_{i,j,k}^{n+\frac{1}{4}} \\
&- ABC^2 \cdot A_{y2}|_{i,j-1,k} \cdot A_{y2}|_{i,j,k} \cdot \tilde{E}_x|_{i,j,k}^{n+\frac{1}{4}} \\
&- ABC^2 \cdot A_{y2}|_{i,j-1,k} \cdot A_{y2}|_{i,j-1,k} \cdot \tilde{E}_x|_{i,j-1,k}^{n+\frac{1}{4}} \\
= &- ABC^2 \cdot A_{y2}|_{i,j,k} \cdot A_{y3}|_{i,j+1,k} \cdot \tilde{E}_x|_{i,j+1,k}^{n} \\
&+ ABC^2 \cdot A_{y2}|_{i,j,k} \cdot A_{y3}|_{i,j,k} \cdot \tilde{E}_x|_{i,j,k}^{n} \\
&+ ABC^2 \cdot A_{y2}|_{i,j-1,k} \cdot A_{y3}|_{i,j,k} \cdot \tilde{E}_x|_{i,j,k}^{n} \\
&- ABC^2 \cdot A_{y2}|_{i,j-1,k} \cdot A_{y3}|_{i,j-1,k} \cdot \tilde{E}_x|_{i,j-1,k}^{n} \\
&+ ABC^2 \cdot A_{y2}|_{i,j,k} \cdot A_{y1}|_{i,j+1,k} \cdot \tilde{E}_{xy}|_{i,j+1,k}^{n} \\
&- ABC^2 \cdot A_{y2}|_{i,j,k} \cdot A_{y1}|_{i,j,k} \cdot \tilde{E}_{xy}|_{i,j,k}^{n} \\
&- ABC^2 \cdot A_{y2}|_{i,j-1,k} \cdot A_{y1}|_{i,j,k} \cdot \tilde{E}_{xy}|_{i,j,k}^{n} \\
&+ ABC^2 \cdot A_{y2}|_{i,j-1,k} \cdot A_{y1}|_{i,j-1,k} \cdot \tilde{E}_{xy}|_{i,j-1,k}^{n} \\
&+ AC \cdot (A_{y1}|_{i,j,k} \cdot \tilde{H}_{zy}|_{i,j,k}^{n} - A_{y1}|_{i,j-1,k} \cdot \tilde{H}_{zy}|_{i,j-1,k}^{n}) \\
&+ AC^2 \cdot (A_{y2}|_{i,j,k} \cdot \tilde{h}_z|_{i,j,k}^{n} - A_{y2}|_{i,j-1,k} \cdot \tilde{h}_z|_{i,j-1,k}^{n}) \\
&- AC \cdot (A_{y3}|_{i,j,k} \cdot \tilde{H}_z|_{i,j,k}^{n} - A_{y3}|_{i,j-1,k} \cdot \tilde{H}_z|_{i,j-1,k}^{n}) \\
&+ C \cdot \tilde{e}_x|_{i,j,k}. \qquad (6.57)
\end{aligned}
$$

As with (6.31), the coefficient matrix of $\tilde{E}_x|^{n+\frac{1}{4}}$ is tridiagonal. The fields $\tilde{E}_x$, $\tilde{H}_z$, and the corresponding auxiliary fields in sub-step 1, are calculated according to the following procedure: first, update $\tilde{e}_x|^{n+\frac{1}{4}}$ and $\tilde{h}_z|^{n+\frac{1}{4}}$ in (6.42) and (6.43); then update $\tilde{E}_x|^{n+\frac{1}{4}}$ in (6.57); third, update $\tilde{E}_{xy}|^{n+\frac{1}{4}}$ in (6.51); then update $\tilde{H}_z|^{n+\frac{1}{4}}$ in (6.45); finally, update $\tilde{H}_{zy}|^{n+\frac{1}{4}}$ by (6.50).

There are 15 terms in (6.57), whereas the number of terms in the implicit equation for

$\tilde{E}_x$ based on the CE-ADI-FDTD with NPML is 21. By applying the fundamental scheme, then, the number of terms is reduced by 28.57%. At each time step of the 3D simulation, the implicit equations are solved multiple times, so that the reduction in the number of terms accumulates and greatly reduces the overall computational time. With the NPML, then, the proposed CE-FADI-FDTD algorithm provides much greater computational efficiency than CE-ADI-FDTD.

### 6.3.1 3D CE-4S-FADI-FDTD with TFSF and NPML

To solve electromagnetic problems associated with excitation by a plane wave source, the TFSF scheme is incorporated into the 3D CE-4S-FADI-FDTD formulation. As with the 2D TFSF scheme, the 3D TFSF scheme requires an auxiliary grid for modeling of the incident wave.

#### 6.3.1.1 1D Auxiliary Grid

In accordance with the CE-4S-FADI-FDTD employed in the 3D domain, the same algorithm is required for the 1D Auxiliary grid. For $\tilde{E}_z$ and $\tilde{H}_y$, the four sub-steps algorithm is specified as follows:

sub-step 1

$$\tilde{e_z}|_i^n = 2\tilde{E}_z|_i^n - \tilde{e}_z|_i^{n-\frac{1}{4}} - \frac{\Delta t}{4\epsilon}\tilde{J}_z|_i^{n+\frac{1}{8}}, \tag{6.58}$$

$$\tilde{h_y}|_i^n = 2\tilde{H}_y|_i^n - \tilde{h}_y|_i^{n-\frac{1}{4}}, \tag{6.59}$$

$$\tilde{E}_z|_i^{n+\frac{1}{4}} + \frac{j\omega_0\Delta t}{8}\tilde{E}_z|_i^{n+\frac{1}{4}} - \frac{\Delta t}{4\epsilon\Delta x}(\tilde{H}_y|_i^{n+\frac{1}{4}} - \tilde{H}_y|_{i-1}^{n+\frac{1}{4}}) = \tilde{e}_z|_i^n, \tag{6.60}$$

$$\tilde{H}_y|_i^{n+\frac{1}{4}} + \frac{j\omega_0\Delta t}{8}\tilde{H}_y|_i^{n+\frac{1}{4}} - \frac{\Delta t}{4\mu\Delta x}(\tilde{E}_z|_{i+1}^{n+\frac{1}{4}} - \tilde{E}_z|_i^{n+\frac{1}{4}}) = \tilde{h}_y|_i^n. \tag{6.61}$$

sub-step 2

$$\tilde{e_z}|_i^{n+\frac{1}{4}} = 2\tilde{E}_z|_i^{n+\frac{1}{4}} - \tilde{e}_z|_i^n - \frac{\Delta t}{4\epsilon}\tilde{J}_z|_i^{n+\frac{3}{8}}, \tag{6.62}$$

$$\tilde{h_y}|_i^{n+\frac{1}{4}} = 2\tilde{H}_y|_i^{n+\frac{1}{4}} - \tilde{h}_y|_i^n, \tag{6.63}$$

$$\tilde{E}_z|_i^{n+\frac{1}{2}} + \frac{j\omega_0\Delta t}{8}\tilde{E}_z|_i^{n+\frac{1}{2}} = \tilde{e}_z|_i^{n+\frac{1}{4}}, \tag{6.64}$$

$$\tilde{H}_y|_i^{n+\frac{1}{2}} + \frac{j\omega_0\Delta t}{8}\tilde{H}_y|_i^{n+\frac{1}{2}} = \tilde{h}_y|_i^{n+\frac{1}{4}}. \tag{6.65}$$

sub-step 3

$$\tilde{e_z}|_i^{n+\frac{1}{2}} = 2\tilde{E}_z|_i^{n+\frac{1}{2}} - \tilde{e}_z|_i^{n+\frac{1}{4}} - \frac{\Delta t}{4\epsilon}\tilde{J}_z|_i^{n+\frac{5}{8}}, \tag{6.66}$$

$$\tilde{h_y}|_i^{n+\frac{1}{2}} = 2\tilde{H}_y|_i^{n+\frac{1}{2}} - \tilde{h}_y|_i^{n+\frac{1}{4}}, \tag{6.67}$$

$$\tilde{E}_z|_i^{n+\frac{3}{4}} + \frac{j\omega_0\Delta t}{8}\tilde{E}_z|_i^{n+\frac{3}{4}} - \frac{\Delta t}{4\epsilon\Delta x}(\tilde{H}_y|_i^{n+\frac{3}{4}} - \tilde{H}_y|_{i-1}^{n+\frac{3}{4}}) = \tilde{e}_z|_i^{n+\frac{1}{2}}, \tag{6.68}$$

$$\tilde{H}_y|_i^{n+\frac{3}{4}} + \frac{j\omega_0\Delta t}{8}\tilde{H}_y|_i^{n+\frac{3}{4}} - \frac{\Delta t}{4\mu\Delta x}(\tilde{E}_z|_{i+1}^{n+\frac{3}{4}} - \tilde{E}_z|_i^{n+\frac{3}{4}}) = \tilde{h}_y|_i^{n+\frac{1}{2}}. \tag{6.69}$$

sub-step 4

$$\tilde{e_z}|_i^{n+\frac{3}{4}} = 2\tilde{E}_z|_i^{n+\frac{3}{4}} - \tilde{e}_z|_i^{n+\frac{1}{2}} - \frac{\Delta t}{4\epsilon}\tilde{J}_z|_i^{n+\frac{7}{8}}, \tag{6.70}$$

$$\tilde{h_y}|_i^{n+\frac{3}{4}} = 2\tilde{H}_y|_i^{n+\frac{3}{4}} - \tilde{h}_y|_i^{n+\frac{1}{2}}, \tag{6.71}$$

$$\tilde{E}_z|_i^{n+1} + \frac{j\omega_0\Delta t}{8}\tilde{E}_z|_i^{n+1} = \tilde{e}_z|_i^{n+\frac{3}{4}}, \tag{6.72}$$

$$\tilde{H}_y|_i^{n+1} + \frac{j\omega_0 \Delta t}{8} \tilde{H}_y|_i^{n+1} = \tilde{h}_y|_i^{n+\frac{3}{4}}. \tag{6.73}$$

At each sub-step the equations are solved in the same order as in the 3D CE-4S-FADI-FDTD algorithm. For example, in sub-step 1 the auxiliary fields are solved explicitly first; then, substitution of (6.61) into (6.60) yields the implicit equation with a tridiagonal coefficient matrix, by which $\tilde{E}_z$ is solved implicitly; finally, by substituting $\tilde{E}_z$ into (6.61), $\tilde{H}_y$ is updated explicitly.

#### 6.3.1.2 3D Field Correction

To simplify the equations, the spatial steps are set to be identical in all directions. Figure 6.2 shows the total field region and the TF/SF boundary in the 3D model, and Figure 6.3 shows the six faces of the total field region. Cell $(Is1, Js1, Ks1)$ is in the total field region. By implementing the 2D CE-4S-ADI-FDTD in Ramadan (2009), after labeling the fields in the total field region and in the scattered field region, with $\Delta x = \Delta y = \Delta z = \Delta$ and $\Delta t \rightarrow \frac{\Delta t}{2}$, the 3D implicit equation for $\tilde{E}_x$ is written as

$$\begin{aligned}
&\frac{8 + j\omega_0 \Delta t}{8} \tilde{E}_{x,tot}|_{Is1,Js1,Ks1}^{n+\frac{1}{4}} - \frac{\Delta t}{4\Delta\epsilon|_{Is1,Js1,Ks1}} (\tilde{H}_{zy,tot}|_{Is1,Js1,Ks1}^{n+\frac{1}{4}} - \tilde{H}_{zy,scat}|_{Is1,Js1-1,Ks1}^{n+\frac{1}{4}}) \\
&= \frac{8 - j\omega_0 \Delta t}{8} \tilde{E}_{x,tot}|_{Is1,Js1,Ks1}^{n} - \frac{\Delta t}{4\Delta\epsilon|_{Is1,Js1,Ks1}} (\tilde{H}_{yz,tot}|_{Is1,Js1,Ks1}^{n} - \tilde{H}_{yz,scat}|_{Is1,Js1,Ks1-1}^{n}).
\end{aligned} \tag{6.74}$$

By applying the field correction method, (6.74) becomes

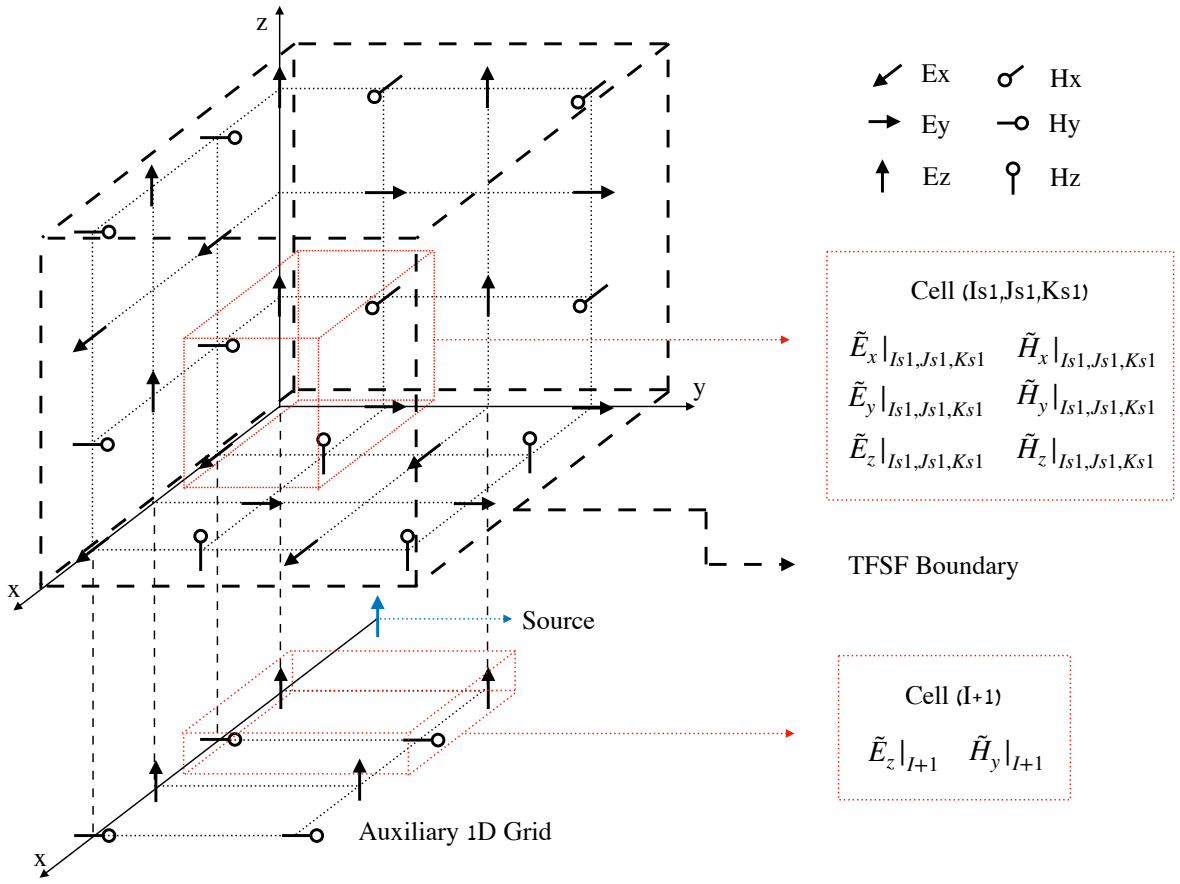


Figure 6.2. The 3D TF/SF Grid.

$$\frac{8+j\omega_0\Delta t}{8}\tilde{E}_{x,tot}|^{n+\frac{1}{4}}_{Is1,Js1,Ks1}$$
$$-\frac{\Delta t}{4\Delta\epsilon|_{Is1,Js1,Ks1}}[\tilde{H}_{zy,tot}|^{n+\frac{1}{4}}_{Is1,Js1,Ks1}-(\tilde{H}_{zy,tot}|^{n+\frac{1}{4}}_{Is1,Js1-1,Ks1}-\tilde{H}_{zy,inc}|^{n+\frac{1}{4}}_{Is1,Js1-1,Ks1})]$$
$$=\frac{8-j\omega_0\Delta t}{8}\tilde{E}_{x,tot}|^{n}_{Is1,Js1,Ks1}$$
$$-\frac{\Delta t}{4\Delta\epsilon|_{Is1,Js1,Ks1}}[\tilde{H}_{yz,tot}|^{n}_{Is1,Js1,Ks1}-(\tilde{H}_{yz,tot}|^{n}_{Is1,Js1,Ks1-1}-\tilde{H}_{yz,inc}|^{n}_{Is1,Js1,Ks1-1})]. \quad (6.75)$$

The incident field is defined on the TF/SF boundary, which is in the computational domain. The fictitious conductivities are non-zero in the PML region, and accordingly $\sigma_x = \sigma_y = \sigma_z = 0$ in the computational domain. Therefore $\tilde{H}_{zy} = \tilde{H}_z$, $\tilde{H}_{zy,inc} = \tilde{H}_{z,inc}$, and similarly $\tilde{H}_{yz,inc} = \tilde{H}_{y,inc}$. The incident fields are obtained from Cell I+1 in the 1D auxiliary grid, and only $\tilde{E}_{z,inc}$ and $\tilde{H}_{y,inc}$ exist, so that $\tilde{H}_{zy,inc} = 0$. After that, (6.75) is rewritten as

$$\begin{aligned}
&\frac{8 + j\omega_0\Delta t}{8}\tilde{E}_{x,tot}|^{n+\frac{1}{4}}_{Is1,Js1,Ks1} \\
&- \frac{\Delta t}{4\Delta\epsilon|_{Is1,Js1,Ks1}}[\tilde{H}_{zy,tot}|^{n+\frac{1}{4}}_{Is1,Js1,Ks1} - \tilde{H}_{zy,tot}|^{n+\frac{1}{4}}_{Is1,Js1-1,Ks1}] \\
= &\frac{8 - j\omega_0\Delta t}{8}\tilde{E}_{x,tot}|^{n}_{Is1,Js1,Ks1} \\
&- \frac{\Delta t}{4\Delta\epsilon|_{Is1,Js1,Ks1}}[\tilde{H}_{yz,tot}|^{n}_{Is1,Js1,Ks1} - \tilde{H}_{yz,tot}|^{n}_{Is1,Js1,Ks1-1}] \\
&- \frac{\Delta t}{4\Delta\epsilon|_{Is1,Js1,Ks1}}\tilde{H}_{y,inc}|^{n}_{Is1,Js1,Ks1-1},
\end{aligned} \tag{6.76}$$

where

$$\tilde{H}_{y,inc}|^{n}_{Is1,Js1,Ks1-1} = \tilde{H}_{y,1D}|^{n}_{I+1}. \tag{6.77}$$

In (6.76), the incident field from the 1D auxiliary grid is treated as a regular source, and the form of the equation is the same as (3.32) based on the CE-ADI-FDTD. The incident fields in other equations can be found in the same manner. Then, with the TFSF scheme, after correcting the fields, all of the equations are same as the equations in CE-4S-ADI-FDTD except that the source fields $\tilde{J}$ and $\tilde{M}$ are represented by the incident fields. By substituting the incident fields into the source functions in (6.11), the sources of the CE-4S-FADI-FDTD are defined. Finally, by following the sub-steps from (6.34) to (6.41), the TF/SF scheme can be incorporated into the 3D CE-4S-FADI-FDTD and NPML algorithm.

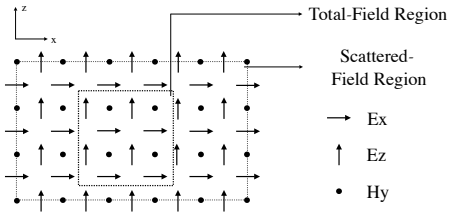


(a) Left

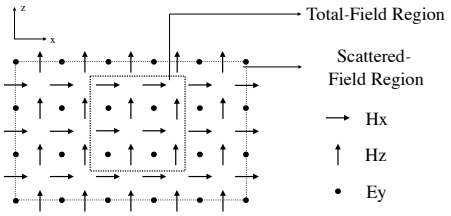


(b) Right

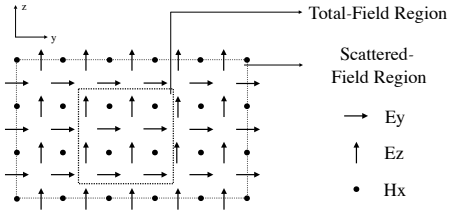


(c) Back

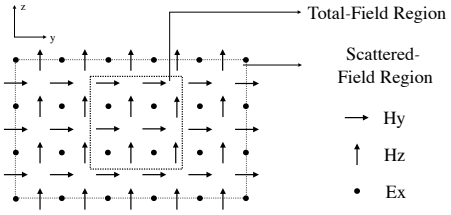


(d) Front

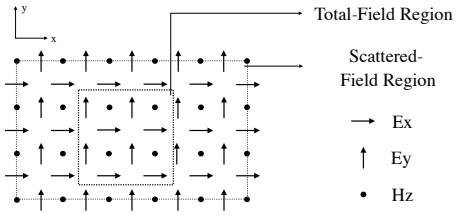


(e) Bottom

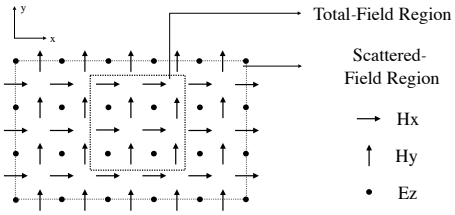


(f) Top

Figure 6.3. The six faces of the total field region.

# CHAPTER 7

# REFERENCE METHODS

In this chapter, three reference methods are developed for comparison with the proposed 3D CE-4S-FADI-FDTD algorithm, corresponding to differing boundary conditions and excitation sources.

## 7.1 Point Source and PEC Boundaries

Based on the 3D CE-4S-FADI-FDTD, the CE fields have complex values, and the CE-FDTD in Ma (2006) has been developed to facilitate comparison of the real part, the imaginary part and the magnitude, starting with the vector CE Maxwell's equations as

$$\nabla \times \tilde{\mathbf{H}} = \epsilon \frac{\partial \tilde{\mathbf{E}}}{\partial t} + j\omega_0 \epsilon \tilde{\mathbf{E}} + \tilde{\mathbf{J}}, \tag{7.1}$$

$$\nabla \times \tilde{\mathbf{E}} = -\mu \frac{\partial \tilde{\mathbf{H}}}{\partial t} - j\omega_0 \mu \tilde{\mathbf{H}} - \tilde{\mathbf{M}}. \tag{7.2}$$

In the example provided in the next chapter, $\tilde{\mathbf{J}} = \hat{\mathbf{z}}\tilde{J}_z$ and $\tilde{\mathbf{M}} = \mathbf{0}$, and the vector CE Maxwell's equations can be represented by six CE scalar equations, as follows:

$$\frac{\partial}{\partial t}\tilde{H}_x + j\omega_0 \tilde{H}_x = -\frac{1}{\mu}\frac{\partial}{\partial y}\tilde{E}_z + \frac{1}{\mu}\frac{\partial}{\partial z}\tilde{E}_y, \tag{7.3}$$

$$\frac{\partial}{\partial t}\tilde{H}_y + j\omega_0 \tilde{H}_y = \frac{1}{\mu}\frac{\partial}{\partial x}\tilde{E}_z - \frac{1}{\mu}\frac{\partial}{\partial z}\tilde{E}_x, \tag{7.4}$$

$$\frac{\partial}{\partial t}\tilde{H}_z + j\omega_0 \tilde{H}_z = -\frac{1}{\mu}\frac{\partial}{\partial x}\tilde{E}_y + \frac{1}{\mu}\frac{\partial}{\partial y}\tilde{E}_x, \tag{7.5}$$

$$\frac{\partial}{\partial t}\tilde{E}_x + j\omega_0\tilde{E}_x = \frac{1}{\epsilon}\frac{\partial}{\partial y}\tilde{H}_z - \frac{1}{\epsilon}\frac{\partial}{\partial z}\tilde{H}_y, \tag{7.6}$$

$$\frac{\partial}{\partial t}\tilde{E}_y + j\omega_0\tilde{E}_y = -\frac{1}{\epsilon}\frac{\partial}{\partial x}\tilde{H}_z + \frac{1}{\epsilon}\frac{\partial}{\partial z}\tilde{H}_x, \tag{7.7}$$

$$\frac{\partial}{\partial t}\tilde{E}_z + j\omega_0\tilde{E}_z = \frac{1}{\epsilon}\frac{\partial}{\partial x}\tilde{H}_y - \frac{1}{\epsilon}\frac{\partial}{\partial y}\tilde{H}_x - \frac{1}{\epsilon}\tilde{J}_z. \tag{7.8}$$

The magnetic equations are centered at time instant $n$. By applying the second-order central difference approximation, it follows that $\frac{\partial}{\partial t}(\tilde{H}_x|^n_{i,j,k}) = \frac{\tilde{H}_x|^{n+\frac{1}{2}}_{i,j,k} - \tilde{H}_x|^{n-\frac{1}{2}}_{i,j,k}}{\Delta t}$. According to the average approximation, $j\omega_0\tilde{H}_x|^n_{i,j,k} = \frac{j\omega_0}{2}(\tilde{H}_x|^{n+\frac{1}{2}}_{i,j,k} + \tilde{H}_x|^{n-\frac{1}{2}}_{i,j,k})$. Finally, the discretized magnetic equation can be written as

$$\begin{aligned}\frac{\tilde{H}_x|^{n+\frac{1}{2}}_{i,j,k} - \tilde{H}_x|^{n-\frac{1}{2}}_{i,j,k}}{\Delta t} + \frac{j\omega}{2}(\tilde{H}_x|^{n+\frac{1}{2}}_{i,j,k} + \tilde{H}_x|^{n-\frac{1}{2}}_{i,j,k}) =& -\frac{1}{\mu\Delta y}(\tilde{E}_z|^n_{i,j+1,k} - \tilde{E}_z|^n_{i,j,k}) \\ &+ \frac{1}{\mu\Delta z}(\tilde{E}_y|^n_{i,j,k+1} - \tilde{E}_y|^n_{i,j,k}).\end{aligned} \tag{7.9}$$

Similarly, all of the other discretized equations are

$$\begin{aligned}\frac{\tilde{H}_y|^{n+\frac{1}{2}}_{i,j,k} - \tilde{H}_y|^{n-\frac{1}{2}}_{i,j,k}}{\Delta t} + \frac{j\omega_0}{2}(\tilde{H}_y|^{n+\frac{1}{2}}_{i,j,k} + \tilde{H}_y|^{n-\frac{1}{2}}_{i,j,k}) =& \frac{1}{\mu\Delta x}(\tilde{E}_z|^n_{i+1,j,k} - \tilde{E}_z|^n_{i,j,k}) \\ &- \frac{1}{\mu\Delta z}(\tilde{E}_x|^n_{i,j,k+1} - \tilde{E}_x|^n_{i,j,k}),\end{aligned} \tag{7.10}$$

$$\begin{aligned}\frac{\tilde{H}_z|^{n+\frac{1}{2}}_{i,j,k} - \tilde{H}_z|^{n-\frac{1}{2}}_{i,j,k}}{\Delta t} + \frac{j\omega_0}{2}(\tilde{H}_z|^{n+\frac{1}{2}}_{i,j,k} + \tilde{H}_z|^{n-\frac{1}{2}}_{i,j,k}) =& -\frac{1}{\mu\Delta x}(\tilde{E}_y|^n_{i+1,j,k} - \tilde{E}_y|^n_{i,j,k}) \\ &+ \frac{1}{\mu\Delta y}(\tilde{E}_x|^n_{i,j+1,k} - \tilde{E}_x|^n_{i,j,k}),\end{aligned} \tag{7.11}$$

$$\frac{\tilde{E}_x|_{i,j,k}^{n+1} - \tilde{E}_x|_{i,j,k}^{n}}{\Delta t} + \frac{j\omega_0}{2}(\tilde{E}_x|_{i,j,k}^{n+1} + \tilde{E}_x|_{i,j,k}^{n}) = \frac{1}{\epsilon\Delta y}(\tilde{H}_z|_{i,j,k}^{n+\frac{1}{2}} - \tilde{E}_z|_{i,j-1,k}^{n+\frac{1}{2}}) - \frac{1}{\epsilon\Delta z}(\tilde{H}_y|_{i,j,k}^{n+\frac{1}{2}} - \tilde{H}_y|_{i,j,k-1}^{n+\frac{1}{2}}), \tag{7.12}$$

$$\frac{\tilde{E}_y|_{i,j,k}^{n+1} - \tilde{E}_y|_{i,j,k}^{n}}{\Delta t} + \frac{j\omega_0}{2}(\tilde{E}_y|_{i,j,k}^{n+1} + \tilde{E}_y|_{i,j,k}^{n}) = -\frac{1}{\epsilon\Delta x}(\tilde{H}_z|_{i,j,k}^{n+\frac{1}{2}} - \tilde{H}_z|_{i-1,j,k}^{n+\frac{1}{2}}) + \frac{1}{\epsilon\Delta z}(\tilde{H}_x|_{i,j,k}^{n+\frac{1}{2}} - \tilde{H}_x|_{i,j,k-1}^{n+\frac{1}{2}}), \tag{7.13}$$

$$\frac{\tilde{E}_z|_{i,j,k}^{n+1} - \tilde{E}_z|_{i,j,k}^{n}}{\Delta t} + \frac{j\omega_0}{2}(\tilde{E}_z|_{i,j,k}^{n+1} + \tilde{E}_z|_{i,j,k}^{n}) = \frac{1}{\epsilon\Delta x}(\tilde{H}_y|_{i,j,k}^{n+\frac{1}{2}} - \tilde{H}_y|_{i-1,j,k}^{n+\frac{1}{2}}) - \frac{1}{\epsilon\Delta y}(\tilde{H}_x|_{i,j,k}^{n+\frac{1}{2}} - \tilde{H}_x|_{i,j-1,k}^{n+\frac{1}{2}}) - \frac{1}{\epsilon}\tilde{J}_z|_{i,j,k}^{n+\frac{1}{2}}. \tag{7.14}$$

As in the equations in the classical FDTD algorithm, the fields in each cell can be represented by a number of known terms in the equations, and can therefore be updated explicitly, as follows. At each time step, the magnetic fields are calculated first via (7.9), (7.10) and (7.11); then the magnetic fields are substituted into (7.12), (7.13) and (7.14) and the electric fields can be solved for.

## 7.2 Point Source and ABC

For the boundless problem, the reference method is based on the frequency-domain solution. The frequency-domain electric field at the observation point is calculated from the point source and the 3D free-space Green's function. Then the time-domain electric field is obtained through the inverse fast Fourier transform (IFFT). The point source used in the

3D CE-4S-FADI-FDTD with NPML is a z-directed Gaussian, and the source function is

$$\tilde{\mathbf{J}}|_{Is,Js,Ks} = \exp\left[-\frac{(t-t_0)^2}{2\sigma_0^2}\right]\hat{\mathbf{z}}. \tag{7.15}$$

where the point source is in Cell $(Is1, Js1, Ks1)$. The bandpass-limited source is then the modulated version of the CE Gaussian function, as follows:

$$\begin{aligned}\mathbf{J}(x',y',z',t) &= \exp\left[-\frac{(t-t_0)^2}{2\sigma_0^2}\right]\cos(2\pi f_0 t)\delta(x')\delta(y')\delta(z')\hat{\mathbf{z}} \\ &= \exp\left[-\frac{(t-t_0)^2}{2\sigma_0^2}\right]\frac{\exp(j\omega_0 t)+\exp(-j\omega_0 t)}{2}\delta(x')\delta(y')\delta(z')\hat{\mathbf{z}},\end{aligned} \tag{7.16}$$

where $(x', y', z')$ denotes the position of the point source. Upon taking the Fourier transform, the source function in the frequency domain can be calculated as

$$\begin{aligned}\mathbf{J}(x',y',z',\omega) &= \hat{\mathbf{z}}\frac{\delta(x')\delta(y')\delta(z')}{2}\int_{-\infty}^{\infty}\exp\left[-\frac{(t-t_0)^2}{2\sigma_0^2}\right]\cdot[\exp(j\omega_0 t)+\exp(-j\omega_0 t)]\cdot\exp(-j\omega t)dt \\ &= \hat{\mathbf{z}}\frac{\delta(x')\delta(y')\delta(z')}{2}\cdot\sigma_0\sqrt{2\pi}\cdot\left\{\left[-\frac{\sigma_0^2(\omega-\omega_0)^2}{2}\right]\cdot\exp\left[-j(\omega-\omega_0)t_0\right]\right. \\ &\qquad \left.+\exp\left[-\frac{\sigma_0^2(\omega+\omega_0)^2}{2}\right]\cdot\exp\left[-j(\omega+\omega_0)t_0\right]\right\}\end{aligned} \tag{7.17}$$

From Balanis (2011), the electric vector potential $\mathbf{A}$ can be obtained as follows:

$$\begin{aligned}\mathbf{A}(x,y,z,\omega) &= \frac{\mu}{4\pi}\iiint_V \mathbf{J}(x',y',z',\omega)\frac{\exp[-j\beta\sqrt{(x-x')^2+(y-y')^2+(z-z')^2}]}{4\pi\sqrt{(x-x')^2+(y-y')^2+(z-z')^2}}dv' \\ &= \hat{\mathbf{z}}\frac{\mu}{4\pi}\sigma_0\sqrt{2\pi}\exp\Big[-\frac{\sigma_0^2(\omega-\omega_0)^2}{2}\Big]\cdot\exp\Big[-j(\omega-\omega_0)t_0\Big]\cdot\frac{-j\beta r}{r} \\ &+ \hat{\mathbf{z}}\frac{\mu}{4\pi}\sigma_0\sqrt{2\pi}\exp\Big[-\frac{\sigma_0^2(\omega+\omega_0)^2}{2}\Big]\cdot\exp\Big[-j(\omega+\omega_0)t_0\Big]\cdot\frac{-j\beta r}{r},\end{aligned} \tag{7.18}$$

where $r = \sqrt{x^2 + y^2 + z^2}$ and $\beta = \frac{\omega}{c_0}$. The electric field at the observation point is calculated as

$$\mathbf{E}(x, y, z, \omega) = -j\omega\mathbf{A} - j\frac{1}{\omega\mu\epsilon}\nabla(\nabla \cdot \mathbf{A}). \tag{7.19}$$

Upon substituting (7.17) into (7.18) and the result into (7.19), then eliminating the terms containing $(\omega + \omega_0)$ and doubling the magnitude, the CE electric field $\tilde{E}_z$ for an observation cell in the FDTD grid is given by

$$\begin{aligned}
\tilde{E}_z(x, y, z, \omega) =& \frac{-j\omega}{r} \cdot B_0 \cdot \exp(-j\beta r) \\
&- \frac{j}{\omega\mu\epsilon} \cdot B_0 \cdot \left(-\frac{\beta^2 z^2}{r^3}\right) \exp(-j\beta r) \\
&- \frac{j}{\omega\mu\epsilon} \cdot B_0 \cdot \left(\frac{j\beta z^2}{r^4}\right) \exp(-j\beta r) \\
&- \frac{j}{\omega\mu\epsilon} \cdot B_0 \cdot \left(-\frac{j\beta}{r^2}\right) \exp(-j\beta r) \\
&- \frac{j}{\omega\mu\epsilon} \cdot B_0 \cdot \left(\frac{2j\beta z^2}{r^4}\right) \exp(-j\beta r) \\
&- \frac{j}{\omega\mu\epsilon} \cdot B_0 \cdot \left(\frac{3z^2}{r^5}\right) \exp(-j\beta r) \\
&- \frac{j}{\omega\mu\epsilon} \cdot B_0 \cdot \left(-\frac{1}{r^3}\right) \exp(-j\beta r),
\end{aligned} \tag{7.20}$$

where

$$B_0 = (\Delta x \Delta y \Delta z)\frac{\mu}{4\pi}\sigma_0\sqrt{2\pi}\exp\left[-\frac{\sigma_0^2(\omega - \omega_0)^2}{2}\right] \cdot \exp\left[-j(\omega - \omega_0)t_0\right] \tag{7.21}$$

and $\Delta x$, $\Delta y$ and $\Delta z$ are the spatial steps in the 3D FDTD grid. The time-domain solution can finally be obtained by IFFT as

$$\tilde{E}_z(x, y, z, t) = IFFT\Big\{\tilde{E}_z(x, y, z, \omega)\Big\}. \tag{7.22}$$

## 7.3 Plane Wave Source and ABC

Figure 7.1 shows the model for the 3D scattering problem excited by a plane wave source in the boundless domain. The incident field is defined on a surface $S$, which is parallel to the $y-z$ plane. As in the 3D TFSF scheme, the incident wave is obtained from the 1D auxiliary grid. The time-domain source function in the 1D auxiliary grid is given by

$$\mathbf{J}(x',t) = \frac{2}{\eta}\exp\left[-\frac{(t-t_0)^2}{2\sigma_0^2}\right]\cos(2\pi f_0 t)\delta(x'-x_0)\hat{\mathbf{z}}. \tag{7.23}$$

With the CE algorithm and the Fourier transform, the CE source function in the frequency domain can then be obtained as

$$\begin{aligned} J_z(x',\omega) = {} & \hat{\mathbf{z}}\delta(x'-x_0)\cdot\frac{2}{\eta}\sigma_0\sqrt{2\pi}\cdot\exp\left[-\frac{\sigma_0^2(\omega-\omega_0)^2}{2}\right]\cdot\exp\left[-j(\omega-\omega_0)t_0\right] \\ & + \hat{\mathbf{z}}\delta(x'-x_0)\cdot\frac{2}{\eta}\sigma_0\sqrt{2\pi}\cdot\exp\left[-\frac{\sigma_0^2(\omega+\omega_0)^2}{2}\right]\cdot\exp\left[-j(\omega+\omega_0)t_0\right] \end{aligned} \tag{7.24}$$

By using the 1D free-space Green's function, the incident wave $E_z$ can be calculated as

$$E_{z,inc}(x,\omega) = -j\omega\mu\int_{-\infty}^{\infty} J_z(x',\omega)\cdot G_{1D}(x,x')dx'. \tag{7.25}$$

By eliminating the terms containing $(\omega+\omega_0)$ and doubling the magnitude, the CE incident electric field is obtained as

$$\tilde{E}_{z,inc}(x,\omega) = -j\omega\mu \int_{-\infty}^{\infty} \frac{2}{\eta}\sigma_0\sqrt{2\pi}\cdot 2\exp\left[-\frac{\sigma_0^2(\omega-\omega_0)^2}{2}\right]\cdot\exp\left[-j(\omega-\omega_0)t_0\right]$$
$$\cdot\left[\frac{-j\exp(-j\beta|x-x'|)}{2\beta}\right]\delta(x'-x_0)dx'$$
$$= -\sigma_0\sqrt{2\pi}\cdot\exp\left[-\frac{\sigma_0^2(\omega-\omega_0)^2}{2}\right]\cdot\exp\left[-j(\omega-\omega_0)t_0\right]\cdot\exp\left[-j\frac{\omega}{c_0}(x_0-x)\right]. \tag{7.26}$$

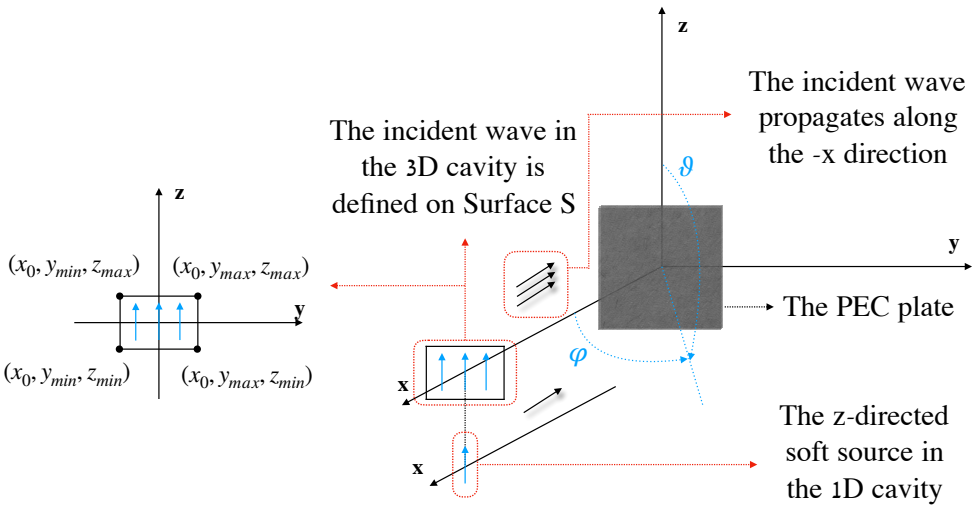


Figure 7.1. The 3D MOM model.

Upon utilizing the method of moments based on the volume integral equations (VIE-MOM) in Sefer et al. (2015), the PEC plate is divided into a number of cubic cells. The total fields $\bar{\bar{E}}_x$, $\bar{\bar{E}}_y$ and $\bar{\bar{E}}_z$ in each cell are taken as constant. In the case of the 3D CE-4S-

FADI-FDTD with TFSF, only $\tilde{E}_{z,inc}$ is nonzero, and $\tilde{E}_{x,inc} = \tilde{E}_{y,inc} = 0$. The VIE-MOM solution then begins with a system of equations as

$$\begin{bmatrix} \bar{G}_{xx} & \bar{G}_{xy} & \bar{G}_{xz} \\ \bar{G}_{xy} & \bar{G}_{yy} & \bar{G}_{yz} \\ \bar{G}_{xz} & \bar{G}_{yz} & \bar{G}_{zz} \end{bmatrix} \begin{bmatrix} \bar{\tilde{E}}_x \\ \bar{\tilde{E}}_y \\ \bar{\tilde{E}}_z \end{bmatrix} = \begin{bmatrix} 0 \\ 0 \\ \bar{\tilde{E}}_{z,inc} \end{bmatrix},$$

where

$$G_{pq}^{mn} = \begin{cases} 0 & \text{if } p \neq q \text{ and } n = m \\ 1 - k_0^2 v(r_m) D_1 & \text{if } p = q \text{ and } n = m \\ -k_0^2 v(r_m) D_2 \left( \delta_{pq} + \frac{\partial^2}{k_0^2 \partial x_p \partial x_q} \right) g(\mathbf{r}', \mathbf{r})|_{r'=r_m}^{r=r_n} & \text{otherwise} \end{cases}, \tag{7.27}$$

Here, $\bar{G}_{pq}(p, q = x, y, z)$ is an $N \times N$ matrix, $\bar{\tilde{E}}_{z,inc}$ is an $N \times 1$ vector and the wave number in free space $k_0 = \omega\sqrt{\epsilon\mu}$. With $\exp(j\omega t)$ assumed in (7.27),

$$D_1 = \frac{1}{3k_0^2}[(1 + jk_0)\exp(-jk_0 a) - 1], \tag{7.28}$$

$$D_2 = \frac{4\pi a}{k_0^2}\left[\frac{\sin(k_0 a)}{k_0 a} - \cos(k_0 a)\right], \tag{7.29}$$

$$v(\mathbf{r}) = \frac{k(\mathbf{r})}{k_0} - 1 \qquad \text{(object function)}. \tag{7.30}$$

The total electric field is calculated via

$$\tilde{\mathbf{E}}(\mathbf{r}) = \tilde{\mathbf{E}}_{inc}(\mathbf{r}) + j\omega\mu \int_{\mathbf{r}' \in V} \bar{\tilde{G}}(\mathbf{r}, \mathbf{r}')\tilde{\mathbf{J}}(\mathbf{r}')dV, \tag{7.31}$$

where the induced equivalent volume current density is represented as

$$\tilde{\mathbf{J}}(\mathbf{r}) = -j\omega\epsilon v(\mathbf{r})\tilde{\mathbf{E}}(\mathbf{r}). \tag{7.32}$$

At any point in the cavity, the total field is the superposition of the incident field and the scattered field:

$$\tilde{\mathbf{E}}(\mathbf{r}) = \tilde{\mathbf{E}}_{inc}(\mathbf{r}) + \tilde{\mathbf{E}}_{scat}(\mathbf{r}). \tag{7.33}$$

The scattered field can finally be obtained as

$$\tilde{\mathbf{E}}_{scat}(\mathbf{r}) = k_0^2 \int\limits_{\mathbf{r}' \in V} \bar{\bar{G}}(\mathbf{r}, \mathbf{r}') v(\mathbf{r}') \tilde{\mathbf{E}}(\mathbf{r}') dV. \tag{7.34}$$

In the Matlab program from Sefer et al. (2015), (7.34) is solved by

$$\begin{bmatrix} \bar{\bar{E}}_{x,scat} \\ \bar{\bar{E}}_{y,scat} \\ \bar{\bar{E}}_{z,scat} \end{bmatrix} = - \begin{bmatrix} \bar{G}_{xx} & \bar{G}_{xy} & \bar{G}_{xz} \\ \bar{G}_{xy} & \bar{G}_{yy} & \bar{G}_{yz} \\ \bar{G}_{xz} & \bar{G}_{yz} & \bar{G}_{zz} \end{bmatrix} \begin{bmatrix} \bar{\bar{E}}_x \\ \bar{\bar{E}}_y \\ \bar{\bar{E}}_z \end{bmatrix}.$$

Finally, the time-domain scattering field at the observation point is obtained by IFFT.

# CHAPTER 8

# EXAMPLES AND RESULTS

## 8.1 Point Source and PEC Boundaries

A 3D cavity example is now considered in order to compare the CE-4S-FADI-FDTD, the CE-ADI-FDTD and the classical FDTD algorithms. The medium inside the cavity is free space, and a z-directed electric current source is placed at the center of the cavity. The spatial steps are set equal in each direction: $\Delta = \Delta x = \Delta y = \Delta z = 0.2855$ m. The cavity is $47 \times 47 \times 47$ cells in size, and the point source is at $(24, 24, 24)$. The domain of the computation is truncated by perfect electric conductor (PEC) boundaries in all directions. The source emits a modulated Gaussian pulse:

$$J_z(t) = \exp\left[-\left(\frac{t - t_0}{\sqrt{2}\sigma_0}\right)^2\right] \cos(2\pi f_0 t), \tag{8.1}$$

where the center frequency $f_0 = 100$ MHz, the bandwidth $bw = 10$ MHz, $\sigma_0 = 9.0032 \times 10^{-8}$ s, the time step $\Delta t = 0.54986$ $n$s for CFLN= 1, and $t_0 = 720.25$ $n$s. Figure 8.1 gives a visual comparison of $\tilde{E}_z$ at the observation point $(14, 24, 24)$ according to the CE-ADI-FDTD and the proposed CE-4S-FADI-FDTD. The CE expression of the electric field is given by $\tilde{E}_z = E_z^p + jE_z^q$. Therefore $E_z^p$ represents the real part of $\tilde{E}_z$, which is shown in the top sub-figure of Figure 8.1. The observation point is 10 cells distant from the source point, and the time delay of the Gaussian is around 0.72 $\mu$s; consequently, the first half of the Gaussian can be seen at around $t = 0.8$ $\mu$s. The Gaussian source is narrow in the frequency domain, and therefore wide in the time domain. In contrast, the size of the cubic cavity is relatively small, at less than $4.5\lambda_{min}$ in each direction. As a result of the PEC boundaries, the reflected fields can be seen without a long simulation time. Accordingly,

after $t = 0.8$ $\mu$s the incident field from the source and the reflected field from the boundary reach the observation point. Superposition of the incident field and the reflected field forms the peak at around $t = 1.1$ $\mu$s. Similar trends are seen in the middle sub-figure for the imaginary part of $\tilde{E}_z$ and in the bottom sub-figure for the magnitude of $\tilde{E}_z$.

The reference method here is CE-FDTD with CFLN= 1. As can be seen, with CFLN= 1, both the CE-ADI-FDTD and the CE-4S-FADI-FDTD algorithms yield results with high accuracy. To accelerate the simulation a large CFLN is needed, which leads to a decline in accuracy of the implicit methods. Because of the 4S scheme, the CE-4S-ADI-FDTD algorithm is much more accurate than the CE-ADI-FDTD algorithm with the same CFLN; however, the 4S scheme also results in a four sub-step computational procedure, which costs more time than the two sub-step computational procedure in the CE-ADI-FDTD. In the CE-4S-ADI-FDTD algorithm, the computation time of each sub-step is same as in the CE-ADI-FDTD. Consequently, by selecting double the CFLN used in the CE-ADI-FDTD at each time step the computation time based on the four sub-steps computational procedure in the CE-4S-ADI-FDTD is same as the computation time based on the two sub-steps computational procedure in the CE-ADI-FDTD. In contrast, with the 4S scheme, the decline in accuracy of CE-4S-ADI-FDTD due to the large value of CFLN is much less than the decline in accuracy of CE-ADI-FDTD. In other words, by doubling the CFLN value, the computation time of the CE-4S-ADI-FDTD is same as the computational time of the CE-ADI-FDTD, although CE-4S-ADI-FDTD is more accurate than CE-ADI-FDTD.

In the proposed CE-4S-FADI-FDTD algorithm, as a benefit of the fundamental scheme, the time required for each sub-step in the four sub-step procedure is much less than the time required for each sub-step in the two sub-step based CE-ADI-FDTD. Therefore, without a significant increase in the CFLN value, the proposed CE-4S-FADI-FDTD algorithm provides a faster computational speed than the CE-ADI-FDTD while maintaining greater accuracy. In all sub-figures of Figure 8.1, with CFLN= 6 the solution using the proposed CE-4S-FADI-FDTD algorithm is in much better agreement with the reference so-

lutions than from CE-ADI-FDTD with CFLN= 4. In Table 8.1, the CPU time required by CE-4S-FADI-FDTD is 5% less than that required by CE-ADI-FDTD.

Table 8.1. Comparison of computational costs using different methods with PEC boundaries

| | CE-FDTD | CE-ADI-FDTD | CE-4S-FADI-FDTD |
|---|---|---|---|
| $\Delta$ | $\lambda_{min}/10$ | $\lambda_{min}/10$ | $\lambda_{min}/10$ |
| Cavity | $47 \times 47 \times 47$ | $47 \times 47 \times 47$ | $47 \times 47 \times 47$ |
| CFLN | 1 | 4 | 6 |
| Iterations | 1965 | 491 | 327 |
| CPU | 811.44 seconds | 570.95 seconds | 539.6 seconds |

In Figure 8.2, the FDTD solution with CFLN= 0.25 is given for comparison with the reference CE based FDTD solutions. Because of the high center frequency of the source, the phases of fields are extremely sensitive to spatial distance. In contrast, the phase error grows rapidly in only a few steps of propagation; the phase error accumulates as the wave propagates, especially after impinging on the PEC boundaries. As a result, CFLN= 0.25 is selected for the classical FDTD. With the CE algorithm, the fields are complex but LPL, without extreme change of phase in space. Consequently CFLN= 1 is adequate for the CE based FDTD's. The solutions are all in good agreement. For CFLN= 0.5, the error in the classical FDTD solution is apparent.

These numerical results demonstrate the accuracy and unconditional stability of the proposed method. It has been shown that, with an appropriately large CFLN, the CE-4S-FADI-FDTD algorithm outperforms CE-ADI-FDTD in accuracy and computational effectiveness together.

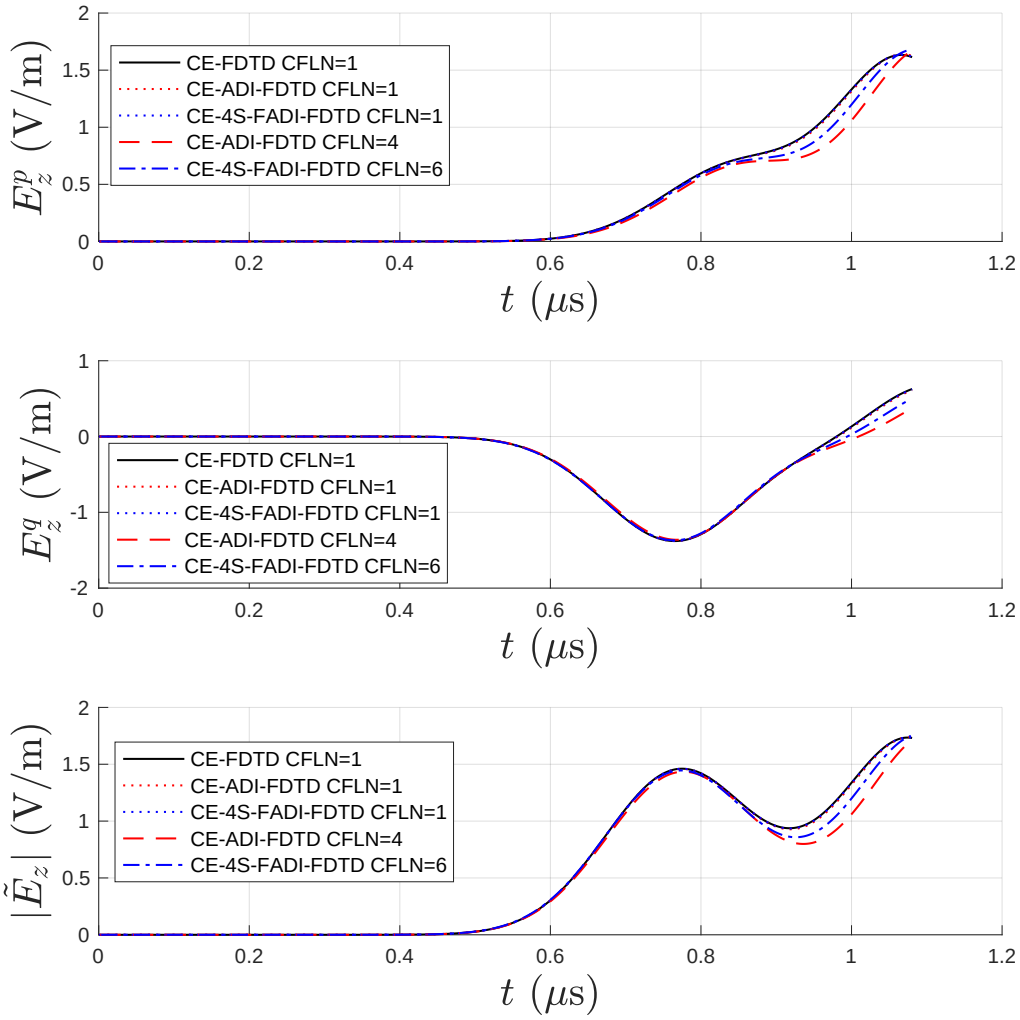


Figure 8.1. Comparison of $\tilde{E}_z$ at the observation point for the 3D model excited by a point source and truncated by PEC boundaries.

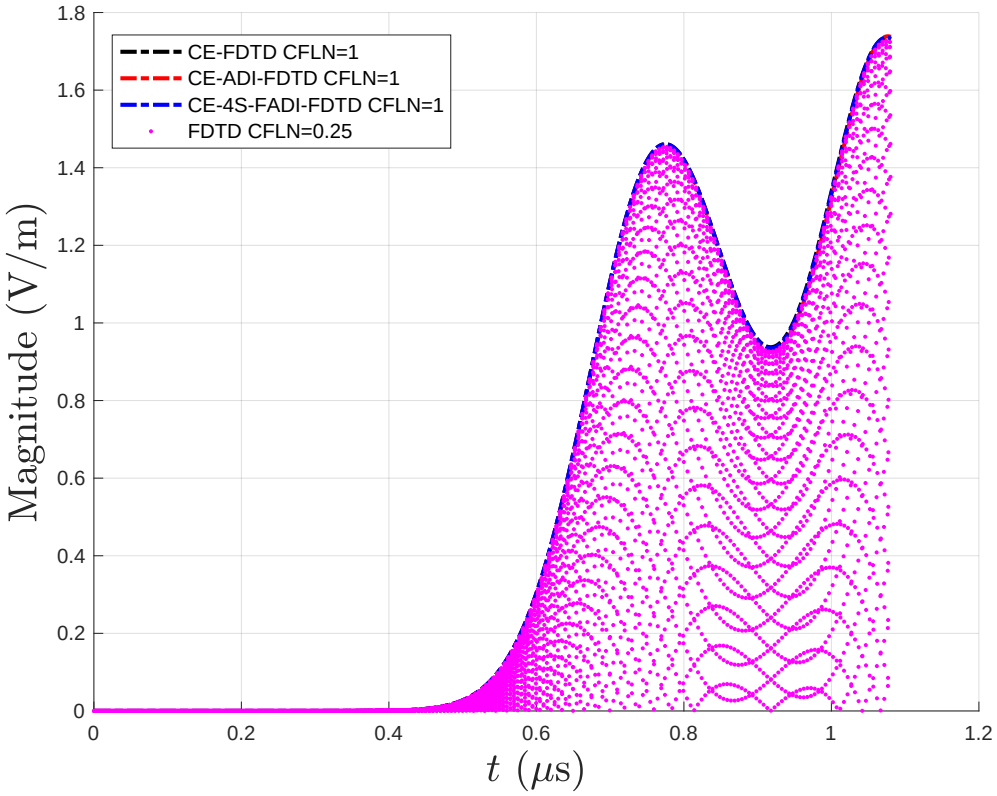


Figure 8.2. Comparison of $|\tilde{E}_z|$ according to the CE based FDTD and $|E_z|$ based on the classical FDTD at the observation point.

## 8.2 Point Source and NPML Boundaries

In this section, a 3D cavity truncated by the NPML region is modeled. The spatial step size is chosen to be the same in each direction, at $\Delta = \Delta x = \Delta y = \Delta z = 0.2855$ m. In each direction, a NPML region of ten cells is extended along both sides of the computational domain, which forms the new cavity with $41 \times 41 \times 41$ cells. The point source is located at $(21, 21, 21)$. The source function is the same as in equation (8.1), and the observation point is at $(11, 21, 21)$. The time step is $\Delta t = 0.54986$ $ns$ for CFLN= 1. The NPML region $[10, 2, 0.001\%]$ is defined with the same setting as in (6.32) and (6.33).

Comparison of $\tilde{E}_z$ at the observation point is shown in Figure 8.3. Since the incident wave and the reflected wave are absorbed in the NPML region, phase error due to reflection is eliminated. Accordingly, the solutions using all methods exhibit excellent accuracy. In Figure 8.3, IFFT represents the solution based on the 3D free-space Green's function and IFFT. The CE-FDTD solution is also depicted, and is in good agreement with the IFFT solution. With CFLN= 6, the CE-ADI-FDTD solution is reasonably accurate without the issue of phase error from the reflected waves; however, the error of the in-phase component in the top sub-figure is still observable. In contrast, with CFLN= 15, the CE-4S-FADI-FDTD solution adherers to the reference solutions, showing its ability in maintaining accuracy with a large CFLN.

Table 8.2. Comparison of the computational costs using different methods with NPML boundaries

| | CE-FDTD | CE-ADI-FDTD | CE-4S-FADI-FDTD |
|---|---|---|---|
| $\Delta$ | $\lambda_{min}/10$ | $\lambda_{min}/10$ | $\lambda_{min}/10$ |
| Cavity | $41 \times 41 \times 41$ | $41 \times 41 \times 41$ | $41 \times 41 \times 41$ |
| CFLN | 1 | 6 | 15 |
| Iterations | 2096 | 349 | 140 |
| CPU | 815.26 seconds | 681.24 seconds | 482.13 seconds |

The computation times taken for the different CE based FDTD methods are shown in Table 8.2. The computation time for CE-4S-FADI-FDTD is 29% less than for CE-ADI-

FDTD. The proposed CE-4S-FADI-FDTD algorithm therefore provides a faster and more accurate solution than CE-ADI-FDTD in problems truncated by NPML boundaries.

Figure 8.4 shows the classical FDTD solution for the same problem. The magnitude of the electric field at the observation point based on different methods is shown. By avoiding the phase error from the reflected boundaries, the classical FDTD solution remains accurate with CFLN= 0.5 and all solutions are in good agreement.

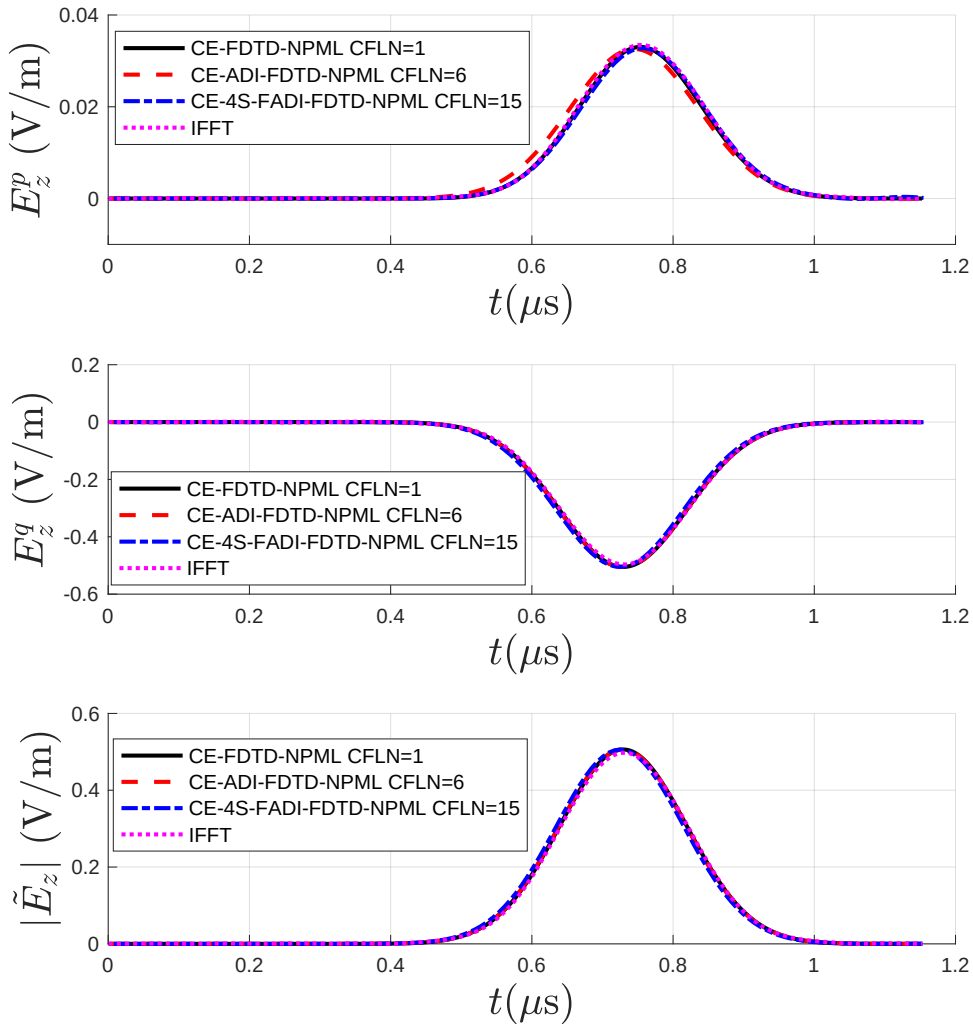


Figure 8.3. Comparison of $\tilde{E}_z$ at the observation point for the 3D model excited by a point source and truncated by NPML boundaries.

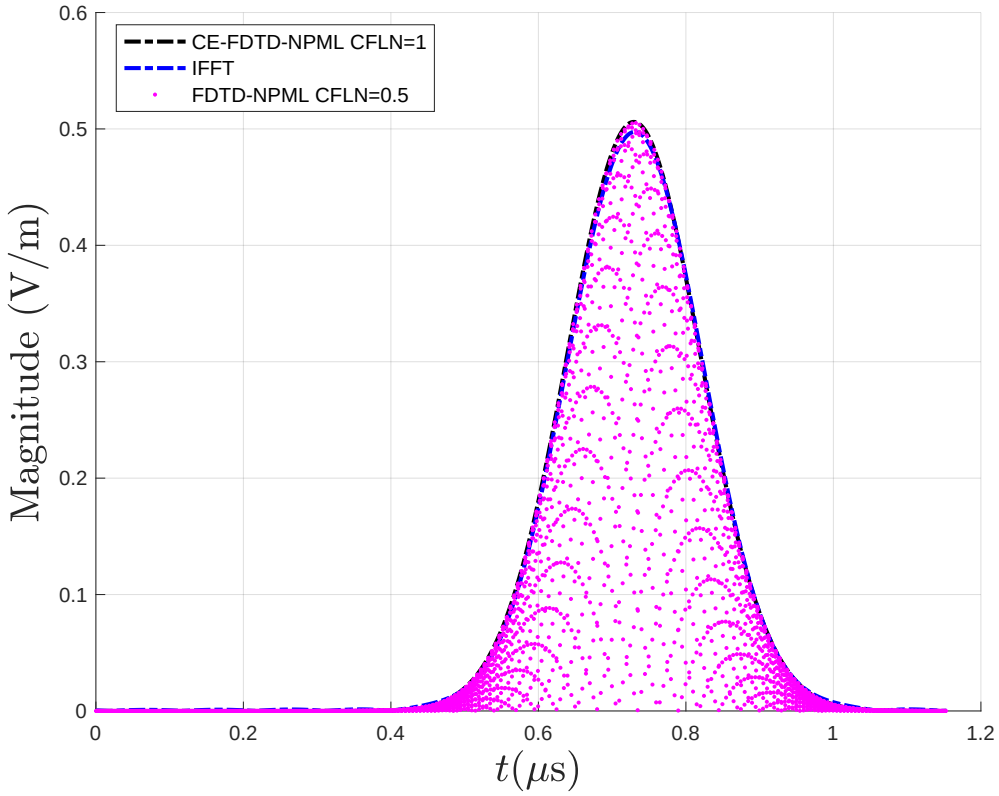


Figure 8.4. Comparison of $|\tilde{E}_z|$ according to the CE based FDTD and $|E_z|$ based on the classical FDTD at the observation point.

## 8.3 Plane Wave Source and NPML Boundaries

In the 3D cavity model excited by a plane wave source, the incident fields in the 3D space are obtained from an auxiliary grid, and the $z$-directed electric current source in the 1D grid is

$$J_{z,1D}(t) = -\frac{2}{2\eta\Delta x}\exp\Big[-(\frac{t-t_0}{\sqrt{2}\sigma_0})^2\Big]\cos(2\pi f_0 t), \tag{8.2}$$

where $\Delta x = \lambda_{min}/20 = 0.1249$ m, $t_0 = 180.06$ $n$s, $\sigma_0 = 22.508$ s, and the characteristic impedance of free-space $\eta = 120\pi$ $\Omega$. The center frequency $f_0 = 100$ MHz and the bandwidth is $bw = 40$ MHz.

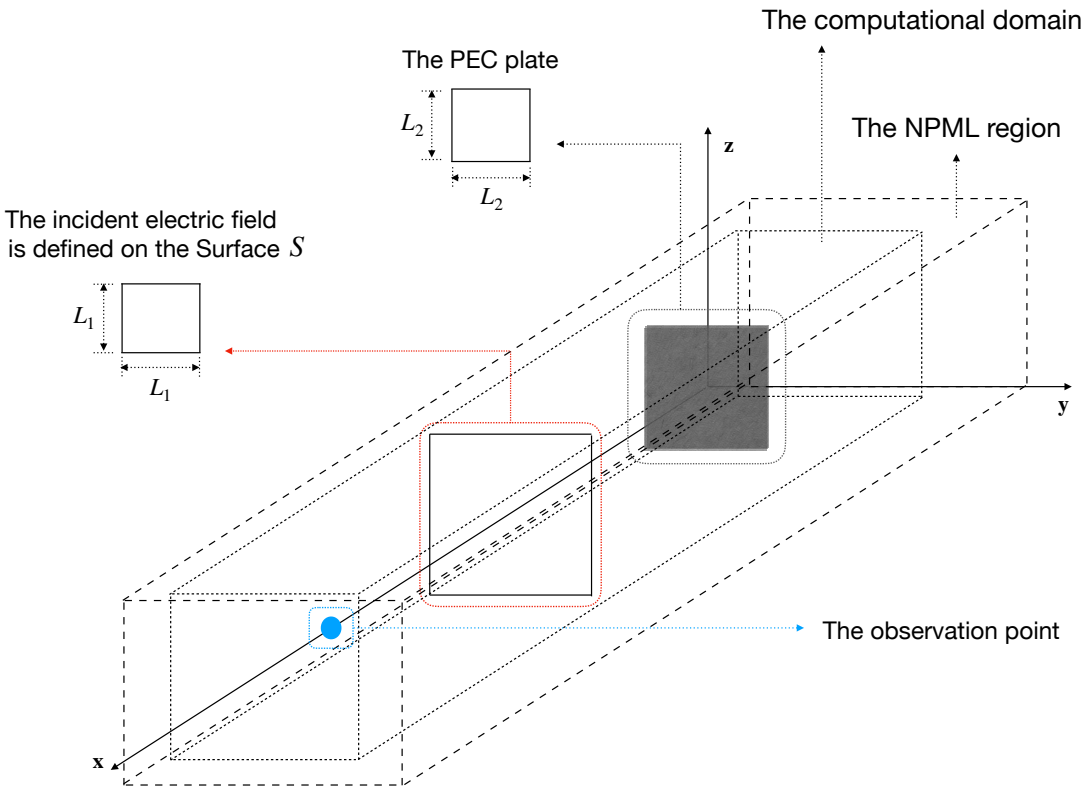


Figure 8.5. The model for the 3D cavity with a plane wave source and NPML boundaries.

Figure 8.5 depicts the 3D model of the scattering problem. The incident CE electric

field $\tilde{E}_{z,inc}$ is defined on Surface $S$ which is centered at $(\lambda_0, 0, 0)$. The PEC plate, which acts as the reflector in the scattering problem, is centered at the origin, and the observation point is positioned at $(11\lambda_0, 0, 0)$. The observation point is therefore a distance $11\lambda_0$ from the PEC reflector. The size of $S$ and the PEC plate aregiven by $L_1$ and $L_2$, where $L_1 = 0.75\lambda_{min}$ and $L_2 = 0.55\lambda_{min}$. The spatial steps in the 3D model are same as the spatial step in the 1D auxiliary grid: $\Delta x = \Delta y = \Delta z = 0.1249$ m. The time step $\Delta t = 0.24056$ $n$s for CFLN= 1.

As shown in Figure 7.1, the incident field $\tilde{E}_{z,inc}$ propagates in the $-x$ direction and subsequently impinges on the PEC plate. The PEC plate is then illuminated by the incident field, from which the induced current is created. The induced current then becomes a radiating source, which results in propagation of the scattered field.

The scattered field at the observation point is shown in Figure 8.6. The size of the cubic cell in VIE-MOM is same as that in the CE based FDTD's. The PEC plates in all the solutions are consequently modeled by one layer of cubic cells. As can be seen in all the sub-figures, CE-FDTD and VIE-MOM serve as the reference solutions, and are in good agreement. With CFLN= 6, the proposed CE-4S-FADI-FDTD solution still preserves great accuracy and stability. Comparison of the numerical results makes clear that the TFSF scheme and the NPML algorithm can be incorporated into the CE-4S-FADI-FDTD algorithm for modeling the boundless cavity excited by a plane-wave source.

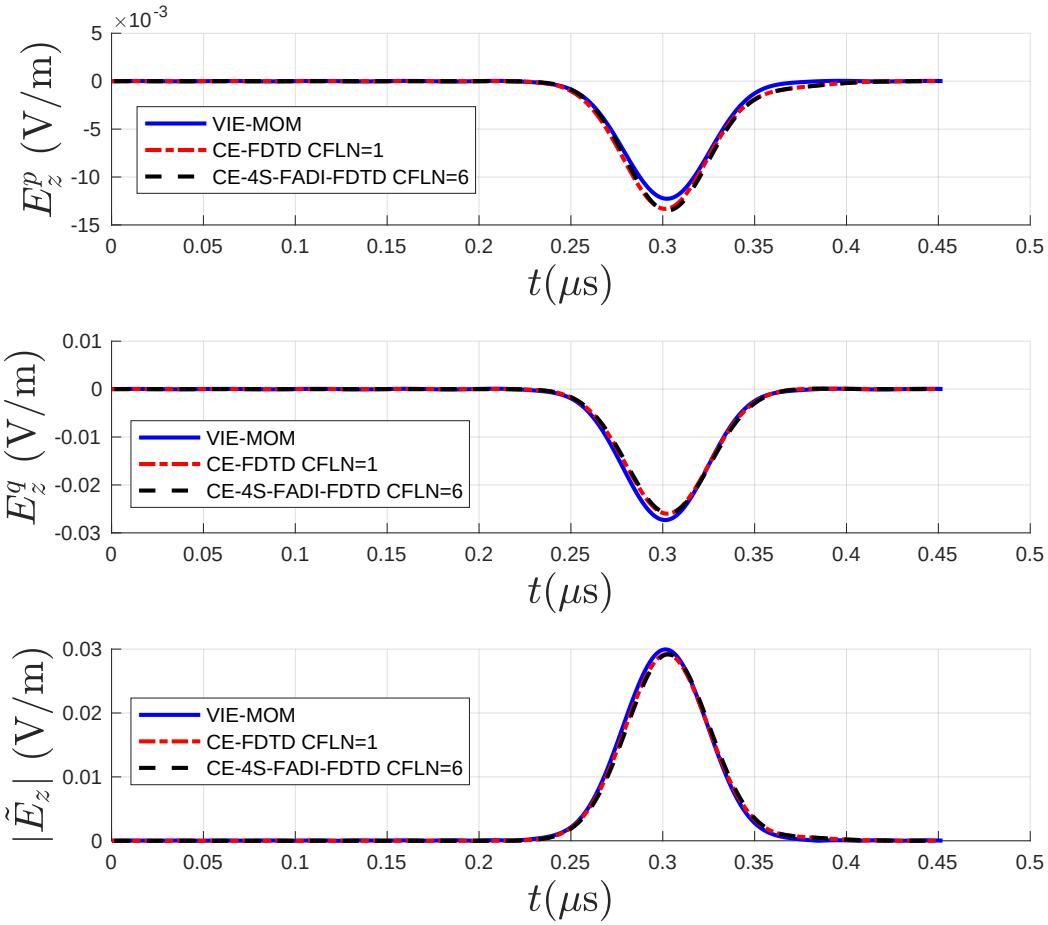


Figure 8.6. The scattered field at the observation point.

# CHAPTER 9

# CONCLUSIONS AND FUTURE WORK

## 9.1 Conclusion

The 3D CE-4S-FADI-FDTD algorithm has been formulated in detail by considering the excitation source and the boundary conditions. It is well known that a large value of CFLN leads to a decline in accuracy. By applying the 4S scheme, the four sub-steps procedure is used at each time step and provides greater accuracy than the two sub-steps procedure in the CE-ADI-FDTD algorithm.

In addition, use of the fundamental scheme greatly reduces the number of terms and operations in the implicit equations. In each sub-step, the implicit equations are solved multiple times, and most of the computation time is consumed by the implicit equations. This improvement in solving the implicit equations therefore gives a considerable reduction in the total computation time.

The examples demonstrate that the CE-4S-FADI-FDTD algorithm provides more accurate and faster solutions than the CE-ADI-FDTD algorithm for cavity problems with different sources and boundary conditions. In summary, by benefiting from the 4S scheme and the fundamental scheme, the proposed CE-4S-FADI-FDTD algorithm outperforms CE-ADI-FDTD in both accuracy and computational effectiveness.

## 9.2 Future Work

The proposed CE-4S-FADI-FDTD algorithm serves as an improved version of the CE-ADI-FDTD. Disadvantages of the CE-ADI-FDTD have also been inherited, however, and overcoming these disadvantages is an aim of future work. Three disadvantages of the proposed method are identified, as follows.

### 9.2.1 The Bandwidth of The Source Excitation

Like the CE-ADI-FDTD, the proposed 3D CE-4S-FADI-FDTD method is developed for a problem with a narrow-band source. That is, as the ratio of the center frequency to the bandwidth in the source function increases, the accuracy from the CE scheme is improved. With a wide-band source, therefore, the accuracy using the CE scheme is less.

### 9.2.2 The Cavity Size

As an implicit FDTD method, the CE-4S-FADI-FDTD algorithm provides a faster solution than the explicit FDTD method for a relatively small cavity problem. The computation time cost from using an implicit equation is much larger than that from an explicit equation. For a large cavity, more cells are therefore needed in modeling the problem. All fields in the explicit FDTD are calculated by explicit equations, and the increase in the computation time is therefore limited. In contrast, the electric fields in the CE-4S-FADI-FDTD algorithm are all calculated via implicit equations. More cells imply more implicit equations, and therefore greatly increase the computation time. To compensate for the time increase from the additional implicit equations, a larger CFLN is required, degrading the accuracy.

### 9.2.3 The Spurious Charge Problem

The proposed 3D CE-4S-FADI-FDTD algorithm suffers from the spurious charge problem, discussed in Jung et al. (2009). A spurious charge exists near the source region, which acts as a secondary radiating source and causes errors. If the CFLN is small, the spurious charge grows extremely slowly, and the erroneous fields generated by the spurious charge is negligible. With a large CFLN, however, as the simulation proceeds, the spurious charge grows rapidly and wrecks the solution based on the actual source. So far no stable method has been developed for eliminating the spurious charge in the 3D case; this is an interesting challenge.

# BIBLIOGRAPHY

# BIBLIOGRAPHY


Balanis, C. A. (2011), *Advanced Engineering Electromagnetics*, 315 – 321 pp., John Wiley & Sons, Inc.

Berenger, J. P. (1994), A perfectly matched layer for the absorption of electromagnetic waves, *Journal of Computational Physics*, 114, 185–200.

Chew, W. C., and W. H. Weedon (1994), A 3D perfectly matched medium from modified Maxwell's equations with stretched coordinates, *Microwave and Optical Technology Letters*, 7, 599–604.

Cummer, S. A. (2003), Simple, nearly perfectly matched layer for general electromagnetic media, *IEEE Microwave and Wireless Components Letters*, 13(3).

Elsherbeni, A., and V. Demir (2009), *The Finite-Difference Time-Domain Method for Electromagnetics with Matlab Simulations*, 187-229 pp., SciTech Publishing.

Goggans, P. M., and Q. Liu (2015), A complex-envelope FDTD formulation using alternating in-phase and quadrature field variables, *IEEE Transactions on Antennas and Propagation*, 63(11).

Haykin, S. S. (1983), *Communication System*, 2 ed., New York: Wiley.

Jung, K.-Y., F. L. Teixeira, S. G. Garcia, and R. Lee (2009), On numerical artifacts of the complex envelope ADI-FDTD method, *IEEE Transactions on Antennas and Propagation*, 57(2).

Kong, Y., and Q. Chu (2009), A novel three-dimensional unconditionally-stable FDTD method, *IEEE MTT-S International Microwave Symposium Digest*.

Kong, Y., and Q. Chu (2010a), Unconditionally stable finite-difference time-domain methods with high-order accuracy in two and three dimensions, *IET Microw. Antennas Propag.*, 4, 1605 – 1616.

Kong, Y., and Q. Chu (2010b), Development of the nearly PML for four-stages split-step unconditionally-stable FDTD method, *Microwave Conference Proceedings, Asia-Pacific*.

Lee, J., and B. Fornberg (2003), A split step approach for the 3-D Maxwell's equations, *Journal of Computational and Applied Mathematics*, 158, 485 – 505.

Li, J., H. Jiang, and N. Feng (2015), Efficient FDTD implementation of the ADE-based CN-PML for the two-dimensional TMz waves, *The Applied Computational Electromagnetics Society Journal*, 30(6).

Liao, Z. (1996), Extrapolation non-reflection boundary conditions, *Wave Motion*, 24, 117–138.

Lin, H., P. Ding, and G. Wang (2007), Perfectly matched layer for two-dimensional unconditionally stable FDTD method based on approximate Crank-Nicolson scheme, *Microwave and Optical Technology Letters*, 49, 1178–1182.

Ma, C. (2006), Development of complex envelope FDTD methods for electromagnetic modeling and simulation, Ph.D. thesis, Dalhousie University.

Ma, C., and Z. Chen (2005), Dispersion analysis of the three-dimensional complex envelope ADI-FDTD method, *IEEE Transactions on Antennas and Propagation*, 53(3).

Mur, G. (1981), Absorbing boundary conditions for the finite-difference approximation of the time-domain electromagnetic-field equations, *IEEE Transactions on Electromagnetic Compatibility*, EMC-23(4).

Namiki, T. (1999), A new FDTD algorithm based on alternating-direction implicit method, *IEEE Transactions on Microwave Theory and Techniques*, 47(10).

Namiki, T. (2000), 3-D ADI-FDTD method-unconditionally stable time-domain algorithm for solving full vector Maxwell's equations, *IEEE Transactions on Microwave Theory and Techniques*, 48(10).

Pursel, J. D., and P. M. Goggans (1999), A finite-difference time-domain method for solving electromagnetic problems with bandpass-limited source, *IEEE Transactions on Antennas and Propagation*, 47(1).

Ramadan, O. (2005), Unconditionally stable nearly PML algorithm for linear dispersive media, *IEEE Microwave and Wireless Components Letters*, 15(7).

Ramadan, O. (2009), Complex envelope four-stage ADI-FDTD algorithm for narrowband electromagnetic applications, *IEEE Antennas and Wireless Propagation Letters*, 8.

Schneider, J. (2010), *Understanding the finite-difference time-domain method*, `www.eecs.wsu.edu/~schneidj/ufdtd`.

Sefer, A., M. A. Uslu, and L. Sevgi (2015), Matlab-based 3-D MoM and FDTD codes for the RCS analysis of realistic objects, *IEEE Antennas and Propagation Magazine*, 57, 122 – 148.

Sun, C., and C. Trueman (2003), Unconditionally stable Crank-Nicolson scheme for solving two-dimensional Maxwell's equations, *Electronics Letters*, pp. 595 – 597.

Sun, G., and C. W. Trueman (2006), Efficient implementations of the Crank-Nicolson scheme for the finite-difference time-domain method, *IEEE Transactions on Microwave Theory and Techniques*, 54(5).

Tan, E. L. (2008), Fundamental schemes for efficient unconditionally stable implicit finite-difference time-domain methods, *IEEE Transaction on Antennas and Propagation*, 56(1).

Umashankar, K., and A. Taflove (1982), A novel method to analize eletromagnetic scattering of complex objects, *IEEE Transactions on Electromagnetic Compatibility*, EMC-24(4).

Yee, K. (1966), Numerical solution of initial boundary value problems involving Maxwell's equations in isotropic media, *IEEE Transactions on Antennas and Propagation*, 14.

Zhang, L., and T. Yu (2012), A method of improving the stability of Liao's higher-order absorbing boundary condition, *Progress in Electromagnetics Research*, 27, 167–178.

# VITA

Qi Liu received the B.S. degree from Jianghan University in 2009. In the Spring of 2014, he completed his Master of Engineering Science (electromagnetics) and continued to pursue the degree of Doctor of Philosophy in Engineering Science (electromagnetics) at the University of Mississippi.

From 2012 to 2019, he studied as a graduate student in the Department of Electrical Engineering at the University of Mississippi. He worked as a teaching assistant and a research assistant during his graduate study.